PREPARATION AND CHARACTERIZATION OF POLYOLEFIN / NANOSILICA COMPOSITES

by

MATHIEU BAILLY

A thesis submitted to the Department of Chemical Engineering

In conformity with the requirements for

the degree of Doctor of Philosophy

Queen's University

Kingston, Ontario, Canada

(April, 2011)

Abstract

Polypropylene (PP) and ethylene-co-octene copolymer (EOC) blends were prepared at various component ratios and reinforced with silica nanoparticles (SiO_2). Strategies to improve filler dispersion involved the grafting of a silane coupling agent on the PP matrix, the addition of a maleated PP (PP-g-MA) as a compatibilizer and the use of hydrophobic silica nanoparticles. These approaches resulted in a fine dispersion of the nanoparticles within the PP phase and induced a reduction of the size of the EOC domains, due to a barrier effect. Tensile and flexural properties were significantly increased, whereas ductility and impact properties were not affected. These enhancements are attributed to the favourable microstructure of the blends, featuring a segregated microstructure, and to the improved interfacial adhesion between the functionalized polymer matrix and the surface of the nanoparticles.

The microstructure and rheology of model melt compounded EOC-based nanocomposites were investigated. Functionalization of the polyolefin matrix was accomplished through silane grafting, or addition of a maleated EOC (EOC-g-MA) compatibilizer. Various grades of unmodified SiO_2 having different specific surface areas (SSA), as well as a surface-modified grade were added to the EOC matrix at various loadings. The formation of covalent and hydrogen bonds between the silanol groups and the functionalized polymer generated strong polymer/filler (P/F) interactions, resulting in improved filler dispersion. Bound polymer characterization revealed that in the compatibilized materials, the amount of polymer physically attached to the nanoparticles was higher than in the non-compatibilized samples.

In the absence of a compatibilizer, larger SiO_2 aggregates formed upon increasing SSA because of increased probability of hydrogen bonding between the particles. The increased propensity for aggregation was revealed by time sweeps as well as by the increased strain sensitivity in stress sweeps. On the contrary, the compatibilized composites exhibited a stable response and a higher

critical strain for the onset of non-linearity, indicative of stronger adhesion between the fillers and the matrix.

Superposition of oscillatory and creep/recovery experiments revealed that the viscoelastic properties in the terminal region were influenced substantially by the state of dispersion of the nanoparticles. In the absence of a compatibilizer, substantial enhancements in the linear viscoelastic (LVE) functions were noted and an increasing SSA resulted in more significant deviations from terminal flow. On the contrary, the SSA of the particles had no effect on the viscoelastic and mechanical properties of the compatibilized composites.

Co-Authorship

This thesis contains chapters that present results that have been published in the form of original journal articles as well as material that is in preparation for submission. The complete citations for these papers and the chapters in which they appear are provided below:

Chapter 2: Bailly M., Kontopoulou M. "Nanocomposite blends containing polyolefins" in “Advanced Polyolefin nanocomposites" Ed. Vikas Mittal, CRC Press, Taylor and Francis, 2011.

Chapter 3: Lee S.H., Bailly M., Kontopoulou M. "Morphology and properties of polypropylene/ethylene-octene copolymer blends containing nanosilica” Submitted to Macromolecular Materials and Engineering

Chapter 4: Bailly M., Kontopoulou M. Polymer 2009; 50(11); 2472-80

Chapter 5: Bailly M., Kontopoulou M., El Mabrouk K. Polymer 2010; 51(23); 5506-15

All the papers were co-authored and reviewed prior to submission to publication by Dr. Marianna Kontopoulou. The first paper was co-authored by Dr. Sung-Hyo Lee as he was responsible for the compounding of the materials and did part of the characterization. The third paper was co-authored with Dr. Khalil El Mabrouk because he conducted the DMA experiments and assisted in the development of the functionalization technique. All of the remaining work and manuscript preparation were performed by the author of this thesis.

Acknowledgements

I would like to thank my supervisor Dr. Marianna Kontopoulou for her continuous support and guidance during my time at Queen's University. In addition to the time she spent with me daily, providing valuable explanations about the numerous technical and theoretical questions I had, I especially appreciated her positive and encouraging attitude towards my work.

Financial support in the form of scholarships from the National Sciences and Engineering Research Council (NSERC), and Queen's University (Queen's Graduate Award) is gratefully acknowledged. Materials supplied by E.I. Dupont, Evonik Industries and Nanocor Incorporated are appreciated.

I am grateful to the following people for the technical assistance they provided over the course of this research project: Mr Douglas Holmyard of the Mount Sinai Hospital for the observations of the TEM samples, Mr Charlie Cooney for the SEM analysis, Mrs Andrea Liskova for her help with the different instruments of polymer characterization, Dr. Khalil El Mabrouk for his contribution to Chapters 4 and 5, Dr. Sung-Hyo Lee for his contribution to Chapter 3, Kelly Sedore and Steven Hodgson for their help with my experimental work and my labmates Ying, Andrew and Karthik.

A final heartfelt *Merci* goes to my partner Erika for her unconditional love and moral support. I would also like to deeply thank my parents, my siblings, my grand-parents, the Knights' family, Dr. Niels Smeets and Reza Saiedi, my friends from home, Jérôme, Laurent, Tony and Morgan. You all helped me to make the most of my experience in Canada. Thank you.

Statement of Originality

I hereby certify that all of the work described within this thesis is the original work of the author. Any published (or unpublished) ideas and/or techniques from the work of others are fully acknowledged in accordance with the standard referencing practices.

Mathieu Bailly

April, 2011

Table of Contents

List of Figures

List of Tables

Nomenclature

A	Area (m^2)
d	Particle diameter (nm)
d_f	Fractal dimension
D_n	Number Diameter (m)
D_v	Volume Diameter (m)
E’	Elastic modulus (Pa)
E”	Loss modulus (Pa)
Ec	Cohesive energy density ($J.m^{-3}$)
G’	Elastic or Storage modulus (Pa)
G'_0	Storage modulus at 0.04 rad/s (Pa)
G”	Viscous or loss modulus (Pa)
G_N	Plateau Modulus (Pa)
H_k	Relaxation strength (Pa)
J_c	Creep compliance (Pa^{-1})
J_r	Creep Recovery compliance (Pa^{-1})
J_e^0	Recoverable compliance (Pa^{-1})
J’	Real part of the complex compliance (Pa^{-1})
J”	Imaginary part of the complex compliance (Pa^{-1})
J_k	Retardation strengths, discrete spectrum (Pa)
L_k	Retardation strengths, continuous spectrum (Pa)
n	Number of particles
PI	Polydispersity Index D_v/D_n
T	Temperature (°C)

t	Time (s)
t_c	Creep time (s)
T_c	Temperature of crystallization (°C)
T_g	Glass transition temperature (°C)
T_m	Melting point (°C)
t_r	Recovery time (s)
W	Work of adhesion (J)

Greek Symbols

η^*	Complex Viscosity (Pa.s)
η_0	Zero shear viscosity (Pa.s)
ω	Angular frequency (rad/s)
ω	Wetting Coefficient
$\tan\delta$	Loss tangent G"/G'
ϕ	Volume fraction (vol%)
ϕ_c	Critical Volume fraction (vol%)
ϕ_e	Effective volume fraction (vol%)
γ	Strain
γ_c	Critical Strain
γ_A	Surface tension of A (J/m^2)
γ_{A-B}	Interfacial tension between A and B (J/m^2)
τ	Stress (Pa)
ψ	Creep function
λ_k	Relaxation time (s)
τ_k	Retardation Time (s)

ΔH_f	Heat of fusion (J/g)
ΔH_c	Heat of crystallization (J/g)
Δ	Polymer Shell thickness (nm)
χ_c	Degree of crystallinity (%)

Abbreviations

ASTM	American Society for Testing Materials
BdP	Bound polymer
$BaSO_4$	Barium sulfate
BET	Brunauer-Emmet-Teller
$CaCO_3$	Calcium carbonate
CCA	Cluster-Cluster Aggregation
DCP	Dicumyl Peroxide
Deg-PP	Degraded polypropylene
DMA	Dynamic Mechanical Analysis
DSC	Differential Scanning Calorimetry
EC	Ethylene-α-olefin copolymer
EOC	Poly(ethylene-*co*-octene)
EOC-g-MA	Poly(ethylene-*co*-octene)-*graft*-maleic anhydride
EOC-g-VTEOS	Poly(ethylene-*co*-octene)-graft-vinyltriethoxysilane
EOC-g-VTES	Poly(ethylene-*co*-octene)-graft-vinyltriethylsilane
EPDM	Ethylene-propylene-diene
EPR	Ethylene-propylene-rubber
EVA	Ethylene vinyl acetate
F/F	Filler/Filler (interactions)

FT-IR	Fourrier-Transformed Infrared
hex-SiO_2	Surface-treated silica nanoparticles with hexadecyl-silane
HCl	Hydrochloric acid
HDPE	High Density Polyethylene
IFSS	Interfacial Shear Strength
IGC	Inverse Gas Chromatography
LCB	Long Chain Branching
LLDPE	Linear Low Density Polyethylene
LVE	Linear viscoelastic
MA	Maleic Anhydride
MFI	Melt Flow Index
MFR	Melt Flow Ratio
$Mg(OH)_2$	Magnesium hydroxide
NLREG	Non linear Regularization Software
NMR	Nuclear Magnetic Resonance
oct-SiO_2	Surface-treated silica nanoparticles with octyl-silane
PC	Polycarbonate
PE	Polyethylene
PE-g-MA	Poly(ethylene-*graft*-maleic anhydride)
PEMFC	Proton Exchange Membrane Fuel Cell
PEO	Polyethylene oxide
P/F	Polymer/Filler (interactions)
phr	Parts per Hundred
PMMA	Polymethylmethacrylate
POE	Polyolefin elastomer

PP	Polypropylene
PP-g-MA	Poly(propylene-*graft*-maleic anhydride)
PP-g-VTEOS	Poly(propylene-*graft*-vinyltriethoxysilane)
P/P	Polymer/Polymer (interactions)
PS	Polystyrene
PU	Polyurethane
RPM	Revolutions Per Minute
SAOS	Small Amplitude Oscillatory Shear
SCB	Short Chain Branching
SEBS	Styrene ethylene-butylene styrene
SEM	Scanning Electron Microscopy
SiO_2	Silicon dioxide
sPPEK	Sulfonated poly(phthalazinone ether ketone)
SSA	Specific Surface Area
$SiCl_4$	Silicon tetrachloride
TEM	Transmission Electron Microscopy
TGA	Thermogravimetric Analysis
TPO	Thermoplastic Olefin
TTS	Time-Temperature-Superposition
VTEOS	Vinyltriethoxysilane
VTES	Vinyltriethylsilane

Chapter 1

INTRODUCTION

Over the last few decades, thermoplastics have found increasing use in engineering applications due to their attractive properties such as light-weight, low cost, ease of fabrication and recycling. To further reduce cost, inexpensive, inert, micro-sized fillers such as talc are commonly added into thermoplastics. Fillers can also be used as additives to enhance various properties including color, surface properties, dimensional stability, thermal properties, electrical properties, magnetic properties, etc [1]. Furthermore, to counteract the low modulus of most thermoplastics, reinforcement using rigid fillers to create polymer composites with enhanced mechanical properties has been implemented in both academia and industry. Common micro-sized fillers aiming at improving the mechanical properties of thermoplastics include calcium carbonate ($CaCO_3$), silicon dioxide (SiO_2), barium sulfate ($BaSO_4$), glass beads, magnesium hydroxide ($Mg(OH)_2$), etc. In the early 90's, the now famous researchers of the Toyota Research Centre in Japan reported the preparation of polyamide-6 nanocomposites reinforced with layered silicates and their very promising properties [2,3]. Since then, many different kinds of fillers exhibiting at least one dimension at the nanometer have been used as reinforcing agents. Generally speaking, the mechanical properties of the polymer matrices, including Young's modulus and yield stress, as well as their thermal stability and barrier properties can be markedly improved by the addition of small quantities (a few weight percent) of nanofillers [4,5]. However, even in the best case scenario when particles are well-dispersed and the reinforcement is significant, many authors have reported a reduction of toughness and ductility accompanying the addition of nanofillers [5]. The numerous potential applications of polymer nanocomposites, mainly in the automotive and packaging industries, combined with their ease of fabrication using common polymer processing

techniques –such as extrusion and injection moulding- makes them an extremely versatile and promising class of materials [6,7].

Among the various types of inorganic nanofillers available, silica has been used in a large variety of industrial applications due to its ability to modify the physical properties of plastics, rubbers and fluids. Practical examples include using silica particles as thickening agents in paints, inks and adhesives and as reinforcing fillers in the rubber industry. The recent commercial availability of fumed silica of nanoscale dimensions has boosted the interest for its use in a variety of polymer-based systems [8-10]. Examples of applications include coatings, where hybrid organic/inorganic materials using silica particles combine transparency, easy processing, hardness, good adhesion to the substrate, and enhanced scratch and abrasion resistance [11]. Polymer/silica nanocomposites have also been used to make proton exchange membranes (PEMs), one of the major component of proton exchange membrane fuel cells (PEMFCs). Sulfonated poly(phthalazinone ether ketone) (sPPEK) filled with silica particles exhibit improved swelling behavior, thermal stability, and mechanical properties compared to the pristine material [12]. In structural materials, where silica particles are widely used as reinforcing agents aiming at improving the mechanical properties of the pure matrix, the state of dispersion of the nanoparticles and their interactions with the hosting polymer chains are the critical factors determining the degree of reinforcement. Even though interactions between silica or carbon black particles and rubbers have been widely and deeply studied for decades, including their consequences in terms of rheological behavior [8], research focusing on thermoplastic/polyolefin based matrices is relatively scarce.

Different processing routes have been implemented for the synthesis of thermoplastic-based / nanosilica composites: melt blending, solution blending, sol-gel process and in-situ polymerization [10]. They all aim at achieving a fine dispersion of the nanoparticles within the

polymer matrix, so that they can act as efficiently as possible as reinforcing agents. The state of dispersion of the particles is one of the major issues in silica-reinforced polymer nanocomposites. Indeed, in the presence of non-polar matrices such as polyethylene or polypropylene, silica particles tend to aggregate to form micrometer-sized clusters at the expense of the mechanical properties. In addition to the selection of appropriate processing equipment for compounding, strategies have been developed to break-up the filler aggregates either by turning the matrix more polar [13] by the addition of a compatibilizer [14], or by chemically modifying the surface of the particles to make it more compatible with the polymer matrix chains [15]. In addition to facilitating compounding, ensuring good polymer/filler (P/F) interactions to improve the load transfer between the fillers and the matrix is crucial to achieve optimum performance [16].

A frequent challenge encountered in composites technology is the loss of ductility, or toughness, upon addition of microscaled or nanoscaled fillers. In polymer technology the impact properties of some commodity polymers such as polymethylmethacrylate (PMMA), polyethylene (PE), polycarbonate (PC) and polypropylene (PP) [17] are generally improved through the addition of a rubbery phase to form a thermodynamically immiscible, phase-separated polymer blend [18]. S. Wu showed that the morphology of the blends is intimately related with their mechanical properties and established correlations between the toughness of a blend and the “matrix ligament thickness”, namely the inter-particle distance [19]. Among the available impact modifiers, such as ethylene-propylene-rubber (EPR), ethylene-propylene-diene (EPDM) and styrene ethylene-butylene styrene (SEBS), polyolefin elastomers (POEs) are a relatively more recent class of elastomer that emerged with the advent of a novel generation of metallocene catalysts during the ’90s, and have been shown to be particularly effective in the impact modification of PP [20]. POEs are copolymers of ethylene and an α-olefin, such as octene, butene and hexene comonomer,

presenting some short chain and long-chain branching (SCB and LCB) that disrupts the original polyethylene crystallinity, making them amorphous and introducing elastomeric properties.

It is common practice, especially in the automotive industry to combine these immiscible blends with fillers such as talc, glass fibers, etc, to improve the mechanical properties while reducing the cost. With the emergence of nanocomposite technology, attempts to combine the significant reinforcement observed upon addition of nanoparticles and the unique impact properties obtained with the introduction of a rubbery phase into a thermoplastic matrix have been made, leading to the so-called “ternary nanocomposites” or “polymer blend nanocomposites” [21-30].

1.1 Thesis objectives

Polyolefins are commodity plastics of significant industrial interest, which are widespread because of their low cost, recyclability, light-weight, ease of processing, good thermal and mechanical properties. They offer a wide range of properties, ranging from rigid (for example semi-crystalline polypropylene) to elastomeric (such as ethylene-α-olefin copolymers) materials. Even though polyolefin-based nanocomposites have many desirable properties, such as barrier properties, rigidity (stiffness), etc, these attributes are usually accompanied by an unavoidable deterioration in toughness. This is mainly due to a poor dispersion of the inorganic nanofillers into polyolefin matrices, and a weak adhesion at the filler-matrix interface. As a result, melt compounded polyolefin nanocomposites have not reached their full potential.

The present thesis seeks to overcome this challenge, by using nanofiller treatment and/or polymer functionalization techniques, as well through the synthesis of ternary nanocomposite blends that can provide a good balance of mechanical properties.

The first objective of this work is to combine polymer compounding and nanocomposite technology to take advantage of both the outstanding toughening capacity of an elastomer in a rigid PP matrix, and the reinforcing ability of silica nanoparticles. Ternary nanocomposites containing PP, a poly(ethylene-co-octene) (EOC) elastomer and a fumed nanosilica (SiO_2) were prepared and characterized. Various strategies were implemented, aiming at obtaining a good dispersion of the nanofillers and improving the interfacial adhesion with the matrix. These include addition of a compatibilizer, functionalization of the matrix, and the use of surface-treated nanoparticles. The efficiency of each strategy is assessed in terms of microstructure and mechanical performance. Other parameters known to influence the final properties of the composites are investigated, such as the silica concentration and the polymer blend ratio. An analysis of the effect of nanofillers on the microstructure of these blends is undertaken, and the resulting implications in terms of properties are reported.

The second objective of this work is to achieve a fundamental understanding of the mechanisms underlying the development of the microstructure and its effect on the rheological and mechanical properties of the nanocomposites. This topic is very controversial in the literature, as no agreement can be found on the interrelations between nanocomposite properties, their morphology and the extent of P/F and filler/filler (F/F) interactions. Various types of P/F interactions (chemical and physical) are established by using matrix functionalization and addition of a compatibilizer. In addition, the F/F interactions are varied by using silica particles with a wide range of specific surface area (SSA) and surface treatments. An EOC was selected as a model polymer in these formulations because it is amenable to grafting with coupling agents, while at the same time providing characteristics that make it ideal for rheological characterization, such as having low crystallinity and melting point and providing good thermal

stability. Along with microscopy, rheology was used as the main characterization tool because of its great sensitivity to the composite microstructure.

1.2 Thesis organization

The present thesis consists of seven chapters. Chapter 1 introduces the topic and explains the scope of this work. Chapter 2 reviews critically the methods of preparation, properties, and applications of the polymers and nanofillers used in this work, and also of the resulting binary/ternary nanocomposites. Chapters 3 and 4 are dedicated to the preparation and characterization of PP/EOC/SiO_2 ternary nanocomposites for extrusion and injection moulding applications respectively, using several strategies to optimize their microstructure and mechanical properties. Chapter 4 introduces silane grafting of the matrix as a means to obtain covalent bonding between the matrix and the SiO_2 particles. Chapter 5 studies with the aid of rheology the effects of covalent bonding and filler surface modification on the formation of flocculated SiO_2 structures, when relatively high amounts of SiO_2 are used. The effects of silica surface area and compatibilization are the subject of Chapters 6 and 7. A new technique based on the combination of creep and frequency sweep experiments has been implemented to extend the time scale experimentally accessible, and therefore enabled a more detailed rheological characterization of the materials. The consequences of the interactions in terms of microstructure and physical properties are discussed throughout the thesis.

Chapter 2

LITERATURE REVIEW*

2.1 Silica

2.1.1 Origin and chemical structure

Silica is a generic name for silicon dioxide (SiO_2), assigned to different minerals belonging to the silicate class. Silicon dioxide can be natural (quartz, cristobalite, tridymite, etc.), synthetic (fumed, precipitated, fused silica), crystalline (quartz) or amorphous (opal). The building block of silica and silicate structures is the $[SiO_4]^{4-}$ tetrahedron unit with a silicon ion at the center cavity. The different crystalline structures of silicon dioxide correspond to the possible arrangements of the $[SiO_4]^{4-}$ units, based on their tendency to form three-dimensional networks. The crystalline silicas are in fact network silicates where each silicon is bound to four oxygens and each oxygen is bound to two silicons [1,31]. Contrary to crystalline silicas, in amorphous silica the bulk structure is determined by a random packing of $[SiO_4]^{4-}$ units, which results in a non-periodic structure. Two distinct methods of production have been used to prepare synthetic silicas: pyrogenic or thermal (leading to fumed silica) and the wet process (leading to precipitated silica). Fumed silica is made from the reaction of metallic silicon and gaseous dry HCl to form silica tetrachloride $SiCl_4$, which is mixed with hydrogen and air and fed into the burner tube of the reactor at 2100K, as described in Figure 2.1.

*Excerpts of this chapter have been published: Bailly M. and Kontopoulou M. "Nanocomposite blends containing polyolefins" in “Advanced Polyolefin Nanocomposites" Ed. Vikas Mittal, CRC Press, Taylor and Francis, 2011.

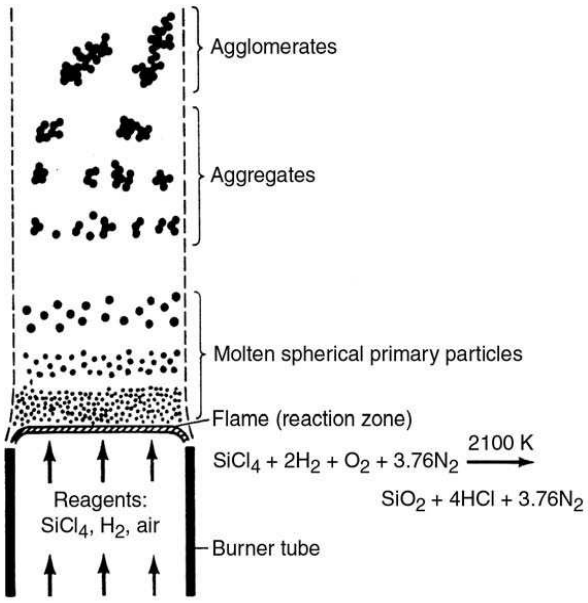

Figure 2.1 Fabrication process of fumed silica. From [31].

Upon cooling the primary particles of silica collide and form aggregates during the solidification process. Fumed silica is an amorphous grade because of the extremely fast cooling process, which takes a few thousandths of a second.

2.1.2 Surface chemistry

The surface of silica particles is mainly composed of silanol groups, as seen in Figure 2.2. Chemical and thermogravimetric analysis indicate that there are approximately 3 to 4.5 hydroxyl groups per square nanometer of silica surface, making it highly hydrophilic [1].

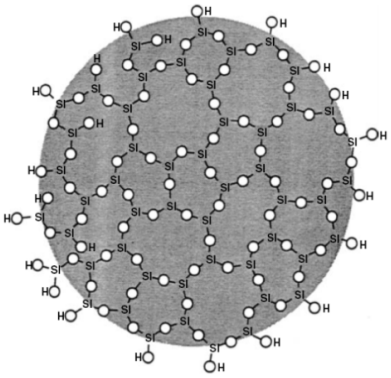

Figure 2.2 Schematic representation of a dehydrated but fully hydroxylated colloidal silica particle. The fourth oxygen coordinated with Si is above or below the plane of the paper. From [31].

More precisely, different groups involving Si-O bonds can be found at the surface of the particles, shown in Figure 2.3:

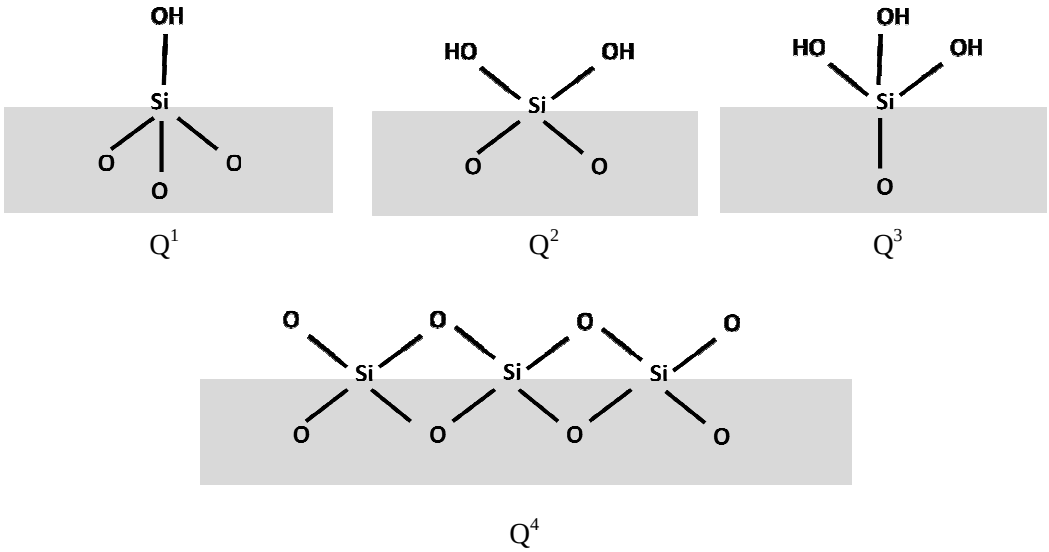

Q^1 Q^2 Q^3

Q^4

Figure 2.3 Representation of silanol groups Q^1, Q^2 and Q^3 and siloxane groups Q^4.

- Silanol groups. They have been classified according to the NMR-related Q^n terminology, where n is the number of bridging hydroxyl groups bonded to the central silicon. Three types of silanol groups exist (Q^1, Q^2, Q^3).
- Surface siloxane groups (Q^4).

Silanol groups have been also found within the particles and called internal silanol groups. It has been estimated that they represent 20% of the global silanol population. Silanol groups are characterized by an FT-IR absorbance at 3750 cm^{-1}. Water can be hydroxylated at the surface through the formation of hydrogen bonds with any of the surface silanols described above, therefore fumed silica has 0.5-2.5% moisture content upon manufacturing. The adsorbed water molecules can be removed from the particles' surface via an appropriate drying process.

The surface chemistry of silica can be quantitatively characterized by the Brunauer-Emmet-Teller (BET) technique to measure the SSA of the particles [32]. This measurement basically represents the ability of the silica particles to adsorb nitrogen. The SSA is expressed in m^2/g and ranges from approximately 50 to 400 m^2/g depending on the grade of silica.

When the particles are embedded into a polymer matrix, the hydroxyl groups tend to attract each other via hydrogen bonding. These hydrogen bonds between particles constitute the main F/F interactions, which force the particles to stick together and form aggregates –few nm-, agglomerates –dozens of nm- and clusters –up to the μm. Direct consequences of strong F/F interactions can be seen through thermal annealing experiments. Formation of large aggregates, which affected the rheological properties of PEO/SiO_2 nanocomposites were observed upon annealing by Zhang and Archer [33] proving that non-modified particles naturally tend to form aggregates.

2.2 Polymer/Silica Nanocomposites

2.2.1 Preparation

There are many processing methods for the synthesis of composites containing silica in a thermoplastic matrix including solution blending, sol-gel processes and in-situ polymerization. Figure 2.4 represents the three methods of fabrication of polymer/silica nanocomposites.

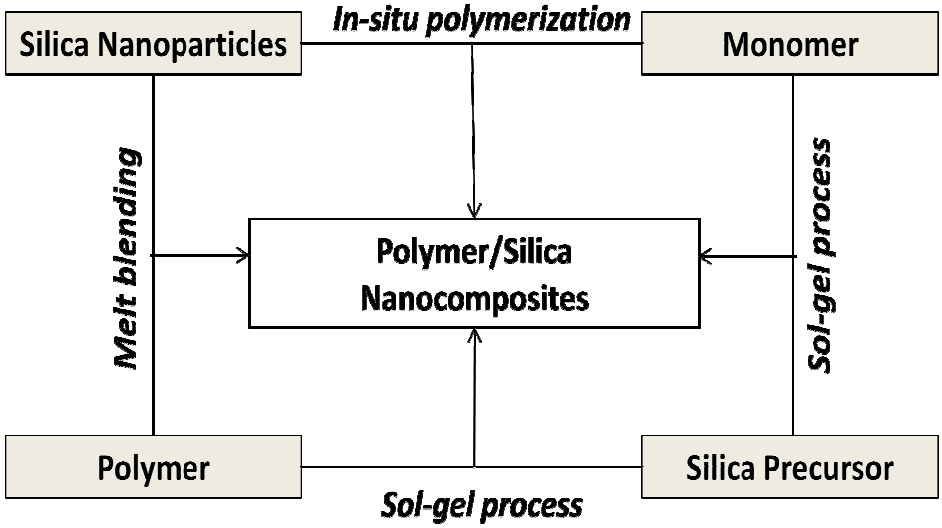

Figure 2.4 Representation of the three approaches in the preparation of polymer/silica nanocomposites. Adapted from [10].

Melt compounding is very versatile, as it provides a high degree of flexibility in the choice of compositions and can be implemented by small to medium size compounders at a reasonable cost.

Batch mixers are widely used in research because the operating conditions and the time at which the fillers and/or other additives are incorporated can be varied during a cycle to achieve optimum mixing. This is especially appreciated when chemical reactions are occurring during mixing, e.g. matrix functionalization. Continuous mixers, e.g. single and twin-screw extruders are more popular in the industry, offer higher throughputs, reduced manpower requirements and greater product uniformity, leading to easier quality control. Disadvantages include less processing flexibility and the need of expensive feeding equipment.

Among the different kinds of commercially available nanosilica, fumed silica remains the most popular. It has been used as a reinforcing agent with a wide range of thermoplastic matrices including polyolefins (PE, PP, PE-based copolymers), polyamides (PA6, PA-66), PMMA, PC, PS, PET, etc [10]. The silica concentration remains usually below 12wt%, as it is more difficult to achieve a fine state of dispersion at high silica concentrations.

2.2.2 Thermodynamic approach

2.2.2.1 Filler/Filler interactions

As the F/F interactions are mainly responsible for the difficulty to achieve a fine state of dispersion, it is important to have tools that can quantitatively estimate the degree of polarity of the nanofillers and by extension their ability to form F/F interactions.

The surface free energy of a solid (γ_s) is complimentary to the SSA as it provides quantitative information about the surface chemistry of the particles. It can be expressed as a sum of two components: γ^d (the dispersive component) describing London-type interactions between fluctuating dipoles and γ^{sp} (the specific component) that includes all the other interactions, such as: polar interactions, γ^p, hydrogen bondings, γ^h and acid-base interactions γ^{ab} [34].

The free energy of a solid is thus:

$$\gamma_s = \gamma_s^d + \gamma_s^{sp} \quad (2.1)$$

with $$\gamma_s^{sp} = \gamma_s^p + \gamma_s^h + \gamma_s^{ab} \quad (2.2)$$

Two methods can be used for the assessment of γ_s and its components: contact angle measurements and Inverse Gas Chromatography (IGC) [35]. Chibowski and Perea-Carpio in [36] reviewed the problems encountered for the determination of the surface free energy of powdered solids like silica using the contact angle technique.

2.2.2.2 Polymer/Filler interactions

One way to quantify the adhesion between two materials is to estimate the work of adhesion (W), i.e. the energy required to separate two materials that were previously adhered. Logically, the greater the attraction between the materials, the greater the work of adhesion will be. The work of adhesion is related to the interfacial tension (γ) between the two materials as the smaller the interfacial tension, the greater the affinity and therefore the greater the work of adhesion will be. It is therefore imperative to have access to surface and interfacial tension data in order to predict the adhesion between the two phases. The experimental techniques to measure the surface and interfacial tensions of polymer melts were reviewed by Wu [34].

Based on this framework, Wang et al. examined in [8] the change in the work of adhesion, ΔW, from a well dispersed system, where a filler particle is surrounded by polymer, to filler agglomeration where each filler particle is neighboring by another filler particle:

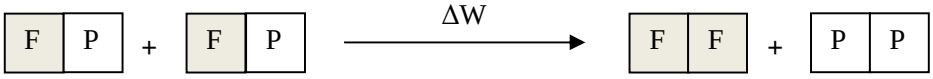

Figure 2.5 Simulation of the agglomeration process. From Wang [8].

Using the considerations stated above, an expression of ΔW as a function of the surface characteristics of the filler and the polymer, as well as the contributions of the different intermolecular forces to the works of adhesion can be obtained:

$$\Delta W = 2[\sqrt{\gamma_f^d} - \sqrt{\gamma_p^d}]^2 + 2[\sqrt{\gamma_f^p} - \sqrt{\gamma_p^p}]^2 + 2\left[W_f^h + W_p^h - 2W_{fp}^h\right] + 2[W_f^{ab} + W_f^{ab} - 2W_{fp}^{ab}] \quad (2.3)$$

The subscripts *f* and *p* are for *filler* and *polymer*. The superscripts *d*, *p*, *h* and *ab* are for *dispersive*, *polar*, *hydrogen*, and *acid-base* interactions.

The value of ΔW will determine whether the system will have the tendency to agglomerate: a value of ΔW=0 will signify that the attractive potential between filler particles disappears; therefore an optimum dispersion of the filler inside the matrix can be obtained. This condition is met if the dispersive and polar components of the surface tension of the polymer and filler are equal, i.e. the surface energy characteristics of the filler and polymer surface are identical.

If this is not the case, the values of the adhesive energies between polymer and filler due to hydrogen bonding, acid-base interactions or any other type of specific interactions must be sufficiently high to offset the effect of the difference in surface energies.

In the case of polyolefin/unmodified silica particles, the interactions are naturally very poor between the hydrophilic silica surface, which has a high surface energy, and the extremely non-polar polyolefin chains, with low surface tension. Therefore particle modification and/or matrix functionalization techniques are needed to enhance the compatibility between the matrix and the fillers through either lowering the surface energy of the filler in the former case, or increasing the adhesive energies between the polymer and filler surface in the latter, leading to the approaches described in the next two subsections.

2.2.3 Surface treatments

F/F interactions consist of hydrogen bonding between the silanol groups present at the nanoparticle surface, making the dispersive mixing of nanoparticles during melt compounding a challenging task. If the processing conditions can be tuned to improve the quality of mixing, for example by lowering the mixing temperature leading to higher shear rates during compounding, the most effective strategies involve the modification of the surface chemistry of the nanoparticles. Indeed, the very hydrophilic nature of its surface makes it incompatible with most of the non-polar polyolefins such as PE and PP. Approaches involving physical and chemical methods have been developed, aiming at disrupting the hydrogen bonding occurring between the particles and also enhancing the affinity with the hosting polymer chains [8,10,15].

Physical methods involve the adsorption of surfactants or macromolecules at the surface of the particles. Surfactants present a hydrophobic tail and a hydrophilic head. The polar groups of the species are the preferential sites for adsorption via polar interaction, hydrogen-bonding or acid-base interaction, while the non-polar groups of the adsorbed species tend to render the particles more hydrophobic and therefore improve the compatibility with the matrix. Different kinds of

surfactants have been used such as stearic acid [37], oleic acid [38] and poly(ethylene glycol) [39].

The chemical modification techniques consist of grafting monomers, or macromolecules on the silica particles, with the same goal of turning the particles more hydrophobic, while at the same time promoting the P/F interactions. Two different kinds of agents are to be considered depending on their functionality: the monofunctional agents also called “coating agents”, which hold only one reactive site used for the grafting reaction onto the particle, and the bifunctional, or coupling agents.

The monofunctional agents include silane functional groups, such as dimethyldichlorosilane [40-42]. Gunko et al. reviewed different silane agents and monitored the reduction of the hydrophilic properties [43]. Zhang and Archer [33] coated the particles with PEO macromolecules with the aid of a silane end-group, while Wu et al. [44] first used a simple silane coating agent and then added an extra coating layer of matrix polymer chains.

The bifunctional agents have two reactive groups, one grafted onto the silica surface and one aiming at a direct reaction with the polymer matrix. Both terms of coating and coupling agents are often the subject to confusion in the literature: the term coupling agent should only be used for a bifunctional agent that can react with the polymer matrix. The general structure of the bifunctional agents can be represented as $RSiX_3$ where X is the hydrolysable group –typically chloro, ethoxy or methoxy - and R is a functional group to ensure compatibility with the polymer matrix. Although coupling agents have been very popular in micro-scaled fillers, such as glass fibers, they have not been widely implemented in nanocomposites for no apparent reasons.

Grafting macromolecules onto the surface of silica particles is a recent technique, which can be implemented in two ways: the macromolecules can be grafted directly or via a coupling agent

(often a silane-based monomer). When macromolecules are grafted directly, two techniques are implemented: the “grafting to” method which involves the attachment of end-functionalized polymers and the “grafting from” -also called “surface-initiated polymerization”- method which deals with the growth of polymer chains from immobilized initiators located on the silica particles, leading to “hairy nanoparticles” or “polymer brushes”. This method has mostly been implemented with radical polymerization involving polystyrene [45,46]; many other types of polymerization have been tested [47]. It can also be more easily achieved via a first step, consisting of grafting a silane coupling agent [16].

Besides all the aforementioned methods, grafting polymers onto silica nanoparticles can also be realized through irradiation [44,48,49], or using the sol-gel preparation technique to synthesize the silica *in-situ* [13]. In comparison with the physical methods, chemical modification usually leads to more significant improvements due to the non-reversible nature of the reaction and the stronger P/F interactions.

2.2.4 Matrix functionalization

Similarly to the surface treatments of nanofillers, matrix functionalization aims at strengthening the P/F interactions. It can be achieved by grafting monomers capable of establishing physical or chemical interactions with the hydroxyl groups of the silica particles. Maleic anhydride has been very popular among the monomers available for grafting on polyolefins. Maleated polyolefins have been used extensively as compatibilizers between inorganic particles -including layered silicates and silica- and the polyolefin matrix [14]. Furthermore, various monomers containing silane functional groups have been successfully grafted onto PE [50], PP [51,52], and ethylene-α-olefin copolymers (ECs) [53,54], using a peroxide initiated grafting process. Although the

primary application of silane-grafted polyolefins is toward crosslinking using moisture curing [53,55], these materials may hold great promise in composite technology as well. Parent et al. investigated the competition between the peroxide-initiated grafting and cross-linking reactions in [54]. Scheme 2.1 depicts the different stages of the peroxide mediated grafting process: first the peroxide releases free radicals upon heating, which form macro-radicals after reaction with the polymer backbone before the propagation takes place and ceases by radical recombination.

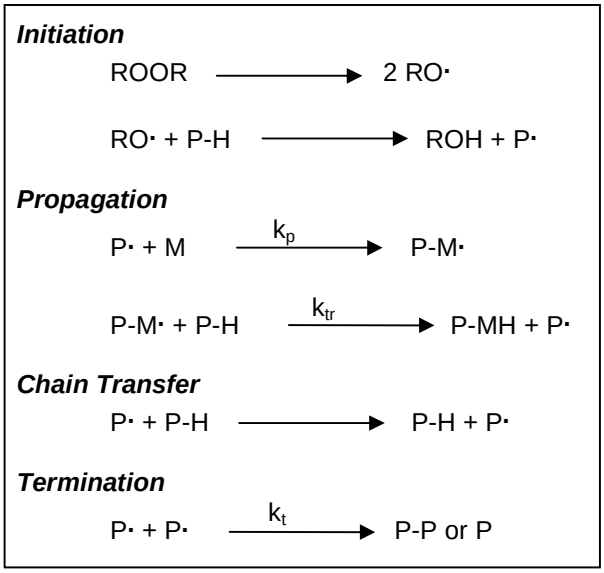

Scheme 2.1 Generic reaction scheme of PP functionalization. ROOR is the initiator, “P” is for Polymer, “M” for Monomer, “H” for hydrogen. The dots represent the radicals.

2.2.5 Polymer/Filler interactions

It is well-established in composite technology that the degree of reinforcement of the matrix lies upon the ability of the fillers and the matrix to form strong interactions in order to transfer the

load applied from the matrix to the rigid nanofillers. P/F interactions are therefore of primary importance, especially in the polymer nanocomposite technology given the extremely high surface area of the nanofillers [33]. Links between the polymeric matrix and the fillers can be formed through either physical or chemical interactions. Physical interactions have been extensively reported in rubber/silica and rubber/carbon black composites [8,9] and involve physical adsorption of the polymer chains onto the surface of the particles. Hydrogen bonding and acid-base interactions are examples of physical interactions, which can result in strong associations between the polymer and the filler particles.

Chemical interactions are established if the fillers and the matrix are associated via covalent bonding. This can be achieved by using coupling agents or by functionalizing the matrix in order to establish a reaction with the functional groups present at the particle surface.

An interesting consequence of the presence of strong P/F interactions is the development of a layer of immobilized or "bound" polymer in the vicinity of the particles, which is sometimes called a "shell". The reduced mobility of the chains can be detected by a shift of the T_g towards higher temperatures [8]. As an example, Wu et al. reported a 10% rise in the T_g upon addition of 9 wt% silica in a maleated polyolefin elastomer matrix [56].

The term "shell" is more appropriate in the case of a low-molecular weight matrix, which would form a "monolayer" upon adsorption onto the filler surface. The shell thickness therefore will generally be not much thicker than the molecular dimensions of the matrix material. If the filler loading is high enough, the shells may overlap, promoting the formation of a "polymer-filler network". On the other hand, the presence of long chains in higher molecular weight matrices would result in a "chain bridging" effect, where two particles are effectively bridged by one or more polymer chains. This is illustrated in Figure 2.6.

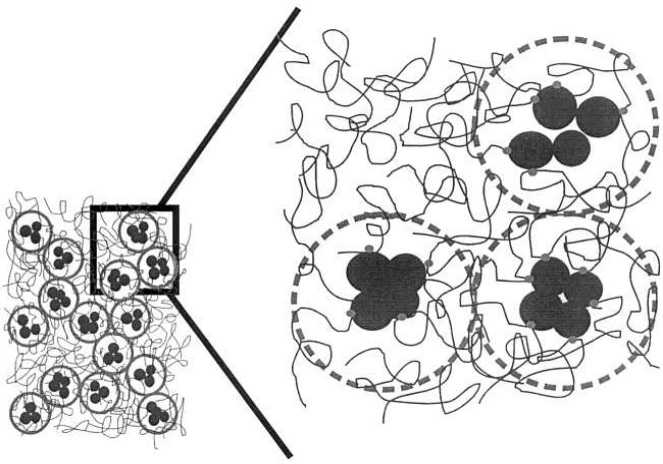

Figure 2.6 Schematic illustration of the polymer-mediated network with a close-up of the adsorption of polymer chains on the filler aggregates. From [57].

In practice it is very difficult to quantify the extent of P/F interactions. Qualitative studies of the P/F interactions have been mostly restricted to FT-IR spectroscopy, aiming at revealing the presence of covalent bonds between the fillers and the matrix. For example, the reaction between the alkoxysilane functionality and the hydroxyl groups of the silica surface has been well documented for composites containing glass fibers [58-60], alumina and silica particles [16,61].

The presence of interactions can also be detected by the measurement of "bound polymer" (BdP), which consists of estimating the amount of polymer bound to the particles after removal of the non-attached or free chains by dissolution in an adequate solvent. Suitable solvents can be chosen to dissolve either only the covalently bound rubber or the rubber which is both physically and chemically attached [9]. On the other hand, treatment of the particles by simple coating agents will tend to disrupt physical and chemical bonds by shielding the particle from its surroundings, thus resulting in the absence of such a bound layer.

From a more phenomenological standpoint, these interactions can be quantified based on mechanical property characterization, under the terminology of “interfacial adhesion”, as proposed in the model developed originally by Pukanszky and Turcsanyi [62]. To take into account the bonding between the fillers and the matrix, they introduced a parameter B, which has no direct physical meaning but is connected with the interfacial properties. This model was applied in case of PP/modified silica in [16,40] where higher values for B were found when treated particles were used, indicating stronger interfacial adhesion.

A similar approach involving the calculation of the Interfacial Shear Strength (IFSS) applicable to micro-scaled fillers was used in [58]. Attempts to bridge over the adhesion theory with the theory based on thermodynamics have also been made through the calculation of the work of adhesion (W), derived from the expression of the surface energies of the fillers and the polymer. This has been done quite extensively in micro-scaled fillers [63] but more rarely in nanocomposites [16,64].

2.2.6 Rheological properties

The influence of nanofillers on the rheological behaviour of rubbers has been investigated extensively since the 70’s. Wang published in 1998 a comprehensive review on the effects on the rheology of P/F and F/F interactions in silica and carbon black-filled vulcanizates [8]. Leblanc did the same work for more recent publications in 2001 [9] with particular attention on the effect of bound rubber. More recently, Cassagnau [65] presented a review of organoclay and fumed silica-filled thermoplastics. The effects of nanosilica both inside and outside the linear viscoelastic (LVE) region were discussed. The LVE region is observed at very small deformations, where the response of the material is independent of the deformation. The main

findings are that during frequency sweeps, filled polymers show deviations from the terminal flow behaviour. Significant changes in the rheological behaviour have been observed past a certain filler loading, pointing to the existence of a "percolation threshold". These changes include the appearance of a secondary plateau for the elastic modulus, where the moduli become essentially independent of frequency. This has been called a "solid-like" behavior [65] and is accompanied by the presence of a yield stress. This phenomenon seems to have a complex dependence on the filler loading, the morphology and the nature and degree of F/F and P/F interactions.

Outside the linear viscoelastic region, where deformations are high enough to alter the unperturbed polymer structure, the magnitude of the dynamic properties of a filled polymer has been found to be dependent on the extent of deformation. This phenomenon is known as the "Payne effect" and was observed first in carbon black-reinforced rubber [66]. Again, the morphology, the interactions between fillers and matrix as well as filler loading have an influence on the limit of linearity –i.e. the critical deformation at which the dynamic properties start to drop.

Other interesting works in the non-linear region involve the moduli restoration following a large strain perturbation, also known as "thixotropy". Indeed, a filled polymer might present the ability to recover its structure after being deformed depending on various parameters such as the rest-time. The structural recovery can also be determined by measuring the linear viscoelastic properties after cessation of different pre-shear rates and applied rest-times.

Finally, other effects have been studied like the time dependency of the dynamic properties in the linear region. Thermal annealing experiments employ annealing of the samples in the melt state for a given time, to allow for complete microstructural equilibration prior to rheological testing.

Zhang and Archer observed significant differences between the annealed and non-annealed nanocomposites, claiming for a re-arrangement of the particles in order to approach the thermodynamic equilibrium [33].

Additionally, the rheological properties of the nanocomposites are deeply dependent on the silica concentration. At high filler loadings, a filler network, leading to "percolation" can be formed. Percolation is a concept first observed experimentally by the change in the electrical conductivity of a composite material provided that the filler loading was high enough to ensure a direct inter-particle contact or "filler-filler network". According to the percolation theory, the critical filler loading for randomly dispersed spherical particles should be around 30 vol% [33].

When direct connections occur between fillers and the polymer chains, the formation of a "polymer / filler network" has been proposed, consisting of the filler and the bound polymer chains. These lead to a percolated network at filler concentrations much lower than those predicted by the percolation theory. If the outer shell is thick enough, leading to an effective volume fraction that is very different from the actual volume fraction, then the formation of a percolated network can occur even at filler loadings as low as 1.2 vol% [65] or 2 vol% [33]. The effective volume fraction can be calculated with the Guth-Smallwood equation [67]:

$$G_N(\phi_e) = G_N(0) \cdot (1 + 2.5\phi_e + 14.1{\phi_e}^2) \quad (2.4)$$

where $G_N(\phi_e)$ is the plateau modulus (Pa) as a function of ϕ_e the effective volume fraction (vol%).

Based on their rheological characterization, Zhang and Archer found an effective volume fraction about five times higher than the real volume fraction in PEO/modified silica composites [33]. An

increase in the effective volume fraction can also result from the presence of polymer that is trapped within filler aggregates.

2.3 Polymer Blends containing Nanosilica

2.3.1 Filler Localization

As most polymer blends are thermodynamically immiscible and consequently exist as two-phase systems, the fillers might be located at different locations, considering that the particles distribute unevenly between the two phases in the overwhelming majority of systems: either inside the matrix (thermoplastic polymer), within the elastomeric phase, or at the interface between the two phases. It is generally acknowledged that two distinct factors contribute to the final localization of the fillers: thermodynamic effects, based on the affinity that the fillers might have with the polymers, and kinetic effects that include the mode of preparation of the composites and the ability of the fillers to migrate to a different location, i.e. from one phase to the other or from one phase to the interface. These factors are critical in the prediction and control of the filler localization.

2.3.1.1 Thermodynamic effects

When fillers are introduced into a polymer blend, they generally tend to migrate to the phase with which they have the most affinity. The affinity between polymers and fillers has been described qualitatively via the study of the surface chemistry of both phases under the terminology of polymer/polymer (P/P) and P/F interactions.

Sumita et al. proposed a criterion to predict the morphology based on the calculation of the interfacial tensions between the different components, which has been applied in recent publications by the research group of Cassagnau [68,69]. The same group published a comprehensive review article on the topic [70]. The criterion is based on the tendency of the system to minimize its total free energy; as a result fillers will tend to go to the phase with which they have the strongest affinity and therefore the lowest interfacial tension.

While P/P interfacial tensions have been experimentally obtained for various systems, P/F interfacial tension data are almost non-existent in the literature due to the difficulty of experimental measurements in the case of dispersed solids like silica nanoparticles.

The wetting coefficient is defined as:

$$\omega = \frac{\gamma_{filler-2} - \gamma_{filler-1}}{\gamma_{12}} \qquad (2.5)$$

And the criterion is:

- If $\omega > 1$ The filler particles distribute within the phase 1
- If $-1 < \omega < 1$ The filler particles distribute at the interface 1-2
- If $\omega < 1$ The filler particles distribute within phase 2

As expected, the greater affinity of a filler to a certain phase is strongly correlated with the relative value of the interfacial tension, which in turn depends on the nature of the P/F interactions. The bigger the affinity between polymer and filler, the lower the interfacial tension will be. Consequently, a preferential localization of the fillers can be obtained by functionalizing

the elastomeric phase [26], by adding a compatibilizer [71,72], by modifying the surface chemistry of the particles [68,69,73-75] or by functionalizing the matrix [74].

Limitations of this criterion include strong discrepancies for surface tension data, due to the issue of extrapolation to reach the melt temperature. Also, it does not take into account the processing time and procedure by assuming that thermodynamic equilibrium is attained, which is obviously not the case experimentally.

Nevertheless this criterion has been successfully applied in filled polymer blends regardless of the nature of the fillers, being carbon black [76], silica [68,69], or nano-$CaCO_3$ particles [64,77]. Alternatively, some papers based their analysis on the values of the work of adhesion, W and the interfacial tensions rather than ω [73,74].

2.3.1.2 Kinetic effects

Based on the thermodynamic considerations mentioned above, when the components of a ternary nanocomposite are introduced simultaneously in the compounding device, the fillers should localize within the phase with which they have the largest affinity. However in some cases experimental observations showed disagreements between predictions and experiment, shedding light on the importance of multiple other factors that do not solely depend on the thermodynamic affinity between the polymers and the fillers. These factors are commonly classified as "kinetic effects" and are related to: (1) the physical properties of the polymers, (2) the time during which the components are mixed, and (3) the compounding sequence.

Firstly, physical properties such as the melting temperature and the viscosity of the polymers dictate to a large extent the medium in which the fillers will be localized. Generally speaking, when there are significant differences in the viscosities or melting temperatures, the fillers tend to

localize within the less viscous polymer, or within the polymer with the lowest melting point [78,79].

Secondly, the sequence followed when the components are introduced into the compounding device can potentially determine the filler localization, regardless of any thermodynamic considerations. The blending sequence can be varied by changing the order of introduction of the components: (1) all together at the same time (2) the two polymers first followed by the fillers (3) the matrix and the fillers first followed by the dispersed phase (4) the dispersed phase and the fillers first and then the matrix. Dasari et al. demonstrated the importance of the compounding procedure by testing the four blending sequences on Nylon-66/SEBS-g-MA/organoclay composites at an 80/15/5 wt% composition [80]. When procedures (1) and (2) were used, the organoclay platelets were equally distributed between the two phases, whereas in (3) and (4) they were located in the phase with which they were blended first. Obviously the different morphologies that they obtained had an impact on the properties of the composites, as discussed in the next two subsections.

2.3.2 Morphology

Depending on thermodynamic and kinetic considerations, the fillers may be located inside the matrix, within the dispersed phase, or at the interface. The resulting microstructure can be characterized as *encapsulated* if the fillers are embedded into the dispersed phase (Figure 2.7 (a)), *segregated* if the fillers and the minor phase are dispersed within the matrix (Figure 2.7 (b) and *core-shell* when the fillers remain at the interface and therefore form a “shell” surrounding the dispersed phase.

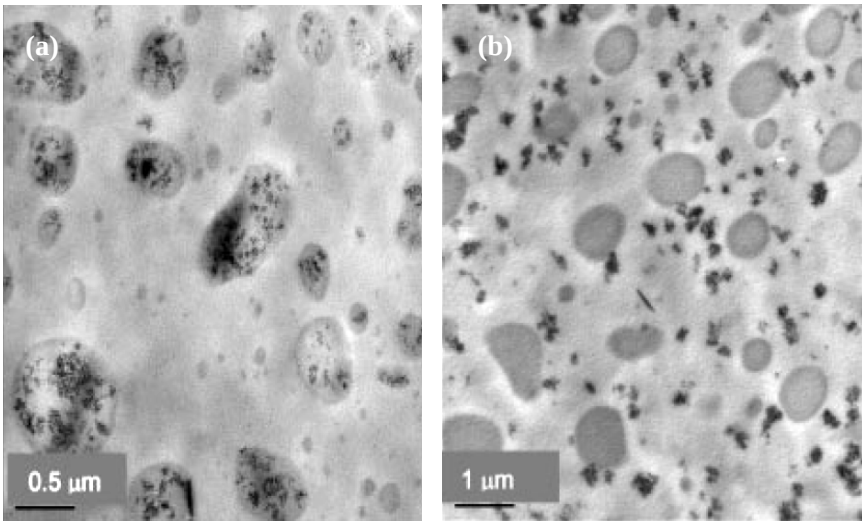

Figure 2.7 TPO blends containing 5wt% of silica, exhibiting segregated morphologies with the silica partitioning in (a) the dispersed phase, and (b) the elastomeric phase. The elastomeric phase appears darker. From [72].

These are the basic morphologies that might be obtained depending solely on the filler localization, but numerous other factors influence the phase structure.

Similarly to what has been observed in binary nanocomposites, the state of dispersion of the fillers also plays a crucial role in ternary nanocomposites. The mechanisms of dispersion remain the same as described in section 2.2.2, and therefore the same techniques are employed to facilitate the breakup of agglomerates: filler modification, matrix functionalization and addition of a compatibilizer. Moreover, in case of segregated and encapsulated morphologies, it is important to note that since the filler resides preferentially in one of the phases, the actual filler loading contained in that particular phase is increased. For example, in a thermoplastic matrix containing 30 wt% of impact modifier and 5 wt% of reinforcing filler, if the morphology is segregated the effective filler loading in the matrix would actually be 7.14 wt%.

Substantial reductions in the size of the domains of the dispersed phase, as well as narrowing of the particle size distribution, have been reported extensively, in various immiscible blends containing nanoclay or nanosilica fillers [69,71,73,81-85]. Indeed, the dimensions of the nanoparticles are comparable to, or smaller than, the domain sizes of many multiphase blends. This may enable them to interfere with the process of particle breakup and coalescence during compounding, thus resulting in changes of the blend morphology. In contrast to the traditional considerations of blend composition, viscosity ratio, mixing procedure i.e. shear rate, mixing time and mixing temperature that are well understood, the mechanisms through which nanoparticles affect the morphology of immiscible and partially miscible blends are still debated and the topic of intense investigation.

2.3.3 Mechanical Properties

Filled polymer blends have been developed to enjoy both advantages of the additions of rigid nanofillers and dispersed rubber particles. As reviewed by Zou et al. [10], silica-reinforced binary nanocomposites offer great enhancement in strength and stiffness, but at the expense of ductility –elongation at break- and impact toughness, whereas toughened polymers gain in toughness but loose in strength.

The same mechanisms applicable for the strengthening of thermoplastic are desirable in ternary nanocomposites, with the same requirements: a fine dispersion of the fillers is necessary in order to guarantee some reinforcement. Additionally to the filler dispersion, another prominent parameter in the morphology is the state of dispersion of the dispersed elastomeric domains. Indeed, as the dispersion of rigid fillers influences the reinforcement, the dispersion of the rubber

particles influences the toughening of the composites, as demonstrated by the groundbreaking work of S. Wu on polymer blends [19].

While the idea of combining both strengthening and toughening effects in the same material sounds great in theory, the synergistic effect due to both additions is not always observed experimentally because of the multiple morphologies that can be obtained according to the filler localization. Indeed, several authors observed that depending on the filler localization different mechanical properties are obtained. In the case in which the fillers are localized in the dispersed phase, Dasari et al. reported a decrease in toughness [80], while Liu and Kontopoulou remarked a significant reduction in strength and stiffness [72]. Both found some improvements in the mechanical properties when the fillers were localized in the matrix.

In another publication by Liu and Kontopoulou, in which the fillers are localized in the matrix, tensile and flexural properties have been improved by the addition of nanosilica while the introduction of the elastomeric phase (POE) led to a significant increase in the impact strength, proving the synergistic effect of POE and silica [71].

Interestingly, one paper by the group of Q. Fu [73] reports mechanical properties of similar materials (PP/EPDM/silica). The synergistic effect could not be achieved because of the core/shell morphology obtained in which silica particles surround the dispersed phase, therefore reducing the ability of the EPDM particles to act as impact modifiers and not being able to fully reinforce the matrix. It appears therefore that the localization of the filler plays a determinant role on the final properties of the ternary composite. This characteristic should be exploited accordingly, in an effort to optimize the properties of the composites, by synthesizing well-defined structures.

Chapter 3

MORPHOLOGY AND PROPERTIES OF POLYPROPYLENE/ETHYLENE-OCTENE COPOLYMER BLENDS CONTAINING NANOSILICA*

3.1 Introduction

Isotactic PP is a semi-crystalline polymer, which has been used in a wide variety of industrial applications because of its ease of processing, low density, remarkable stiffness and relatively low cost. However, its use has been limited by its brittleness at low temperatures.

The impact resistance of PP can be improved with the addition of impact modifiers such as EPR, EPDM and various POEs [20,86-89]. Compared with the traditionally-used EPDM and EPR, POEs exhibit improved processability and better dispersion when blended with PP. They have been used widely to provide enhanced impact properties for automotive exteriors and interiors and other applications requiring superior low temperature performance [20,89-96].

To provide PP an optimum balance of toughness and stiffness, elastomers such as EPR, EPDM and POEs have been added, as well as inorganic micro-sized fillers including $CaCO_3$, SiO_2, talc, $BaSO_4$, etc [33,71,97-105]. It has been shown that nanosilica particles can be used to preferentially reinforce PP, while taking advantage of the toughening effect of the elastomeric dispersed phase [71,72,106].

* In preparation for submission to Macromolecular Materials and Engineering

The objectives of the present Chapter are twofold: Firstly to present a detailed examination on the morphology development and mechanical properties of PP/EOC blends filled with silica nanoparticles over the entire composition range. Secondly to elucidate the mechanisms governing the stabilization of the size of the dispersed phase in the presence of nanoparticles, by observing the morphology evolution upon annealing and upon application of simple shear flow.

3.2 Experimental

3.2.1 Materials

Polypropylene homopolymer, Escorene PP 1042, MFR 1.9 g/10 min at 230 ºC, was supplied by ExxonModil Chemical. Maleated PP (PP-g-MA), Fusabond® PM 613, MFR 49 g/10 min at 230°C containing 0.55 wt.% of maleic anhydride, was supplied by E.I. DuPont Canada. A commercial grade poly (ethylene-*co*-octene) (Engage 8100), containing 24 wt.% of comonomer with density of 0.87 g/cm^3 and melt flow index of 1.0 g/10min (at 190 ºC) was provided by Dow Chemical. Nanosilica (oct-SiO_2), Aerosil® R805, with a specific surface of 150±25 m^2/g and mean particle size of 12 nm, surface modified by octylsilane was supplied by Evonik Industries. Irganox 225 antioxidant was obtained from Ciba-Geigy.

3.2.2 Compounding procedure

All components were introduced simultaneously in a Werner & Pfleiderer ZSK-30 (L/D=40, D=30.7mm) co-rotating twin screw extruder using the screw configuration shown in Figure 3.1. The screw configuration was comprised of four kneading disc blocks and two reverse pumping screw elements. This configuration was chosen following extensive experimentation, aiming at obtaining a fine dispersion of the secondary phase.

Figure 3.1 The screw configuration used in the compounding experiments

Blends containing different PP/EOC compositions (in wt%: 70/30, 60/40, 50/50, and 30/70) were prepared at a feed rate of 2.5 kg/hr and a screw speed of 200 rpm. Composites containing 5 phr (4.8wt%) of oct-SiO_2 with and without 10 phr (9wt%) of PP-g-MA were prepared under the same conditions. Antioxidant at 0.3wt% was added to all formulations. The temperatures profile of the extruder from feeding to the die was 60 ºC-200 ºC-205 ºC-205 ºC-210 ºC-210 ºC-200 ºC for all blends.

3.2.3 Mechanical properties

Tensile properties were measured using an Instron 3369 universal tester, at crosshead speeds of 50 mm/min. Dumbbell-shaped specimens were cut with a Type V die according to ASTM D638 from 1.5 mm thick sheets, which were prepared by compression molding of the compounded samples at approximately 200ºC and 10 MPa using a Carver press.

Flexural tests were performed according to ASTM D790, procedure B, at a speed of 13.65 mm/min. Rectangular bars of dimensions 127x12.7x3.2 mm were produced by compression molding at 200 ºC. Notched Izod impact tests were carried out on an Instron BLI impact tester at room temperature according to ASTM D 256. Specimens of dimensions 64x12.7x3.2 mm were prepared by compression molding at 200ºC. At least 5 specimens were tested for each sample and the average values were reported.

3.2.4 Microscopy and image analysis

For SEM observations, samples were first hot pressed at 190°C, 10 MPa for 1 min, then immersed in liquid nitrogen for 5 min before brittle fracture. The elastomer phase was removed after etching in n-heptane for 2.5 hours at 80°C. The etched surfaces were observed on a JEOL JSM-840 scanning electron microscope. The SEM images were analyzed by using the Sigma Scan Pro image analysis software to estimate the average diameters of the dispersed elastomer phase. A characteristic size, corresponding to the Feret diameter was then calculated based on the estimated area, A, according to:

$$D = \sqrt{\frac{4A}{\pi}} \tag{3.1}$$

3.2.5 Rheological characterization

Rheological characterization was carried out on a Reologica ViscoTech oscillatory rheometer using 20 mm parallel plate fixtures, with a gap of 1 mm at 190ºC, under nitrogen blanket. The rheometer was operated in the dynamic oscillatory mode in the linear viscoelasticity region. The complex viscosity (η*), elastic modulus (G') and tan δ were measured as a function of angular frequency (ω).

3.2.6 Morphology evolution upon time and steady-shear

Annealing experiments were performed by leaving the compounded samples on a hot stage at 180°C for times ranging from 1-60 min and subsequently immersing them in cold water.

To monitor the effects of shear, the samples were first subject to a creep experiment with the same equipment as described above under 100 Pa at 200°C until a strain of about 9.4 was reached. Once the experiments were completed, the samples were rapidly cooled down to 60°C and removed from the rheometer. They were then immersed into cold water and freeze fractured at ¾ of the disk radius in liquid nitrogen. The elastomer phase was etched in n-heptane at 80°C for 2.5 hrs. The etched surfaces were observed under SEM.

3.3 Results

3.3.1 Rheological properties

The dynamic oscillatory functions of the base materials as a function of the angular frequency are presented in Figure 3.2. The compatibilized PP, PP/PP-g-MA, displays slightly lower values of complex viscosity due to the addition of PP-g-MA, which has a much lower viscosity than the unmodified PP due to its lower molecular weight.

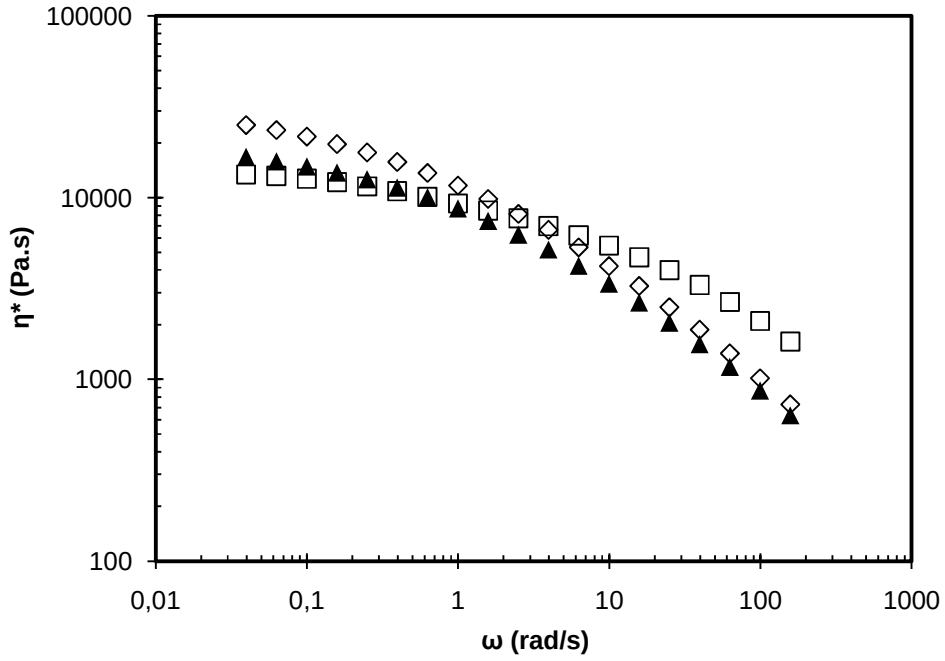

Figure 3.2 Complex viscosities of PP, EOC, and PP/PP-g-MA. Symbols are (◇) PP, (□) EOC, (▲) PP/PP-g-MA.

3.3.2 Morphology

The SEM micrographs of PP/EOC blends at different compositions are shown in Figure 3.3. In the absence of compatibilizer, EOC exists as a dispersed phase up to a 60/40 PP/EOC ratio. As the concentration of the dispersed phase increased, the shape of the particles became less spherical. A co-continuous morphology was obtained at the 50/50 PP/EOC composition, whereas phase inversion occurred at 30/70, with EOC becoming the major phase (in Figure 3.3 (d) corresponding to this blend, the dispersed PP particles can be clearly seen – the EOC matrix has not been etched).

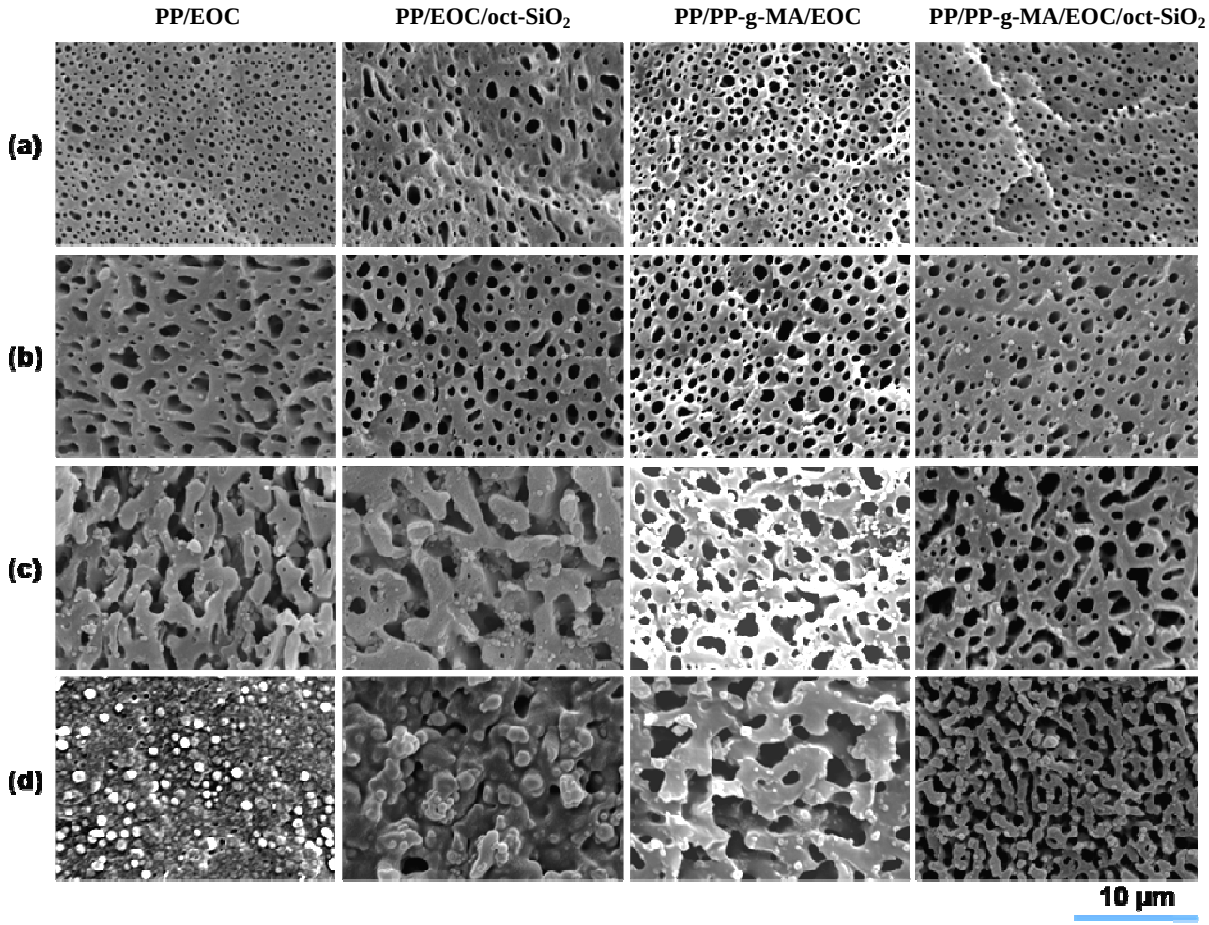

Figure 3.3 SEM photomicrographs showing the effect of silica on the EOC domain size at different EOC contents: (a) 70/30; (b) 60/40; (c) 50/50; (d) 30/70. Scale bars represent 10 µm. All samples were etched except PP/EOC at 30/70.

Addition of 5 phr silica to the blends did not affect significantly the morphology up to the 50/50 ratio (see also Figure 3.4). However, phase inversion and the co-continuous morphology seems to persist at the 30/70 PP/EOC ratio.

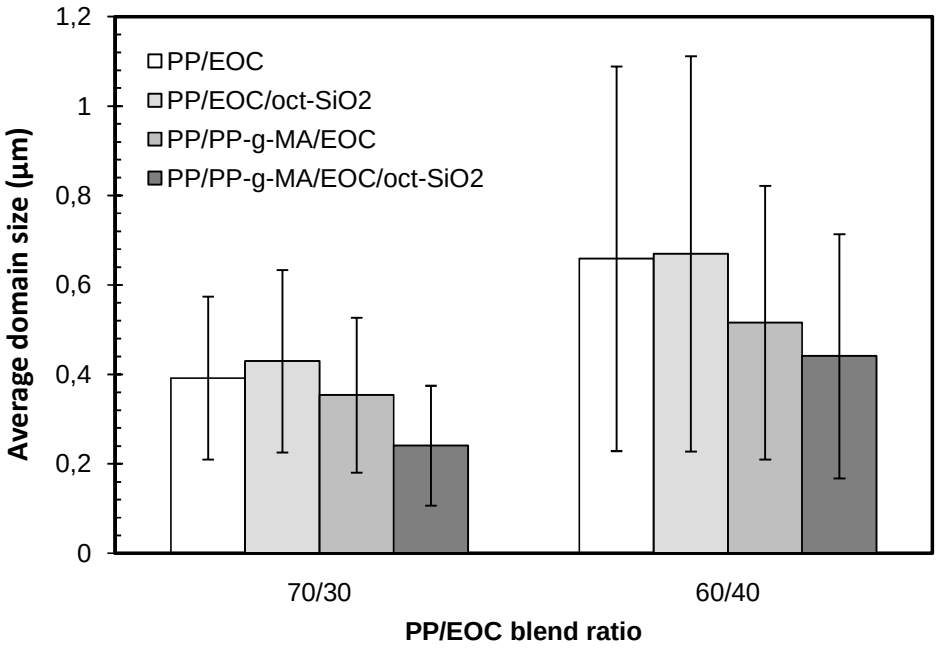

Figure 3.4 Average EOC domain size showing the effect of silica and PP-g-MA on the PP matrix as a function of PP/EOC blend ratio.

Maleated PP is commonly added as a compatibilizer in order to enhance the affinity between the nanosilica particles and the polymer chains, thus improving the dispersion of the nanoparticles [14,59,71,72,107]. The effects of the addition of PP-g-MA in the PP/EOC blends were twofold: Firstly the addition of PP-g-MA made the effective concentration of the (PP+PP-g-MA) matrix greater than the original PP concentration. Secondly, PP-g-MA having a significantly lower molecular weight than pristine PP, it also has a lower viscosity. The resulting lower viscosity of the matrix, (see Figure 3.2) might have influenced the phase inversion composition, to such an extent that a co-continuous structure is observed up to the 30/70 PP/EOC composition.

Addition of nanosilica particles to the (PP/PP-g-MA)/EOC blends led to a further refinement of the size of the dispersed phase, as shown in Figure 3.4. It also resulted in a significantly finer co-

continuous structure, as shown in Figure 3.3 (d). The effect of nanosilica on the co-continuous structure is discussed in detail in a paper by Lee at al. [106], who suggested that the competition between break-up and coalescence is affected during compounding in the presence of nanoparticles, thus resulting in altered morphologies.

It is important to note that the addition of nanosilica particles led only to smaller EOC domains when PP-g-MA was used as a compatibilizer. This suggests that a reduction in size happens only when the nanosilica particles are well-dispersed within the matrix, in the presence of a compatibilizer.

3.3.3 Morphology evolution upon time and steady-shear

Even though the effect of nanofillers on the microstructure of the polymer blends has been widely reported [14,69,71,83] and several explanations have been offered, the phenomenon has not been studied adequately to date. It is obvious that in the presence of nanoparticles, the break-up and coalescence of the dispersed phase may be affected. Lee et al. [106] who investigated PP/EOC blends at the phase inversion composition speculated that in the presence of nanoparticles droplet breakup is facilitated by the high stresses that develop locally. Additionally, the droplets of the dispersed phase are forced to follow a highly tortuous path, corresponding to conditions of highly confined flow. However, they did not find any evidence of an altered coalescence mechanism.

In this work we attempted to investigate the effect of the addition of nanofiller on the coalescence process, by conducting two types of experiments, in the absence of shear (annealing), according to the procedures described in references [108-110] and upon application of steady shear flow within the rheometer.

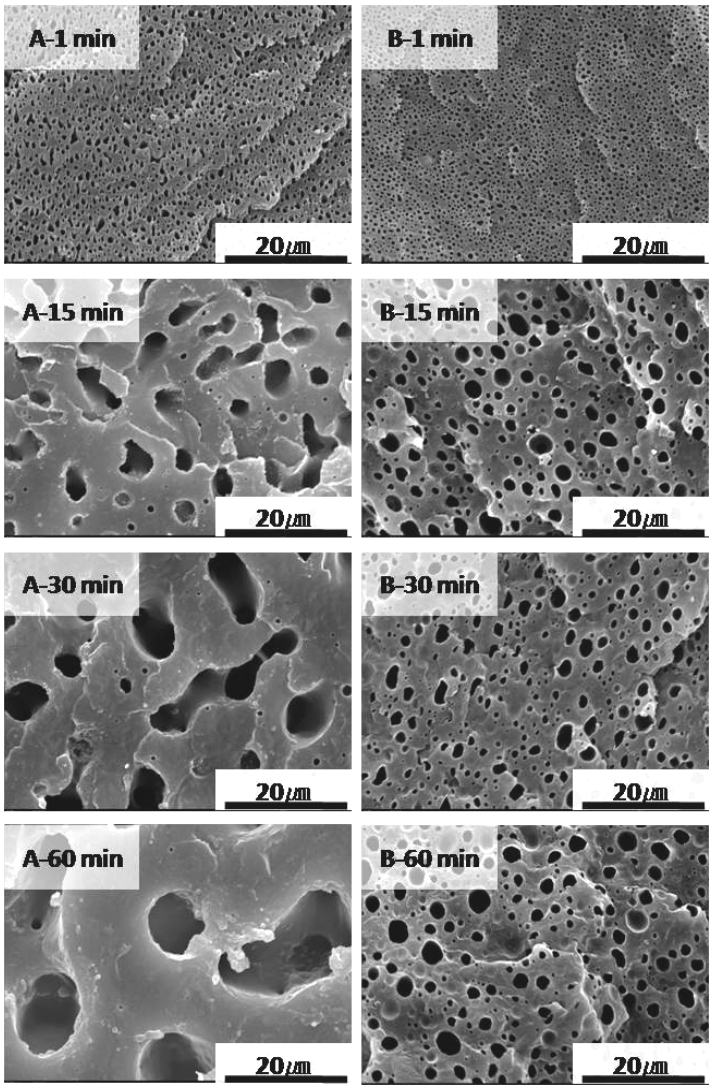

Figure 3.5 SEM micrographs for the annealed PP/PP-g-MA/EOC 60/40 blends (EOC extracted) without (A) and with 5 phr silica (B). The label on the micrographs denomination is respectively 1, 15, 30, and 60 min annealing time at 180°C.

As shown in Figure 3.5, showing SEM images taken after annealing experiments for the 60/40 composition, it is obvious that the coalescence of EOC droplets, which is very severe in the case

of the unfilled blend (Figure 3.5 (a)), is slowed down substantially in the presence of the filler (Figure 3.5 (b)).

To further investigate the effect of shearing on the microstructure of the blends and composites, the evolution of the morphology of the blends in simple shear flow was assessed, according to the procedures of Martin et al. [111] and Maani et al. [112].

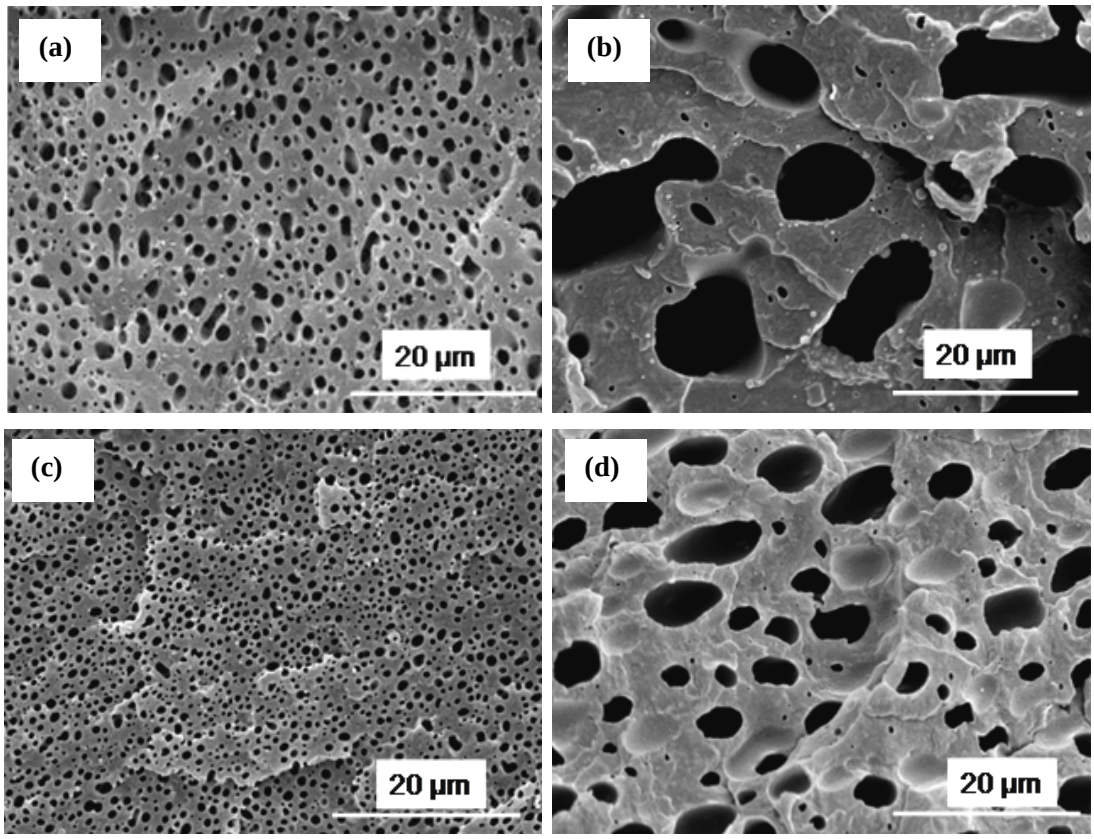

Figure 3.6 SEM images of PP/PP-g-MA/EOC 60/40 blends before (a), (c) and after creep (b), (d). (a) and (b) represent the unfilled sample and (c) and (d) the composite containing 5 phr SiO_2. The total deformation is 9.4 strain units for all the samples. The corresponding time was 1200 s for the unfilled blends and 3200 s for the filled blends.

As seen in Figure 3.6 (a) and (b) severe coalescence of the dispersed phase takes place upon shearing of the blend, resulting in very large and irregular domains. On the other hand, the composite has a finer morphology to begin with (Figure 3.6 (c)), but it is clear that the increase in the size of the dispersed phase domains is not as dramatic, implying that, as expected, the nanoparticles contribute to a suppression of the coalescence [111]. A slight deformation in the shape of the EOC domains can be noticed on Figure 3.6 (d), the domains being less spherical and more elliptic in the direction of the deformation.

To further understand the role of the silica particles on the morphology of the blends, TEM observations were carried out and are presented in Figure 3.7. It can be seen on the TEM images that silica nanoparticles localized exclusively in the (PP/PP-g-MA) matrix phase to form a segregated microstructure in Figure 3.7 (a), (b), (c), and an encapsulated microstructure in Figure 3.7 (d).

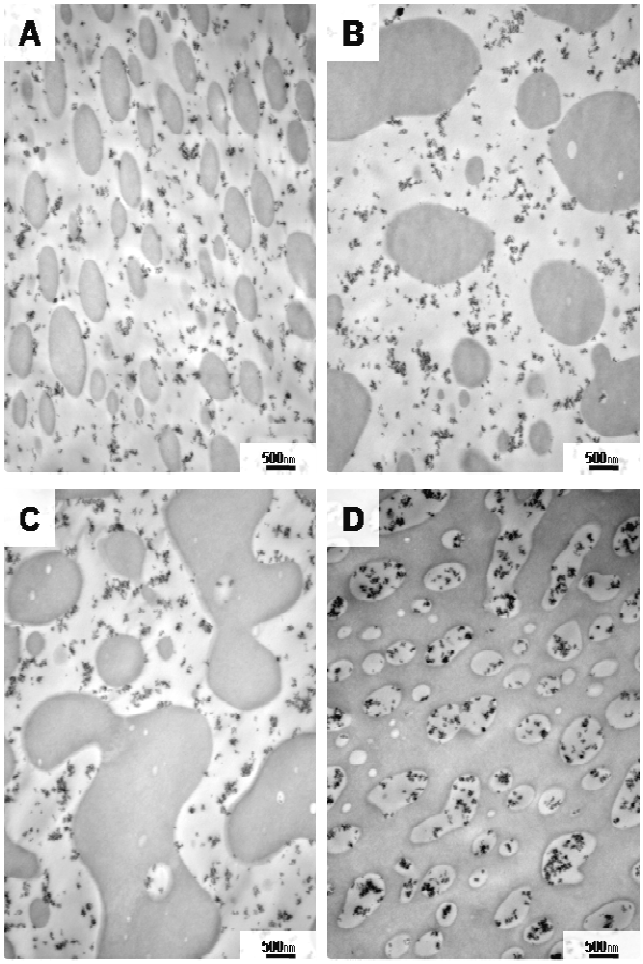

Figure 3.7 TEM micrographs of PP/PP-g-MA/EOC/oct-SiO_2 composites as a function of PP/EOC blend ratio. (A) 70/30; (B) 60/40; (C) 50/50; (D) 30/70. Scale bars represent 500 nm. The stained elastomer phase appears darker.

It is believed that this partitioning, which is based on the thermodynamic principles explained in Chapter 2, is responsible for the favourable mechanical properties of these blends, which are presented in the next section. Further analysis on the thermodynamic partitioning can be found in Chapter 4.

3.3.4 Mechanical properties

The results of the flexural tests are presented in Figure 3.8. First of all, the addition of the compatibilizer had a slight effect on the flexural strength (Figure 3.8 (a)) and flexural modulus values (Figure 3.8 (b)). In the absence of compatibilizer, the addition of silica nanoparticles led to a moderate increase of both flexural modulus and strength at almost all the compositions. However, the best results were obtained when the addition of the silica particles were combined with the addition of the compatibilizer. The improvements of the flexural properties were significant over the entire range of compositions. Moreover, this combination was even more beneficial at high EOC concentrations, such as 50/50. At high EOC concentrations, these results are due to the change in the morphology and the shift in phase inversion composition, resulting in a change from co-continuous morphology to droplet/matrix morphology. However, at low EOC concentrations, the reduction of the domain size as seen on Figure 3.4 is believed to be the key-factor influencing both flexural and tensile properties.

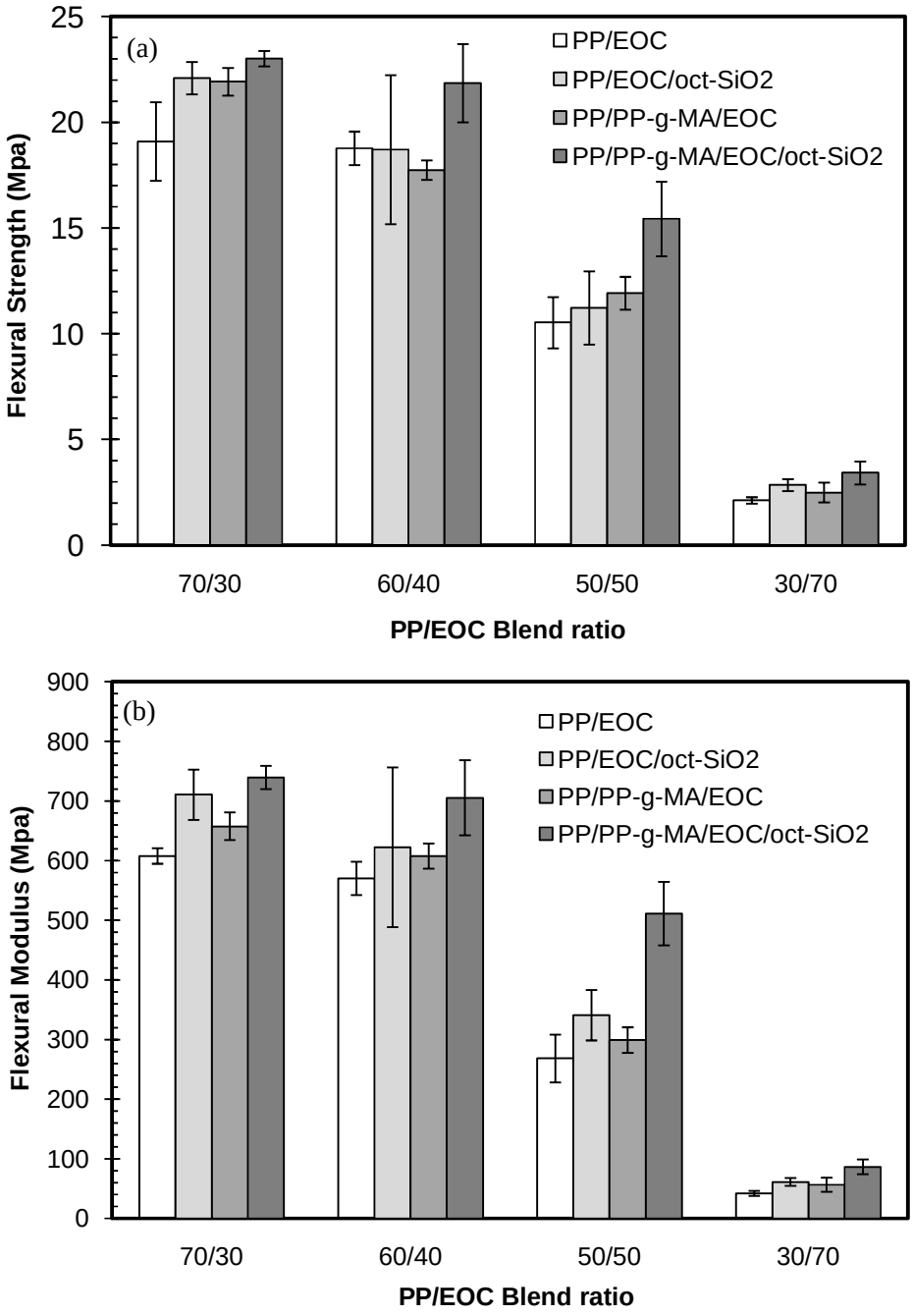

Figure 3.8 (a) Flexural strength and (b) flexural modulus of TPO/nanosilica composites as a function of PP/EOC blend ratio. Error bars represent the standard deviation at a 95% confidence interval.

The positive impact of the combination of silica particles and compatibilizer is also noted in the tensile properties of the compatibilized materials, reported in Table 3.1.

Table 3.1 Tensile properties of compatibilized blends at different PP/EOC blend ratios

Composition			Yield Stress (MPa)	Tensile stress (MPa)	Elongation at Break (%)	Young's Modulus (MPa)
PP/EOC	oct-SiO_2 (phr)	PP-g-MA (phr)				
70/30	-	10	15.8±0.1	30.6±0.8	1838±70	204.2±2.1
70/30	5	10	18.2±0.3	39.7±1.9	2414±90	222.0±8.0
60/40	-	10	11.9±0.5	30.9±1.8	2226±140	141.3±3.8
60/40	5	10	14.5±0.4	35.6±2.5	2448±110	182.7±7.3
50/50	-	10	No yield	29.2±0.8	2315±14	101.3±3.6
50/50	5	10	11.0±0.4	34.8±1.2	2630±48	125.0±5.6

The tensile properties confirm that nanoparticles improve significantly the strength and stiffness of the blends over the entire range of compositions. The appearance of a yield stress in the 50/50 composition is consistent with the change to a droplet-matrix morphology, with a more rigid continuous phase.

Even more interestingly, the elongation at break was not affected by the presence of the particles; it even increased slightly in all compositions, proving that the particles were finely dispersed, especially in the blends with low EOC concentrations as shown on the TEM images of Figure 3.7. Consistently with the preservation of ductility noted from the tensile experiments, the addition of silica particles and compatibilizer did not compromise the impact properties, as shown in Figure 3.9.

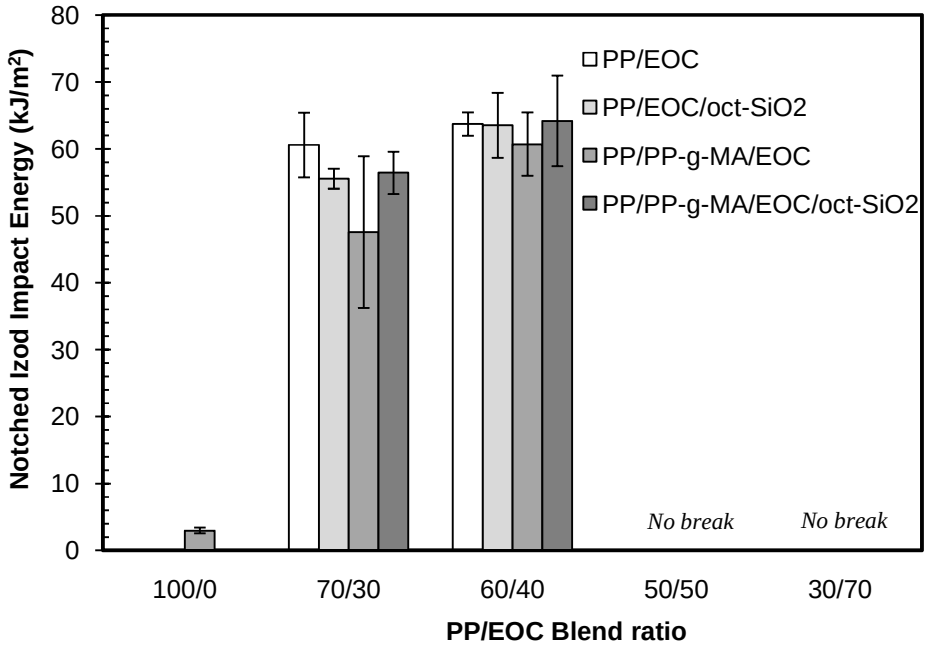

Figure 3.9 Effect of silica on notched Izod impact strength of composites as a function of PP/EOC blend ratio. Error bars represent the standard deviation at a 95% confidence interval.

We attribute this good balance between stiffness and impact properties to the fact that the matrix is reinforced selectively, while leaving the toughening ability of the elastomeric phase intact. The

slight reduction in the particle size of the dispersed EOC phase in the presence of the silica, may also act favorably toward improving toughness [19,21,113].

3.4 Discussion

According to the TEM images shown in Figure 3.6, the nanoparticles were located within the (PP/PP-g-MA) phase to form a segregated morphology when compounded in a twin-screw extruder, consistent with previous reports by Liu and Kontopoulou who obtained similar morphologies using a batch mixer [71,72]. In this work we have shown that the nanoparticles partition always in the PP phase, irrespective of the PP/EOC ratio.

In addition to their localization, the nanoparticles were also finely dispersed thanks to the presence of the compatibilizer and the surface treatment consisting of grafting alkyl chains on their surfaces. The alkyl groups offered a greater affinity with the non-polar chains of the PP matrix and tended to break-up the F/F interactions. As a result of the segregated morphology and the good interfacial adhesion, the composites showed higher strength and stiffness in tensile and flexural modes, while maintaining good impact properties and ductility. At compositions where PP is the matrix, this enhanced mechanical performance is attributed to the selective reinforcement of the matrix leading to higher strength and stiffness, while keeping the EOC phase unfilled and capable to toughen the blends. Furthermore, the shift in phase inversion composition that was observed in the compatibilized samples at compositions above 50/50 PP/EOC resulted in a higher modulus, and the appearance of a yield stress, given that PP was still the matrix.

In addition to modifying the properties of the composites, in the presence of the nanoparticles the characteristics of the dispersed phase were also altered. Theories to explain the reduction of the size of the dispersed phase in the presence of nanoparticles vary, depending on whether the filler

is located in the continuous phase, in the dispersed phase, or at the interphase between the two blend components. Compatibilizing effects due to polymer adsorption on the filler surface, as well as reduction in the interfacial tension between the two phases in the presence of the filler are the generally accepted mechanisms when the filler is located at the interface [69,81,85]. However these mechanisms are obviously not dominant when the filler resides in the matrix, generating a segregated morphology.

In segregated morphologies, different mechanisms underlying the reduction of the size of the dispersed phase domains may be present, including altered viscosity ratio affecting the balance between droplet break-up and coalescence and improved stress transfer to the dispersed phase during compounding, facilitating breakup. The first of these mechanisms is unlikely, because it has been shown that the viscosity is not altered significantly in the presence of nanoparticles at these concentrations [71,106]. The second mechanism may be present as a result of droplets forced to follow a tortuous path corresponding to the conditions of highly confined flow, facilitating droplet break-up, but it is very hard to prove such an assertion experimentally.

Another possibility is that the nanoparticles, together with the layer of bound polymer attached to them, act as physical barriers, preventing droplet coalescence. As clearly shown in Figure 3.8 and Figure 3.9 the EOC domains have a strong tendency toward coalescence, upon further shearing or annealing, similar to the behaviour exhibited by many immiscible blends [112]. However the rate of coalescence is significantly reduced in the presence of nanoparticles. These findings prove for the first time the ability of nanoparticles that are well-dispersed inside the matrix to inhibit coalescence due to a barrier effect, therefore providing a conclusive answer to this widely reported phenomenon.

3.5 Conclusions

The morphology and mechanical properties of PP/EOC blends containing a maleated PP-g-MA compatibilizer and silica nanoparticles were investigated throughout the entire composition range of the blend. Microscopy revealed that in the compatibilized composites the silica nanoparticles localized exclusively in the (PP/PP-g-MA) phase and were finely dispersed resulting in a segregated microstructure. Additionally, the nanoparticles strongly impacted the morphology of the blends over the entire range of blend ratios: at low EOC contents the size of the EOC domains was significantly reduced, and at ratios close to phase inversion, higher EOC concentrations were necessary to obtain a co-continuous morphology. The presence of silica nanoparticles in the compatibilized composites improved significantly the morphological stability of the samples subjected to annealing and steady-shear flow. Coalescence of the EOC domains and coarsening of the microstructure were significantly reduced by the presence of nanoparticles. When the combination of compatibilizer and silica particles was used, the composites exhibited enhanced strength and stiffness in both flexural and tensile tests, whereas impact strength was maintained. This was attributed to the selective localization of the fillers, reinforcing the PP phase without compromising the ability of the EOC domains to act as impact modifiers.

Chapter 4

PREPARATION AND CHARACTERIZATION OF THERMOPLASTIC OLEFIN / NANOSILICA COMPOSITES USING A SILANE-GRAFTED POLYPROPYLENE MATRIX*

4.1 Introduction

Due to the non-polar character of PP, functionalization and/or treatment of the nanoparticles are needed to achieve a good dispersion of the rigid nanoparticles and satisfactory mechanical properties. In the case of silica fillers, this has been achieved via different routes, such as functionalization of the PP matrix with maleic anhydride [114] or silanes [13,51,115], addition of a compatibilizer [14,71,116], or chemical treatment of the nanoparticles [15]. The latter may be accomplished through grafting macromolecules directly onto the nanoparticles [48,117] or by using coupling or coating agents [16,33,40-42,44,61,118].

In the previous chapter it was shown that benefits can be obtained when the filler is selectively localized within the PP matrix. A maleated PP compatibilizer was used to ensure good dispersion and enhance the interfacial properties of the nanosilica and the matrix. In this chapter an alternative functionalization method for PP is followed, through peroxide-initiated grafting of vinyltriethoxysilane, to obtain a PP-g-VTEOS derivative. The alkoxysilane functionality can engage the hydroxyl groups on the surface of silica to provide covalent bonds between the polymer and the filler, resulting in improved compatibility between the matrix and the filler. The

* A version of this Chapter has been published. Bailly M., Kontopoulou M. Polymer 2009(50); 2472-80

morphology as well as the mechanical, thermal and rheological properties of the nanocomposites are presented with a particular focus on the P/F interactions.

4.2 Experimental

4.2.1 Materials

Polypropylene, Escorene PP1042, MFR 1.9 g/10 min at 230°C, was supplied by ExxonMobil Chemical. Ethylene-octene copolymer (EOC) polyolefin elastomer, Engage 8130, MFR 13g/10 min at 190°C, from Dow Chemical was used as an impact modifier. Vinyltriethoxysilane (VTEOS, 97%, Aldrich Chemical Company Inc.) and dicumyl peroxide (DCP, 98%, Sigma Aldrich) were used as received. Irganox 225 antioxidant was obtained from Ciba-Geigy.

4.2.2 Characterization of nanofillers

Three different types of silica, supplied by Evonik Industries (formerly Degussa Corp.) were used. A hydrophilic fumed silica Aerosil® 200 (SiO_2) with an average particle size of 12 nm and a SSA of 200±25 m^2/g, and two hydrophobic surface modified nanosilicas: Aerosil® R805 modified with octylsilane (oct-SiO_2) having a SSA of 150±25 m^2/g and Aerosil® R816 modified with hexadecylsilane (hex-SiO_2) having a SSA of 190±20 m^2/g.

The relative degree of modification with silanes was examined by thermogravimetric analysis (TGA) and FTIR. TGA was performed using a TA Instruments Q500 series thermogravimetric analyzer. Samples were heated from room temperature to 900°C at a rate of 10°C/min under nitrogen atmosphere. Oct-SiO_2 exhibited the highest amount of weight loss; 7 wt% compared to SiO_2 and hex-SiO_2 which showed a weight loss of 1.5 and 2.3-wt% respectively.

From the FTIR spectra the area of the peak corresponding to the –OH groups in the 2700cm^{-1}-3800cm^{-1} range was compared relative to the area of a reference peak at 1650 cm^{-1}. It was found that oct-SiO_2 is more heavily modified than hex-SiO_2 since the area under its peak is lower, indicating that more hydroxyl groups have been substituted by silane groups.

4.2.3 Grafting procedure and nanocomposite preparation

PP powder (40 g) was tumble-mixed with a solution of DCP (0.1 wt%) in VTEOS (5 wt%) for 20 min. The grafting reaction was carried out in a Haake PolyLab rheometer equipped with a Rheomix 610p mixing chamber and roller rotors. The rotation speed, temperature and residence time were fixed at 60 rpm, 190°C and 8 min respectively. 0.2 wt% of antioxidant was added after 3 minutes of mixing time. The grafting reaction of VTEOS onto PP, giving PP-g-VTEOS, has been described in detail in reference [119]. Following the formation of PP-g-VTEOS, various amounts of nanosilica, ranging from 2 to 7 wt% were added and mixed for 2 minutes, followed by the introduction of 20 wt% EOC, which was compounded for 3 minutes.

In order to obtain a non-functionalized PP sample suitable for comparison with the VTEOS grafted material, PP was reacted with 0.1 wt% DCP for 3 minutes to obtain a degraded derivative (deg-PP). Subsequently 0.2 wt% of antioxidant was added; the total mixing time was 8 minutes. This procedure provided a sample with comparable rheological properties, as well as similar heat history as the PP-g-VTEOS.

4.2.4 Characterization of functionalized PP

PP-g-VTEOS samples for graft content analysis were purified from residual VTEOS by dissolving in hot refluxing xylene, precipitating from acetone, and drying under vacuum at 60°C.

FT-IR spectra were obtained using a Nicolet Avatar 360 FTIR ESP instrument. Grafted VTEOS contents were calculated from FT-IR integrations of the 1064-1094 cm^{-1} absorbance of the silane relative to a 422-496 cm^{-1} internal standard region originating from PP. A calibration curve for the determination of the graft content was obtained by using known mixtures of PP and an unreactive silane (ethyltriethoxysilane) as standards. Based on this calculation the grafted VTEOS content was determined to be 0.45wt%.

4.2.5 Microscopy

The state of dispersion of the filler was assessed by TEM imaging, using an FEI Tecnai 20 instrument. Ultra-thin sections were cryomicrotomed using a Leica ultra microtome and stained in RuO_4 vapour to enhance the phase contrast between the PP and elastomer phases.

Samples were prepared for SEM observations by compression moulding using a Carver press at 190°C, and 10 MPa for 1 minute, then freeze-fractured in liquid nitrogen. The elastomer phase was etched in toluene for 2 hours at 80°C. The etched surfaces were observed on a JEOL JSM-840 scanning electron microscope. The SEM images were analyzed by using the Sigma Scan Pro image analysis software to estimate the average diameters of the dispersed elastomer phase. Between 200 and 800 particles were analyzed per sample. The diameter of each particle (D) was calculated using its area determined by the image analysis software. The number (D_n) and volume (D_v) diameters were calculated with the following formulae:

$$D = \sqrt{\frac{4Area}{\pi}}, \qquad \mathrm{D_n} = \frac{\sum n_i D_i}{\sum n_i}, \qquad \mathrm{D_\upsilon} = \frac{\sum n_i D_i^4}{\sum n_i D_i^3} \tag{4.1}$$

n_i being the number of particles having a diameter of D_i.

Finally, the polydispersity index was calculated as:

$$PI = \frac{D_v}{D_n} \tag{4.2}$$

4.2.6 Mechanical properties

Tensile properties were measured using an Instron 3369 universal tester, at crosshead speeds of 10 mm/min. Dog-bone shaped specimens were cut with a Type V die according to ASTM D638 from 1.5 mm thick sheets, which were prepared by compression molding of the compounded samples at approximately 200ºC using a Carver press.

Flexural tests were performed according to ASTM D790, procedure B, at a speed of 13.65 mm/min. Rectangular bars of dimensions 127x12.7x3.2 mm were produced by compression molding at 200ºC. Notched Izod impact tests were carried out on an Instron BLI impact tester at room temperature according to ASTM D 256. Specimens of dimensions 64x12.7x3.2 mm were prepared by compression molding at 200ºC. At least 5 specimens were tested for each sample and the average value is reported.

4.2.7 Thermal properties

The melting and crystallization temperatures (T_m and T_c respectively), as well as heats of fusion and crystallization of the samples were measured on a TA Q100 Differential Scanning Calorimeter (DSC). The samples were first heated to 200ºC for 5 min to eliminate their thermal history and subsequently cooled to -40ºC at a rate of 5ºC/ min. The second endotherm was recorded by heating at 5°C/min. The heat of crystallization was calculated relevant to that of pure crystalline PP (191.4 J/g according to [120]).

4.2.8 Rheological characterization

Rheological characterization was carried out on a Reologica ViscoTech oscillatory rheometer using 20 mm parallel plate fixtures, with a gap of 1 mm at 200 ºC, under nitrogen blanket. The rheometer was operated in the dynamic oscillatory mode in the linear viscoelasticity region –i.e. with strain under 10%, which was determined by stress sweep experiments. The elastic modulus (G'), loss modulus (G") and complex viscosity (η*) were measured as functions of the angular frequency (ω).

4.3 Results

4.3.1 Effect of VTEOS grafting on rheological properties

The chemical treatment of PP with peroxides unavoidably results in degradation via chain scission, lowering substantially the viscosity of the material. This is clearly seen in Figure 4.1, which shows the complex viscosity of PP prior and after chemical modification. On the other hand, the presence of VTEOS grafts does not have a significant effect on the rheology of the materials, as seen through the comparison of the deg-PP and PP-g-VTEOS. Based on the viscosities of both PP-g-VTEOS and deg-PP used in the TPO compounds, a suitable EOC grade with a comparable viscosity was chosen, to provide an optimal viscosity ratio at shear rates between 20-100 s^{-1}, which are relevant to compounding with the batch mixer.

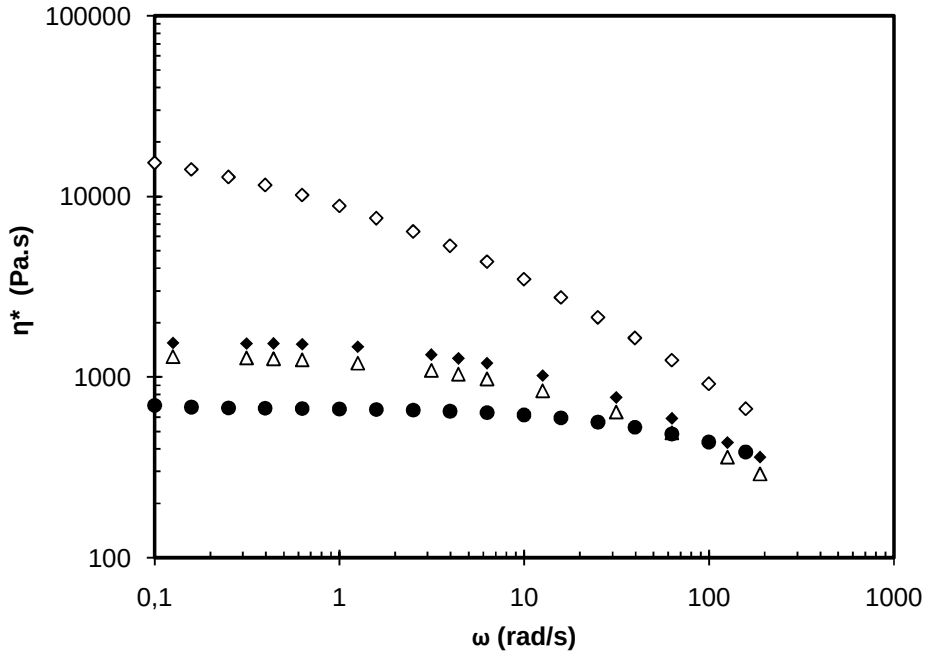

Figure 4.1 Complex viscosity as a function of frequency, obtained by dynamic oscillatory experiments at 200°C. Symbols are (◇) PP; (△) PP-g-VTEOS; (●) EOC; (◆) deg-PP.

4.3.2 Morphology

As reviewed in Chapter 2, the properties of ternary nanocomposites are largely determined by the localization and the state of dispersion of the inorganic fillers, as well as the size and the distribution of the dispersed polymer phase. It has been demonstrated that better mechanical properties are achieved when the inorganic fillers are localized within the matrix [71,72]. In this work, adding the silica prior to the addition of the elastomeric phase resulted in a separated microstructure, where the silica nanoparticles remain exclusively in the PP matrix, irrespective of filler treatment (Figure 4.2).

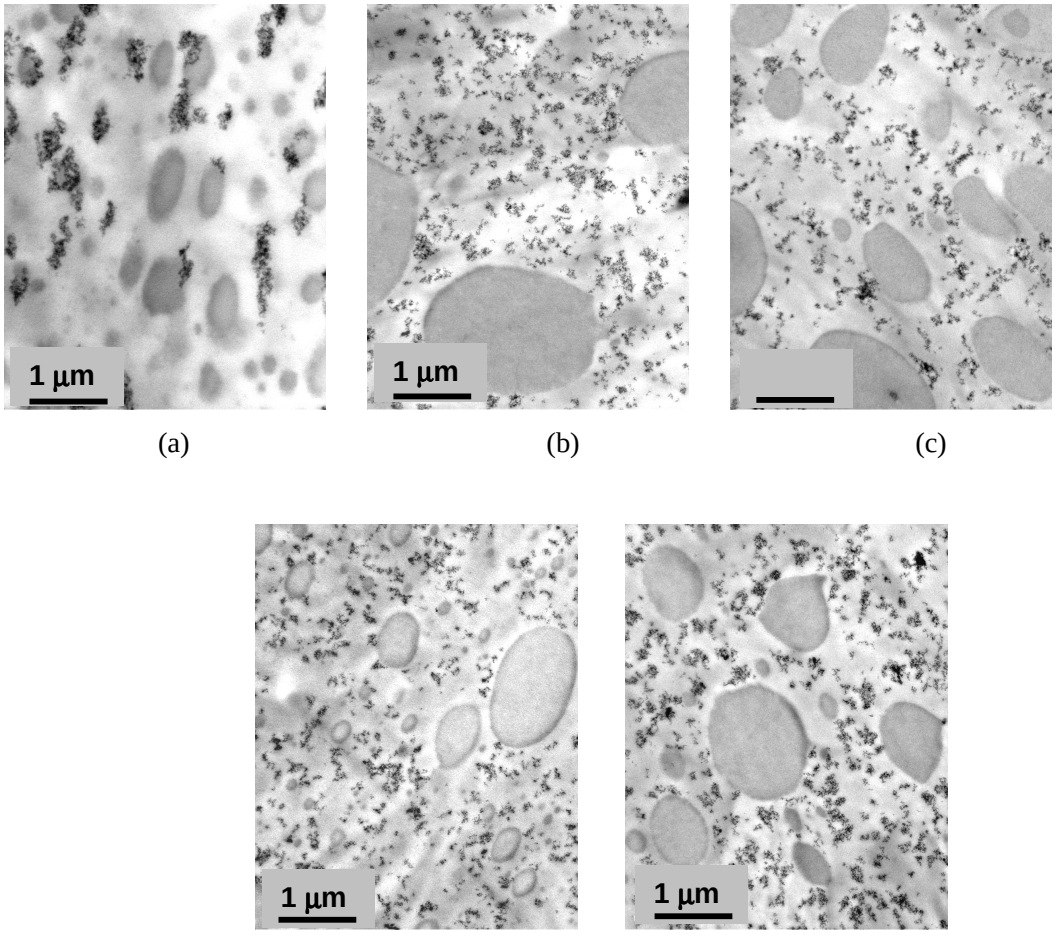

(a) (b) (c)

(d) (e)

Figure 4.2 TEM images of (a) deg-PP/EOC/SiO_2; (b) PP-g-VTEOS/EOC/SiO_2; (c) PP-g-VTEOS/EOC/oct-SiO_2; (d) deg-PP/EOC/oct-SiO_2; and (e) PP-g-VTEOS/EOC/hex-SiO_2. Silica content is 5wt%. The darker domains correspond to the EOC dispersed phase.

The state of dispersion of the filler depends on the silica treatment and the presence of matrix functionality: it is well-known that the silanol groups present at the surface of the silica nanoparticles tend to form hydrogen bonds, resulting in a strong tendency toward agglomeration during melt compounding. This is evident in the deg-PP/EOC/SiO_2 composites containing untreated SiO_2 and a non functionalized matrix (Figure 4.2 (a)). Given the large size of the

aggregates (about 1μm), these can rather be characterized as “microcomposites”. Introduction of the alkoxysilane functionality results in the establishment of covalent bonding between the polymer and the filler, by engaging the hydroxyl groups on the surface of the silica, according to Scheme 4.1.

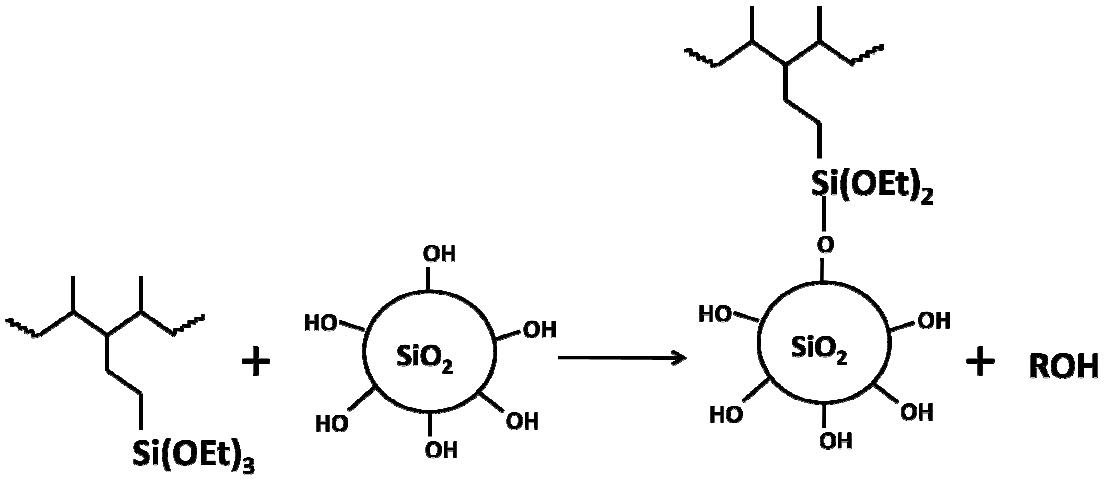

Scheme 4.1 Schematic illustration of the hydrolysis reaction between the silanol groups located at the surface of the silica with the VTEOS grafts.

This improves the stress transfer to the filler during melt compounding, resulting in more efficient breakup of the filler aggregates, as evidenced in the PP-g-VTEOS/EOC/SiO_2 composites of Figure 4.2 (b). Furthermore, replacing silanol groups located at the surface of the nanoparticles by silane groups consisting of long alkyl chains will tend to reduce the size of the aggregates, by breaking up the hydrogen bonds between the particles, therefore improving the dispersion of the fillers, as seen on the TEM images of PP-g-VTEOS/EOC reinforced with oct-SiO_2 and hex-SiO_2 (Figure 4.2 (c-e)). Additionally, the surface treatment of the nanoparticles renders the nanoparticles more hydrophobic owing to the presence of the long alkyl chains in the grafted

silane groups, therefore reducing their polar nature. This further contributed to the improved dispersion of oct-SiO_2. Surface treatment of the nanoparticles provided a very efficient means for their good dispersion, irrespective of the presence of functionality in the matrix, as shown by the relatively good dispersion of oct-SiO_2 in the non functionalized deg-PP matrix (Figure 4.2 (d)).

Hex-SiO_2 contains longer alkyl chains, which would result in a reduced tendency of the filler to agglomerate, because of steric hindrance [45]. However, comparison of the two silane modified silicas by TGA and FT-IR spectroscopy showed that oct-SiO_2 particles are more heavily modified than hex-SiO_2 particles. This is probably the reason why oct-SiO_2 composites exhibit improved dispersion (Figure 4.2 (c) vs. (e)), although additional research is needed to differentiate between these factors.

In addition to the differences in filler dispersion, SEM observations showed variabilities in the size of the dispersed elastomer phase.

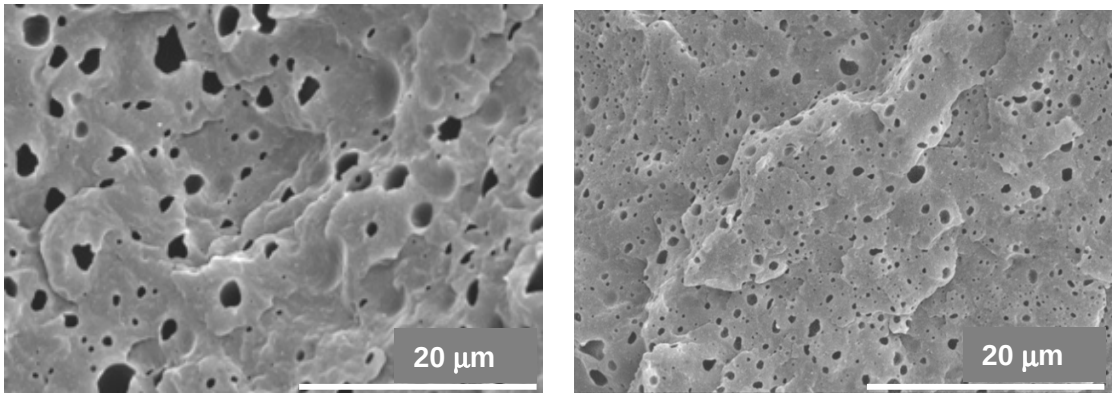

(a) (b)

Figure 4.3 SEM micrographs of (a) PP-g-VTEOS/EOC; (b) PP-g-VTEOS/EOC/oct-SiO_2 7 wt%. The holes correspond to the etched dispersed phase.

In Figure 4.3, which shows the SEM images of the PP-g-VTEOS/EOC and PP-g-VTEOS/EOC/ 7wt% oct-SiO_2, it can be seen that in the presence of the filler the size of the dispersed phase becomes significantly finer.

The results of the image analysis performed on the SEM images of PP-g-VTEOS/EOC blends containing up to 7wt% of oct-SiO_2 are presented in Figure 4.4 and confirm a shift in size in favour of finer particles, at the highest nanosilica content.

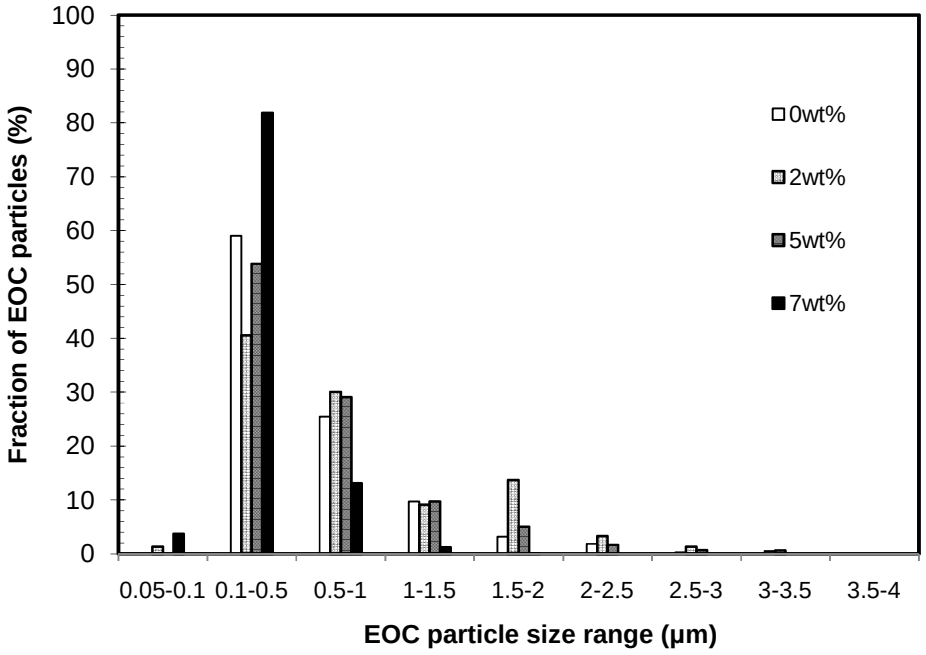

Figure 4.4 EOC particle size distribution in PP-g-VTEOS/EOC /oct-SiO_2 composites at different silica contents. Data based on the number of particles per image with approximately 800 particles per image.

The number and volume average particle diameters for all the composites are summarized in Table 4.1.

Table 4.1 Particle sizes for composites containing various amounts and types of nanosilica, obtained through image analysis of SEM images.

Sample	D_n(μm)	D_v (μm)	Polydispersity Index
PP-g-VTEOS/EOC	0.58	2.25	3.68
PP-g-VTEOS/EOC/oct-SiO_2 2wt%	0.81	2.04	2.45
PP-g-VTEOS/EOC/oct-SiO_2 5wt%	0.64	2.42	3.71
PP-g-VTEOS/EOC/oct-SiO_2 7wt%	0.30	0.82	2.27
PP-g-VTEOS/EOC/SiO_2 5wt%	0.91	2.93	3.06
PP-g-VTEOS/EOC/hex-SiO_2 5wt%	0.64	2.98	4.22
Deg-PP/EOC/oct-SiO_2 5wt%	0.60	2.97	4.46
Deg-PP/EOC/SiO_2 5wt%	0.44	2.09	1.93

These findings are in agreement with the findings of Chapter 3, in which we reported that in the presence of well-dispersed silica particles in the matrix, coalescence was inhibited, leading to a reduction of the size of the dispersed domains.

4.3.3 Rheological characterization

As shown from the oscillatory shear results in Figure 4.5 and Figure 4.6 the composites exhibit a loss of the Newtonian plateau and higher values of the complex viscosity and moduli as the filler content increases above 2 wt%. The disappearance of the terminal flow region and appearance of a yield stress become more pronounced at higher filler loadings (Figure 4.5).

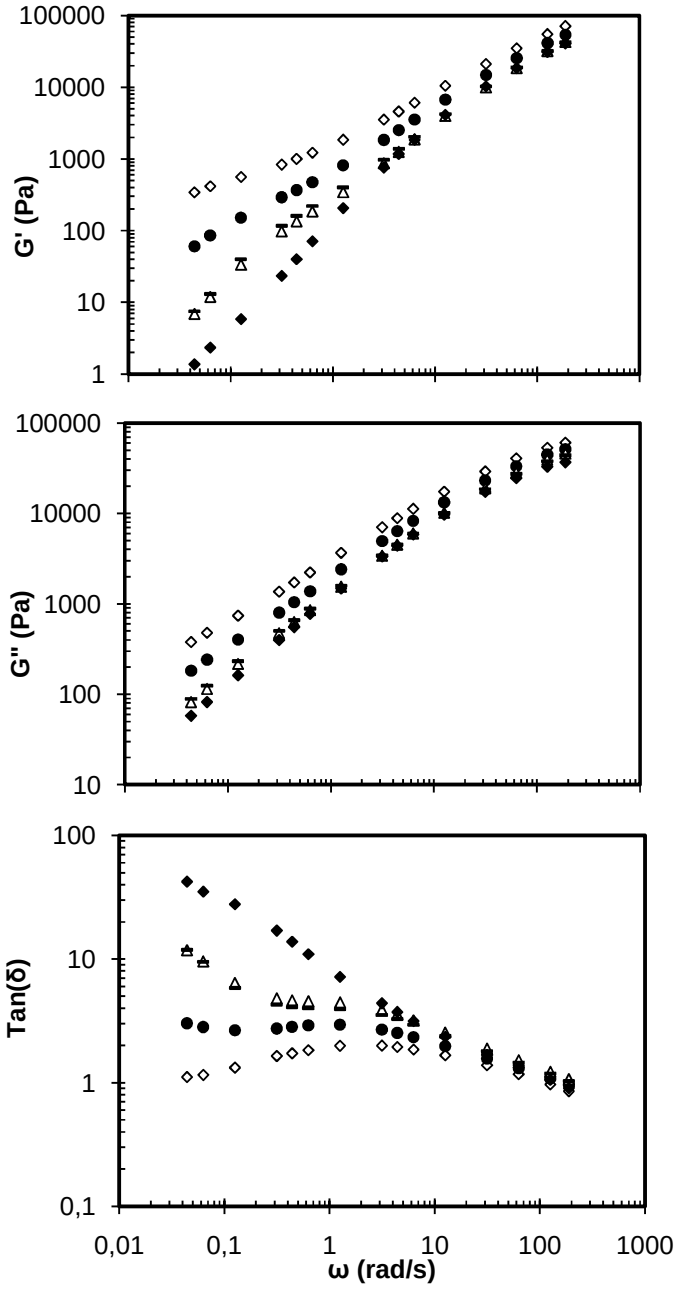

Figure 4.5 (a) Complex viscosity (η*), (b) elastic modulus (G′), and (c) tanδ of the nanocomposites as a function of frequency at 200°C. Symbols are (◆) PP-g-VTEOS; (-) PP-g-VTEOS/EOC; (△) PP-g-VTEOS/EOC/oct-SiO_2 2wt%; (●) PP-g-VTEOS/EOC/oct-SiO_2 5wt%; (◇) PP-g-VTEOS/EOC/oct-SiO_2 7wt%.

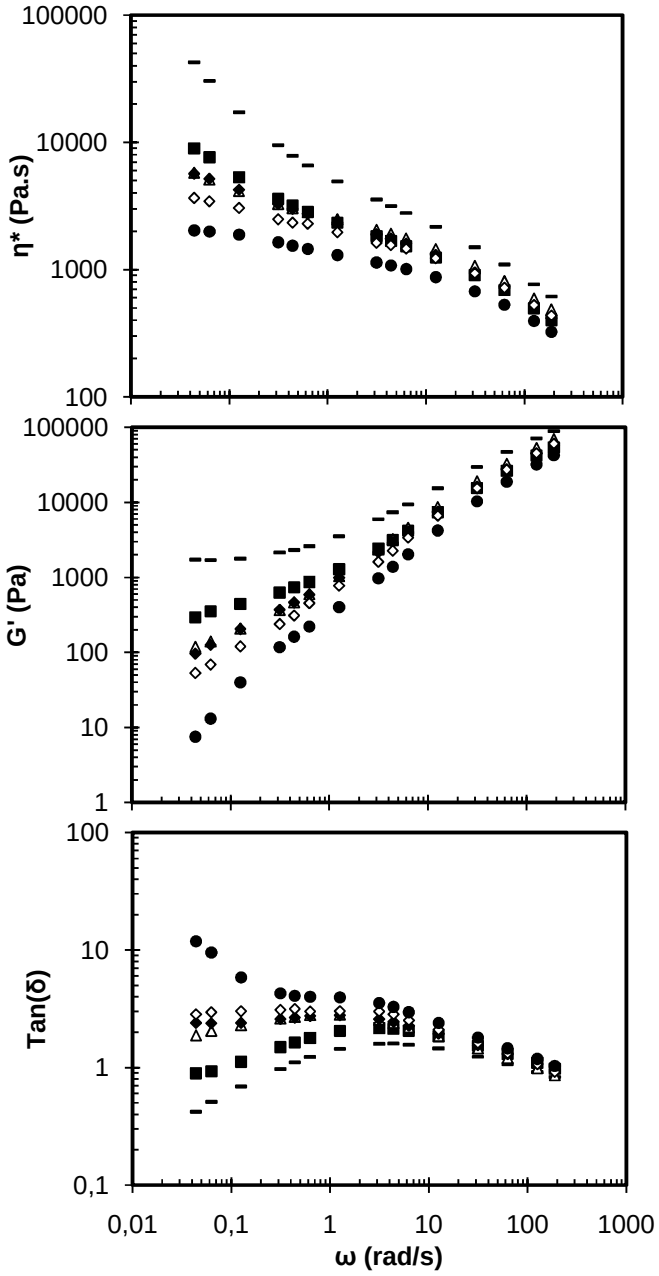

Figure 4.6 Complex viscosity (η*), elastic modulus (G'), and tanδ of the composites as functions of frequency at 200°C. Symbols are (●) PP-g-VTEOS/EOC; (◇) PP-g-VTEOS/EOC/SiO_2; (◆) deg-PP/EOC/oct-SiO_2; (△) PP-g-VTEOS/EOC/hex-SiO_2; (■) PP-g-VTEOS/EOC/oct-SiO_2; (-) deg-PP/EOC/SiO_2. Silica content is 5wt%.

The appearance of yielding at 7 wt% is consistent with the existence of a “percolation” threshold. This behaviour has been attributed to the formation of a “polymer-filler” network [65]. These trends are better reflected by the loss tangent versus frequency data, as shown in Figure 4.5 (c). First of all the secondary relaxation, attributable to the presence of a dispersed deformable phase [121] can be clearly seen in the curves corresponding to the PP-g-VTEOS/EOC blend; addition of just 2wt% oct-SiO_2 does not appear to affect this response. Both samples tend to reach terminal flow eventually. Significant deviations from the terminal flow are noted however as the oct-SiO_2 content increases further, with the highest content approaching what seems like a “secondary” plateau.

Whereas the rheological response is dependent on silica content, silica treatment and matrix functionalization also play a significant role, as shown in Figure 4.6.

These results show two distinctly different trends. On the one hand, the presence of large aggregates, evident in the deg-PP/EOC/SiO_2 composites (see also Figure 4.2 (a)) results in a substantial increase in viscosity and elasticity over the entire frequency range. Such behaviour is typical of macrocomposites in which F/F interactions due to the presence of hydrogen bonding are predominant [33,65]. Addition of the alkoxysilane functionality introduced covalent bonding and improved the dispersion of the filler considerably, resulting in a nanocomposite as shown in Figure 4.2 (b). The complex viscosity and elasticity appear substantially lower compared to deg-PP/EOC/SiO_2; still there is a significant increase compared to the base material. The extent of modification of the silica particles further seems to influence the low frequency properties. At this point the origin of this phenomenon is not clear; this will be the subject of investigation in Chapter 5.

4.3.4 Thermal properties

The results of the thermal characterization of the composites by DSC are shown in Table 4.2. Once again surface treatment and aggregation seem to be of prime importance: The unmodified SiO_2 particles, which have the highest SSA have a pronounced nucleation effect, increasing the crystallization temperature by about 10°C, followed by hex-SiO_2, while the most heavily modified oct-SiO_2, which has the lowest SSA, has the least effect on crystallization temperature. The overall crystallinity of the composites follows a similar trend. It is worth noting that the nucleation effect is absent in the case of the microcomposites deg-PP/EOC/SiO_2, obviously because of the substantially reduced surface area available for nucleation in the presence of large aggregates, hindering their ability to act as efficient nucleating agents.

Table 4.2 Thermal properties of composites containing various amounts and types of nanosilica

Sample	T_m (°C)	ΔH_f (J/g)	T_c (°C)	ΔH_c (J/g)	Crystallinity (%)
PP	164.9	99.2	118.1	98.9	51.4
PP-g-VTEOS	162.7	102.6	119.4	103.5	53.2
PP-g-VTEOS/EOC	161.1	75.0	117.1	75.7	48.6
PP-g-VTEOS/oct-SiO_2 5wt%	163.6	97.3	118.3	98.4	56.8
PP-g-VTEOS/EOC/oct-SiO_2 2wt%	162.1	83.0	120.6	83.0	55.1
PP-g-VTEOS/EOC/oct-SiO_2 5wt%	162.2	76.9	119.7	79.6	52.4
PP-g-VTEOS/EOC/oct-SiO_2 7wt%	163.2	77.1	121.0	78.1	53.5
PP-g-VTEOS/EOC/SiO_2 5wt%	164.1	88.5	128.5	88.7	60.3
PP-g-VTEOS/EOC/hex-SiO_2 5wt%	163.5	80.0	126.9	80.3	54.5
Deg-PP/EOC/oct-SiO_2 5wt%	160.9	81.9	117.6	82.11	55.9
Deg-PP/EOC/SiO_2 5wt%	162.0	85.7	116.6	87.3	58.4

4.3.5 Mechanical properties

As shown in Table 4.3, the addition of EOC decreases the tensile strength and Young's modulus of the PP matrix and enhances the elongation at break and impact strength, resulting in a more ductile material. This is a well-known consequence of elastomer addition [20,88] and confirms the ability of EOC to act as an efficient impact modifier for the PP-g-VTEOS matrix.

Table 4.3 Mechanical properties of composites containing various amounts and types of nanosilica.

Sample	Young's Modulus (MPa)	Tensile Stress (MPa)	Elongation at Break (%)	Flexural Modulus (MPa)	Flexural Stress (MPa)	Impact Strength (J/m)
PP-g-VTEOS	325.8±48	34.32±1.4	1159±336	1090±34.6	37.9±4	22.4±3.3
PP-g-VTEOS/EOC	224.8±13	21.6±1.5	1457±333	573±17	21.9±1.8	39.9±1.5
PP-g-VTEOS/oct-SiO_2 5wt%	371.1±14	35.9±1.6	38±6.6	1181±27	41.6±0.5	20.4±2.2
PP-g-VTEOS/EOC/oct-SiO_2 2wt%	260.2±9.9	23.8±0.6	713±443	821±22	28.9±0.7	43.0±4.2
PP-g-VTEOS/EOC/oct-SiO_2 5wt%	298.4±15	26.5±0.8	536±241	913±11	30.8±0.4	44.5±3.3
PP-g-VTEOS/EOC/oct-SiO_2 7wt%	278.4±12.4	23.9±0.9	78.4±35	925±17	31±1.2	36.6±2.8
PP-g-VTEOS/EOC/SiO_2 5wt%	259.4±35.9	22.4±0.8	119.8±67	842±13.3	28.9±3.1	40.9±3.2
PP-g-VTEOS/EOC/hex-SiO_2 5wt%	268.1±14.8	22.2±0.8	79.5±29	851±39.8	28.7±0.3	42.9±7.3
Deg-PP/EOC/oct-SiO_2 5wt%	240.4±30.4	23.1±2.1	211.9±117	755±35.0	27.0±1.1	42.7±6.2
Deg-PP/EOC/SiO_2 5wt%	268.6±24.8	20.8±2.7	202.3±160	897±50.7	31.3±1.0	35.6±3.7

Significant reinforcement was achieved upon silica addition. The dispersion of the nanoparticles plays a determinant role in the ability of the rigid nanofillers to carry the applied load. A fine dispersion is accompanied by a larger interfacial area and a strong adhesion between the fillers and the matrix; this is the basis of an efficient load transfer, given that the reinforcement upon silica addition occurs as the load applied during mechanical testing is transferred to the rigid nanoparticles. From Table 4.3 it becomes obvious that oct-SiO_2, which has the best dispersion as seen on the TEM images (Figure 4.2), is the most beneficial filler. In its presence, the Young's and flexural moduli are improved by 33% and 61% respectively at a 5wt% oct-SiO_2 content compared to PP-g-VTEOS/EOC, as shown in Figure 4.7.

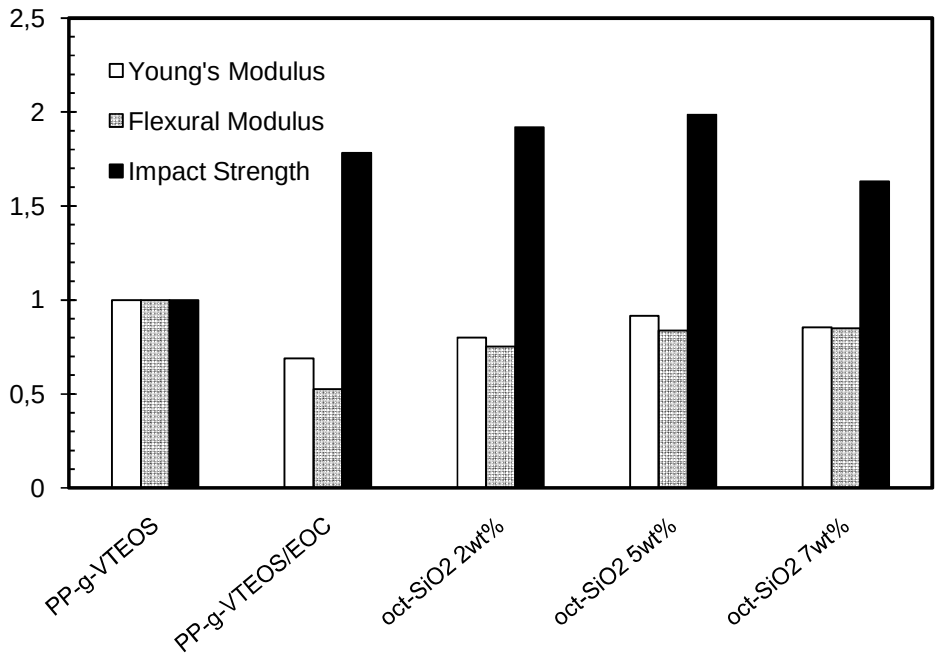

Figure 4.7 Effect of oct-SiO_2 loading on the mechanical properties of PP-g-VTEOS. The bars represent the ratio of the physical property of the composite with respect to the property of the unfilled PP-g-VTEOS.

This increase tends to restore the original moduli that the PP matrix had prior to addition of the elastomer. The maximum values are obtained at a 5wt% silica content in tensile tests and at 7wt% in flexural tests. A smaller degree of reinforcement is observed for SiO_2 and hex-SiO_2 particles, which exist in a more aggregated state.

On the other hand, the increase in modulus is accompanied by an almost complete loss of the elongation at break, with the exception of the oct-SiO_2 containing composites, which maintain some ductility. For this material the most substantial losses in ductility are observed beyond 5wt% oct-SiO_2 content. This can be explained by the presence of a percolation threshold at contents above 5wt%, as evidenced by the rheological characterization (Figure 4.5). Higher silica contents lead to the formation of agglomerates, which act as stress concentrators. Most importantly, the presence of nanosilica does not compromise impact properties – on the contrary a slight improvement is seen upon the addition of nanofillers, and especially oct-SiO_2 (Figure 4.7 and Table 4.3).

It is worth noting that the addition of oct-SiO_2 to PP-g-VTEOS alone results in significant ductility and toughness reduction (see Table 4.3). Therefore the improvement seen in the PP-g-VTEOS/EOC- based composites can be attributed to the selective localization of the filler, which reinforces the PP-g-VTEOS matrix, while leaving the POE phase intact. The ability of EOC to act as an impact modifier for the PP-g-VTEOS matrix remains thus unaffected.

4.4 Discussion

The physical properties of nanocomposites are largely dependent on the P/F and F/F interactions. It is well-established that the reinforcement of the polymer is attributed to the increase in the area of contact between the polymer and the nanofillers, as well as the ability of the polymer and the

matrix to form a strong interface, in order to transfer the applied load from the matrix to the rigid nanofillers.

In this work, the type of interactions between the silica and the PP matrix depends on the degree of treatment of the silica particles and the functionalization of the matrix. The following mechanisms are prevalent: Firstly, the silanol groups present at the surface of the nanoparticles participate in hydrogen bonding, causing the particles to aggregate when compounded with a hydrophobic matrix like PP. This is the main F/F interaction, which causes the formation of micrometer-scale aggregates, the presence of which is unfavourable in terms of mechanical properties. Secondly, the alkoxysilane functionality engages the hydroxyl groups on the surface of the silica in a hydrolysis reaction, according to Scheme 4.1, resulting in covalent bonding. This reaction has been previously reported in alumina and silica particles [16,61], as well as glass fiber composites [58-60] and constitutes the predominant mechanism in the composites containing the PP-g-VTEOS matrix. Our results indicate that presence of covalent bonding alone is not sufficient to obtain optimum properties, as evidenced by the results obtained for the composites containing PP-g-VTEOS and unmodified SiO_2. Rather a combination of good dispersion and presence of covalent bonding is needed. This can be achieved by treatment of the nanoparticles with silanes to replace some of the silanol groups by silane groups, thus rendering the particles more hydrophobic, with improved affinity to the polyolefin matrix and a smaller tendency to agglomerate. It should be noted however that since the replacement of silanol groups is only partial, the hydrolysis reaction is still likely to occur. The extent of the interaction with the silane grafts will thus depend on the amount of the free hydroxyl groups remaining after modification. Moreover, the improved dispersion of particles facilitated by the replacement of OH groups should contribute to a further increase of the surface available for the hydrolysis reaction. The

substantial improvement in mechanical properties observed in the oct-SiO_2 containing composites indicates that for this nanosilica grade the extent of particle modification is balanced, so that F/F interactions can be reduced enough to prevent particle agglomeration, while leaving a sufficient amount of hydroxyl groups available to form covalent bonds.

The benefits of covalent bonding in terms of strengthening the interface between polymer and filler become apparent when comparing the PP-g-VTEOS/EOC/oct-SiO_2 system with its non-functionalized deg-PP/EOC/oct-SiO_2 counterpart. Even though the dispersion of oct-SiO_2, as well as that of the dispersed EOC phase is not substantially different in the two systems (see Figure 4.2 and Table 4.1) implying that the surface modification of the filler is primarily responsible for its good dispersion, the mechanical properties are substantially enhanced in the presence of covalent bonding (Table 4.3), which strengthens the interface between polymer and filler. This is further confirmed by the enhancement in rheological properties, which is more pronounced in the PP-g-VTEOS/EOC/oct-SiO_2 composite (Figure 4.6), compared to the rest of the nanocomposites.

In this work, the focus rests on formulating a strategy for impact toughening, which takes advantage of filler-induced matrix reinforcement, while maintaining the impact toughening properties of the polyolefin elastomer. The deformation mechanisms upon addition of a rubbery phase into a thermoplastic matrix have been widely investigated for decades. Stress concentration around the elastomer particles leads to three different mechanisms: multiple shear yielding occurring at the interface matrix / rubber or in the matrix itself, multiple crazing by the formation of crazes either at the vicinity or inside the rubber particles [17], and finally by cavitation which often induces stress whitening. The latter mechanism has been observed in our previous work on maleated PP/EOC/oct-SiO_2 composites [71].

In order for the EOC to act as an efficient impact modifier via the above mechanisms, its beneficial elastomeric properties must remain unaffected by the filler. Therefore ensuring that the filler remains exclusively inside the matrix is crucial in obtaining optimum properties. A calculation of the thermodynamic partitioning of oct-SiO_2 can be done by first estimating the surface tension between two components, according to the Owens and Wendt equation [122]:

$$\gamma_{AB} = \gamma_A + \gamma_B - 2\sqrt{\gamma_A^d \gamma_B^d} - 2\sqrt{\gamma_A^p \gamma_B^p} \quad (4.3)$$

where A and B correspond to the two polymer phases (PP and EOC respectively); γ is the global surface tension, with γ^p and γ^d respectively being its *polar* and *dispersive* contributions.

The localization of the fillers can then be predicted through the calculation of the wetting coefficient ω:

$$\boldsymbol{\omega} = \frac{\gamma_{SiO_2-B} - \gamma_{SiO_2-A}}{\gamma_{AB}} \quad (4.4)$$

ω<-1 means that the fillers will tend to go into the EOC phase, -1<ω<1 implies that the filler will tend to remain at the interface, and ω>1 indicates that the fillers will tend to go into the PP phase.

Substitution of the surface tension data shown in Table 4.4, results in a wetting parameter of ω=-8.3 for the unmodified silica, indicating that it has a higher affinity toward the dispersed EOC phase.

Table 4.4 Surface tensions of PP, EOC and nanosilica at 190°C.

Material	Surface tension (mJ/m^2)			Reference
	Global	Dispersion	Polar	
PP	21.7	21.2	0.5	[77]
EOC	17.5	15.6	1.9	[77]
SiO_2	47	12.9	34.1	[69]
oct-SiO_2	15.5	15.5	0	[69]

On the contrary a wetting parameter of ω=1.1 is found at a temperature of 190°C, indicating that the oct-SiO_2 particles have a higher affinity toward the PP phase, and will thus tend to migrate into the PP matrix upon melt compounding.

We have confirmed these calculations by compounding simultaneously PP, EOC and silica, followed by TEM observations. The results were similar, when PP-g-VTEOS was used, indicating that matrix functionalization does not influence substantially the localization of the filler. It is possible therefore when using the modified silica to adopt a one-step compounding procedure, where all components are inserted together in the equipment, and still obtain the desirable partitioning of the filler in the PP matrix, thereby ensuring that a good balance of toughness and stiffness is maintained.

4.5 Conclusions

Ternary nanocomposites based on a PP-g-VTEOS matrix were prepared via a melt compounding procedure, which resulted in a separated morphology wherein the silica nanoparticles were dispersed in the polypropylene matrix. Surface treatment of the nanosilica with silanes contributed to the fine dispersion of the filler.

DSC experiments demonstrated the nucleating effect of the non-treated silica particles via an increase of the crystallization temperature and the degree of crystallinity. However, silane-treated particles did not affect significantly the crystallization process.

The tensile and flexural properties of the composites were improved upon addition of the rigid nanofillers, whereas the impact strength was maintained when the nanosilica was treated with octylsilane. These improvements in properties are attributed to a combination of the localization of finely dispersed fillers in the PP matrix and the presence of covalent bonding due to a hydrolysis reaction between the silanol groups present on the surface of the silica and silane grafts in the polymer. It can be concluded that this approach can generate composites having a good balance of stiffness due to the strengthening of the matrix in the presence of nanosilica, and toughness because of the presence of the unfilled dispersed elastomer phase.

Increasing silica concentration significantly changed the rheological behaviour at low frequencies to reach a pseudo-solid like behaviour characterized by a reduced dependency of the complex viscosity and the elastic modulus on the frequency. The responses were influenced by the type of interactions between nanosilica and polymer matrix. This is further investigated in Chapter 5.

Chapter 5

EFFECT OF POLYMER/FILLER INTERACTIONS ON THE STRUCTURE AND RHEOLOGICAL PROPERTIES OF ETHYLENE-OCTENE COPOLYMER/ NANOSILICA COMPOSITES*

5.1 Introduction

Colloidal silica suspensions have been used extensively in applications involving paints, food, as well as in emerging technologies such as photonics and microelectronics, due to their function as thickening and thixotropic agents in low molecular weight solvents [123,124]. Fumed and precipitated silica particles have also successfully served as reinforcing agents for rubbers [125] and more recently for thermoplastic matrices [10].

The unique properties of silica nanoparticles arise from their surface chemistry characterized by the presence of silanol groups. When dispersed in a liquid medium, aggregates of primary particles interact via hydrogen bonding, giving rise to larger flocculated structures called flocs. As the concentration of particles in solution increases, a sol-gel transition is eventually reached, characterized by the formation of a three-dimensional network and the appearance of a gel-like structure. This specific arrangement of particles in a space filling network can be described by a fractal geometry [126,127]. The gelation process depends strongly on several variables, such as the volume fraction of nanoparticles, the type of particles used (hydrophilic versus hydrophobic) and the nature of the suspending medium (polar versus non-polar). As a result, a wide range of materials can be prepared, from low viscosity sols to elastic gels [124].

*A version of this Chapter has been published. Bailly M., Kontopoulou M., El Mabrouk K. Polymer 2010 ;51(23) ;5506-15

The steady-shear rheology of silica-containing suspensions is characterized by pronounced shear thickening and is influenced by the transient disruption and build-up of the filler network [123,128]. Scaling relations obtained through linear and non-linear viscoelasticity measurements [124,129-131] have been associated to the fractal dimensions of the flocculated silica structures, as obtained by image analysis or light-scattering [127,132].

Studies on polymeric matrices have mostly focused on elastomer technology. Using thermodynamic arguments, Wang et al. showed that in filled rubber compounds differences in the surface energy between filler and polymer cause flocculation of the filler aggregates in a manner similar to that observed in colloidal systems [8]. Experimental evidence in elastomers points to the concept of a network structure that refers to a space-filling configuration of kinetically aggregated filler clusters [133]. A structure comprised of rigid filler particles with fractal structure has also been suggested by Huber and Vilgis [134].

The rheological properties of polymer composites are related to the work of adhesion between the filler surface and the polymer matrix [135]. Therefore a lot of attention has been paid on the rheology of composites containing high molecular weight suspending media, being either polymers in the melt state or polymer solutions. Dramatic increases in the storage moduli at low frequencies, leading to the appearance of a secondary plateau or a “solid-like behaviour” and a drop of the storage modulus upon an increasing strain, also known as the “Payne effect” are commonly observed [65]. The scaling relations governing these composites are similar to those reported for suspensions [65].

Although the presence of chemical bonds between the matrix and the fillers is crucial to achieve improved mechanical properties of the resulting composites [15,136,137], the influence of chemical bonds on the rheological properties of the composites is still unclear.

Chapter 4 reported the beneficial effects of grafting a silane functional group to the polyolefin matrix. This chapter aims at investigating further the nature of the interactions between the grafted matrix and the nanosilica. The EOC matrix is functionalized with a reactive and a non-reactive silane, the former of which forms chemical bonds with the surface silanol groups of the nanosilica particles. Detailed rheological characterization and imaging are used to detect the influence of the presence of chemical bonds on the structure of the composites and their rheological response.

5.2 Experimental

5.2.1 Materials

The ethylene-octene copolymer (EOC), trade name Engage 8130, density 0.864 g.cm^{-3}, MFI 13 g/10 min at 190°C, copolymer content 42 wt%, was obtained from Dow Chemical. The melting and crystallization temperatures of this polymer, as measured by DSC are 67.1°C and 40°C respectively, and the degree of crystallinity is 3.7%. Vinyltriethoxysilane (VTEOS, 97%, Aldrich Chemical Company Inc.), vinyltriethylsilane (VTES, 98%, Sigma-Aldrich) and dicumyl peroxide (DCP, 98%, Sigma Aldrich) were used as received.

Two different types of silica with an average particle size of 12 nm were supplied by Evonik Industries (formerly Degussa Corp.): A hydrophilic fumed silica Aerosil® 200 with a specific surface area (SSA) of 200±25 m^2/g, and a hydrophobic surface modified nanosilica Aerosil® R805 modified with octylsilane (oct-SiO_2) having a SSA of 150±25 m^2/g. Detailed characterization of the fillers, including TGA and FT-IR scans can be found in Chapter 4.

5.2.2 Grafting Procedure and Composite Preparation

EOC pellets were premixed with 0.1 wt% of DCP and 2 wt% of VTEOS or VTES in a Haake PolyLab rheometer equipped with a Rheomix 610p mixing chamber and roller rotors at 80°C for 10 min at 60 rpm. The material was subsequently removed and re- introduced in the mixer at 180°C and 60 rpm to accomplish the grafting reaction and obtain EOC-g-VTEOS or EOC-g-VTES, depending on the type of monomer used. The grafting mechanism has been described elsewhere [138]. After completion of the grafting reaction (about 5 min) the fillers were added and compounded for a total of 12 minutes, according to the compositions given in Table 5.1. The weight fractions shown in Table 5.1 were converted to volume fractions by using a density of 2.2 $g.cm^{-3}$ for the nanosilica, 0.864 $g.cm^{-3}$ for the solid polymer and 0.760 $g.cm^{-3}$ for the molten polymer [139].

Table 5.1 EOC/nanosilica compositions in weight and volume percent.

Nanosilica Content (wt%)	Vol% Solid State	Vol% Melt State
4	1.61	1.42
5	2.02	1.78
7	2.87	2.53
10	4.18	3.70
12	5.08	4.50

It should be noted that the calculated volume fractions represent the volume that the fumed silica would occupy if it were in a compacted state. The open structure of the fumed silica however renders the effective volume fraction significantly larger than this calculated value [124].

Therefore due to the extremely low bulk density of the nanosilica, a 12 wt% composite is already highly filled. We have not attempted to study composites with higher filler loadings due to difficulties in melt compounding higher amounts of silica. Additionally, the contents of interest from a practical standpoint are well below 12 wt%.

5.2.3 Characterization of functionalized EOC

FT-IR spectra were obtained using a Nicolet Avatar 360 FTIR ESP instrument. Graft contents were calculated from FT-IR integrations of the absorbance of the silanes relative to an internal standard peak originating from the plain matrix. Purification of the polymer prior to FT-IR evaluations was carried out by dissolution in hot refluxing xylene, precipitation from acetone, and drying under vacuum at 60°C overnight.

A calibration curve for the determination of the graft content was obtained by using known mixtures of the polymer matrix and the VTE(O)S monomers as standards. Based on this method, the amount of VTE(O)S grafted onto the EOC matrix was estimated to be 0.8wt%.

Grafting of a silane in the presence of peroxide alters slightly the rheological properties of the starting EOC material, as shown in Figure 5.1, because in the presence of free radicals, chain scission and recombination takes place. Recombination is the dominant mechanism for the polyethylene-based copolymers used in this work, thus a slight increase in viscosity compared to the base material is observed.

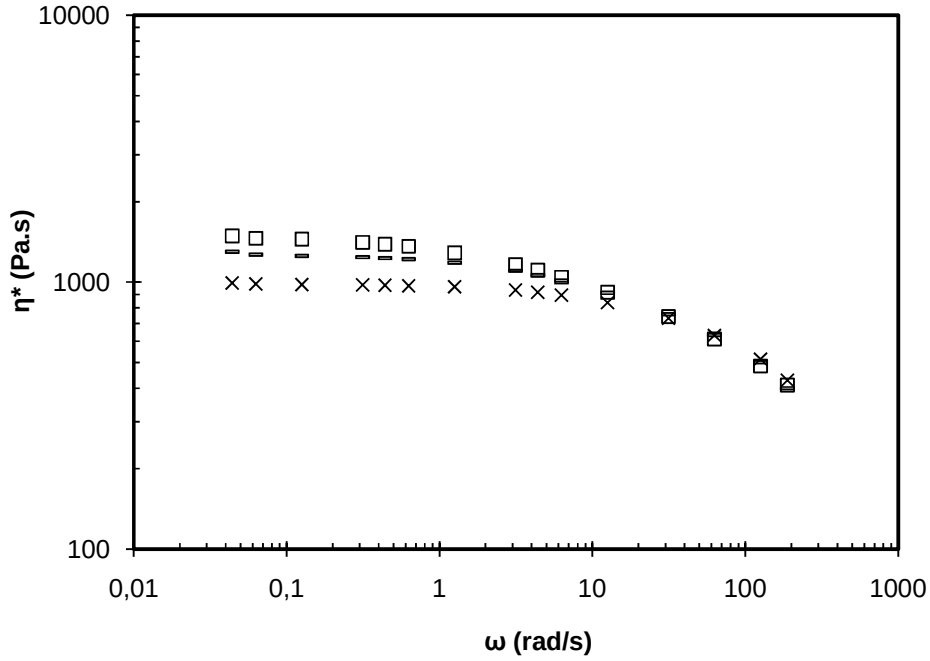

Figure 5.1 Complex viscosity versus frequency for unfilled EOCs at 190°C. (x) EOC; (-) EOC-g-VTES; (□) EOC-g-VTEOS.

5.2.4 Morphology

The state of dispersion of the fillers was assessed by TEM imaging. Samples were compression-moulded using a Carver press at 150°C and 10 MPa for 1 min. Ultra-thin sections were prepared using a Leica ultra microtome. The images obtained using a FEI Tecnai 20 instrument were converted into binary digital images according to the procedure described by Yatsuyanagi et al. [140]. Image analysis was subsequently performed using the SigmaScan Pro software to measure the area of the black colored phase corresponding to the silica particles and aggregates.

5.2.5 Rheological Properties

Rheological characterization was carried out using a Reologica ViscoTech oscillatory rheometer equipped with 20 mm parallel plate fixtures under nitrogen purge, under a gap of 1 mm. Compression-moulded disks with a diameter of 20 mm were prepared using the Carver press, as described above.

Stress sweep experiments were carried out from 1 to 10^4 Pa at a frequency of 0.1Hz and temperature of 200°C. LVE frequency sweep experiments were performed in the dynamic oscillatory mode, under a constant strain of 10%, unless otherwise indicated. The elastic modulus (G'), loss modulus (G") and complex viscosity (η*) were measured as functions of the angular frequency (ω) at temperatures ranging from 80°C to 200°C. Time sweeps were performed at strains ranging between 1 and 10%, frequency of 0.1 rad/s and temperature of 190°C.

Pre-shearing or annealing are commonly used to ensure a consistent shear history of silica suspensions prior to rheological evaluations [33,123]. However in this work since the primary concern was to correlate the rheological response to the structure of compression molded samples as evidenced by TEM imaging, no further shearing was applied to the compression molded disks used for rheology, unless otherwise specified.

The plateau modulus was estimated via the integration of the G"(ω) method, which assumes that the distribution of the loss modulus with frequency is symmetric [141].

$$\boldsymbol{G_N = \frac{4}{\pi}\int_{-\infty}^{\omega_{max}} G"(\omega) d ln \omega} \quad (5.1)$$

where ω_{max} is the frequency at which G" reaches a maximum.

Whenever possible (at low filler loadings), time temperature superposition (TTS) from 80°C to 200°C was carried out to obtain the widest possible frequency range for this determination. At higher loadings, where TTS was not applicable, the measurements obtained at the lowest temperature (80°C) were used for the estimation of the plateau modulus. The Generalized Maxwell model was employed to obtain the relaxation spectrum of the composites. A Fortran-based non-linear optimization program (UBCFIT), developed at the University of British Columbia, which follows the algorithm first developed by Baumgaertel at al. [142] and is based on the determination of the least number of (λ_k, H_k) parameters (Parsimonius spectrum) needed to provide a good fit was used. The Generalized Maxwell model was implemented to obtain the G"(ω) versus ω function, which was then integrated in Eq. (5.1).

5.2.6 Bound Polymer Determination

Chopped composites (1g) were dissolved into 40 mL of toluene at 80°C for 3 hrs to dissolve the polymer that was not bound to the filler. After cooling, the solution was subjected to centrifugal separation at 4000 rpm for 1h. The supernatant was decanted and the gel was shaken with 30 mL of fresh toluene before being left to stand for 1h. Centrifugal separation was repeated and the remaining gel containing the bound polymer and silica particles was dried under vacuum at 60°C overnight. The amount of bound polymer was determined using a TA Instruments Q500 series thermogravimetric analysis instrument to heat samples under nitrogen atmosphere from 25°C to 700°C at a rate of 10°C/min. Percent weight losses recorded for the SiO_2 and oct-SiO_2 particles for the plain and extracted composites were used to calculate the amount of polymer bound to the filler.

5.2.7 Dynamic Mechanical Analysis

Dynamic mechanical properties were studied on rectangular 57.4x6.9x1mm compression-molded samples using a Rheometer Solid Analyzer RSA-II. The instrument was operated in the dual cantiliver configuration. The dynamic responses were tested from -100 to 20°C at a frequency of 1Hz and a heating ramp of 2°C/min.

5.3 Results

5.3.1 Morphology

Figure 5.2 displays the TEM images of the four different systems containing 7 wt% (Figure 5.2 (a1-d1)) and 12 wt% silica (Figure 5.2 (a2-d2)). Silica exists in an aggregated state with the size and shape of the aggregates varying slightly, depending on the type of matrix and particles used. Increasing the filler loading results in an increase in the area of the aggregates and a decrease in the inter-aggregate distance. At 12 wt% the composites appear to be almost interconnected, signifying that this composition is at the vicinity of the percolation threshold (Figure 5.2 (a2-d2)). Based on the images, nanosilicas dispersed within a polyolefin have a fractal structure, similar to that inferred for various colloidal and fumed nanosilica suspensions in liquid media. Fractal dimensions can be estimated based on image analysis of the TEM images, using the software developed by Sasaki et al. [143]. According to this method, the fractal dimension d_f ranges between 2.2 and 2.4 for all the composites.

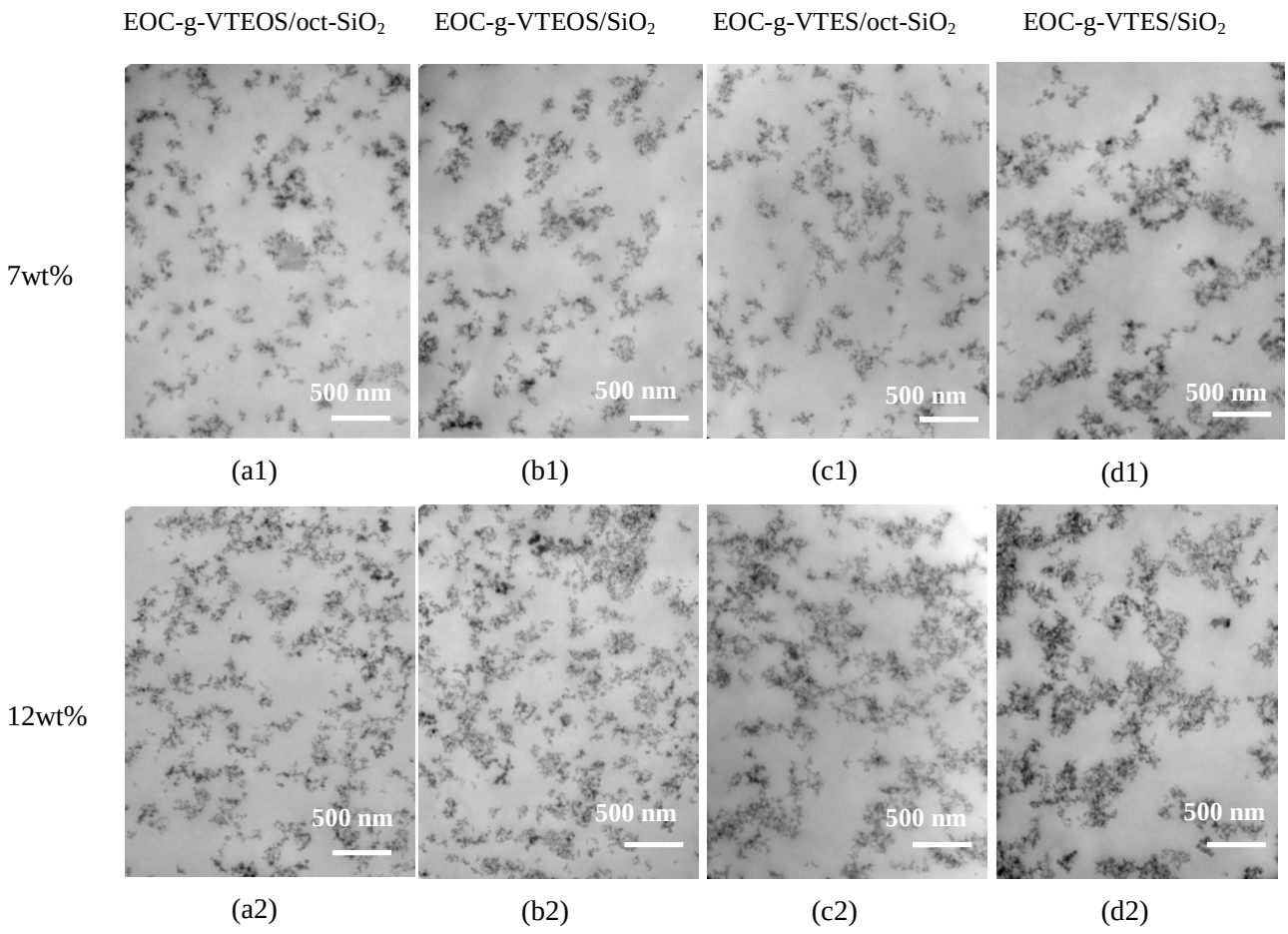

Figure 5.2 TEM images of composites having different matrices: (a) EOC-g-VTEOS/oct-SiO_2; (b) EOC-g-VTEOS/SiO_2; (c) EOC-g-VTES/oct-SiO_2; (d) EOC-g-VTES/SiO_2. (a1-d1) 7 wt% silica, (a2-d2) 12 wt% silica. The scale bar represents 500 nm.

The results of the image analysis shown in Figure 5.3 compare the size distribution of silica aggregates (Figure 5.3 (a)) and their relative contribution to the total area of the silica by size range (Figure 5.3 (b)), at a 7 wt% loading.

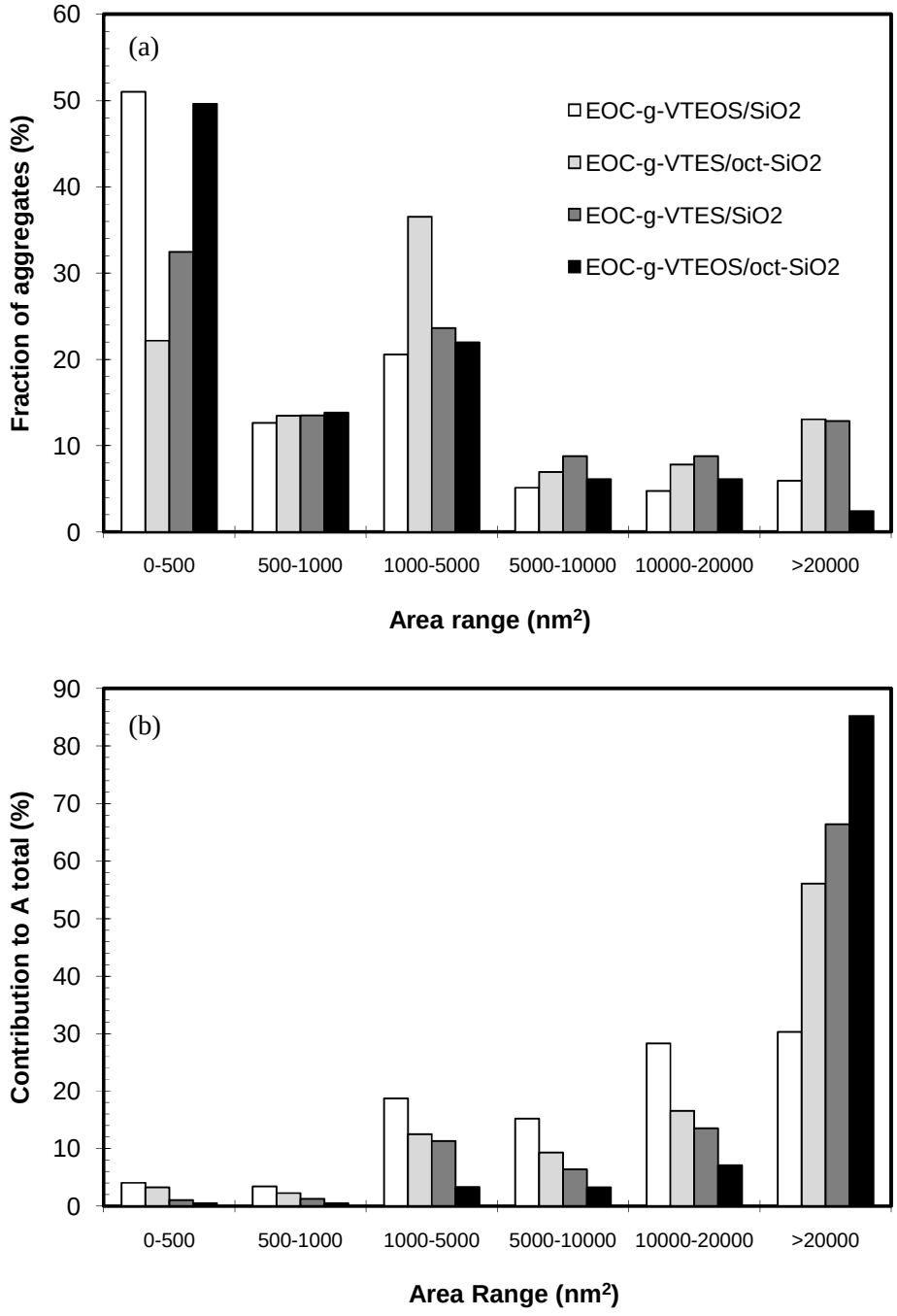

Figure 5.3 (a) Silica aggregate size distribution based on the number of aggregates and (b) % contribution to the total area per range of aggregate size. Silica loading is 7wt%.

It is obvious from these graphs that the size distribution of the aggregates (Figure 5.3 (a)) depends on the nature of the matrix and the silica treatment. Composites based on EOC-g-VTEOS have a higher fraction of isolated particles (area<500nm^2) and a smaller amount of large aggregates (area>20,000nm^2) than composites based on EOC-g-VTES, which display a higher fraction of large aggregates. Additionally, the fraction of very large aggregates is reduced when oct-SiO_2 particles are used, as opposed to SiO_2 particles. Figure 5.3 (b) reveals that the vast majority of the silica particles can be found in large aggregates (e.g. 85% for EOC-g-VTES/SiO_2), except for EOC-g-VTEOS/oct-SiO_2 which shows a more balanced distribution.

Apart from the size distribution of the aggregates, image analysis clearly confirms that their aspect ratio (defined as the smallest dimension over the largest dimension orthogonal to it) strongly depends on their size; the bigger the aggregate, the less spherical it is. Aspect ratios below 0.2 were found for the large aggregates having area above 20,000 nm^2, implying that they do not have a spherical shape; rather they appear to have a fractal structure [133].

The improved dispersion of the oct-SiO_2 particles within the polymer matrix is most likely due to the disruption of the hydrogen bonds between the silanol groups that cause aggregation. In the presence of the silane coating agent the specific component of the surface tension is lowered substantially, whereas the dispersive component becomes more significant, improving the affinity with the polyolefin matrix [144].

Dispersion is further facilitated by improving the stress transfer between polymer and fillers during compounding, thus breaking the aggregates apart. This can be achieved by establishing stronger P/F interactions. The difference between VTEOS and VTES lies in the presence of the

ethoxy groups in VTEOS instead of the alkyl groups in VTES. The hydroxyl groups present at the surface of the particles can react with the ethoxy groups of VTEOS through a hydrolysis reaction similar to Scheme 4.1, thus establishing strong interfacial interactions between the polymer and fillers. However, in the absence of the ethoxy group in VTES, this reaction cannot take place.

The effectiveness of this functionalization approach is seen by comparing Figure 5.2 (b1) with (d1), as well as Figure 5.2 (b2) with (d2). In the presence of covalent bonds when the EOC-g-VTEOS matrix is used, the dispersion of unmodified SiO_2 particles appears substantially improved. The EOC-g-VTEOS/oct-SiO_2 composite (Figure 5.2 (a1) and (a2)) contain the lowest fraction of the large aggregates compared to the rest of the composites (see also Figure 5.3). This composite has benefited from particle modification, which reduces the F/F interactions, while still maintaining some capacity for P/F interactions through covalent bonding, since the hydroxyl groups are only partially replaced by the silane coating agent.

Based on the above results, filler dispersion is obviously affected by the presence and extent of P/F interactions. Bound polymer characterizations are frequently used in rubber technology as a means to quantify P/F interactions [9]. This technique has been applied to the composites under consideration in this work, as described below.

5.3.2 Bound polymer characterizations and effective volume

As shown in Table 5.2 the amount of polymer that is bound to the filler is higher in the EOC-g-VTEOS-based composites compared to the ones having EOC-g-VTES as the matrix. SiO_2 particles have the most potential for covalent bond formation between the silanol groups and the VTEOS grafts and therefore have the highest amount of bound polymer. The presence of bound

polymer in EOC-g-VTES-based composites may be attributed to residual polymer that has been physically adsorbed or trapped within the large particle aggregates [8,140].

Table 5.2 Amount of bound polymer and estimated thickness of polymeric shell surrounding the particles, for composites containing 7wt% silica.

	EOC-g-VTEOS/ oct-SiO_2	EOC-g-VTEOS/SiO_2	EOC-g-VTES/ oct-SiO_2	EOC-g-VTES/SiO_2
Bound polymer (wt%)	7.0	10.2	3.5	6.1
Bound polymer per mass of silica (g/g)	1.0	1.5	0.5	0.9
Shell thickness estimated from bound polymer (nm)	2.9	3.8	1.7	2.7
Shell thickness estimated through eq. (5.2) and (5.4) (nm)*	2.5	2.9	N/A	N/A

* Using the least squares method.

The presence of an immobilized "bound" polymer layer has been related to substantial increases in the rheological properties of filled polymers. The concept of an "effective volume fraction" which takes into account not only the volume occupied by the particles, but also that of the rigid shell surrounding them, has been used to explain this increase. Assuming an idealized case of spherical silica particles of density 2.2 $g.cm^{-3}$ and diameter of 12 nm surrounded by a bound polymer shell of density 0.864 $g.cm^{-3}$, the shell thickness can be estimated. The results are presented in Table 5.2.

In addition to the calculation of the shell thickness, an effective particle volume fraction can be estimated from values of the plateau modulus by using the modified Guth-Smallwood equation [67] proposed by White and Crowder [145].

$$G_N(\phi_e) = G_N(0) \cdot (1 + 2.5\phi_e + 14.1{\phi_e}^2) \quad (5.2)$$

where G_N is the plateau modulus and ϕ_e the effective volume fraction.

White and Crowder proposed an expression to estimate the effective volume fraction based on the average particle diameter d and the shell thickness Δ:

$$\phi_e = \phi + \left(\frac{6\phi}{d}\right)\Delta \quad (5.3)$$

Heinrich and Kluppel [133] proposed an alternative expression, shown in Eq. (5.4) to take into account the fact that particles are inter-connected and therefore the shell does not exist at the particle-particle intersection.

$$\phi_e = \frac{(d+2\Delta)^3 - 6d\Delta^2}{d^3}\phi \quad (5.4)$$

where d is the average particle diameter (12 nm in our case) and Δ is the shell thickness, provided that Δ<<d [133].

Eq. (5.2), in combination with Eq. (5.4), was used to fit the experimental data of plateau modulus versus volume fraction. A representative fit is shown in Figure 5.4 for the EOC-g-VTEOS/oct-

SiO_2 composite. The fitted values obtained for EOC-g-VTEOS/oct-SiO_2 and EOC-g-VTEOS/SiO_2 are shown in Table 5.2.

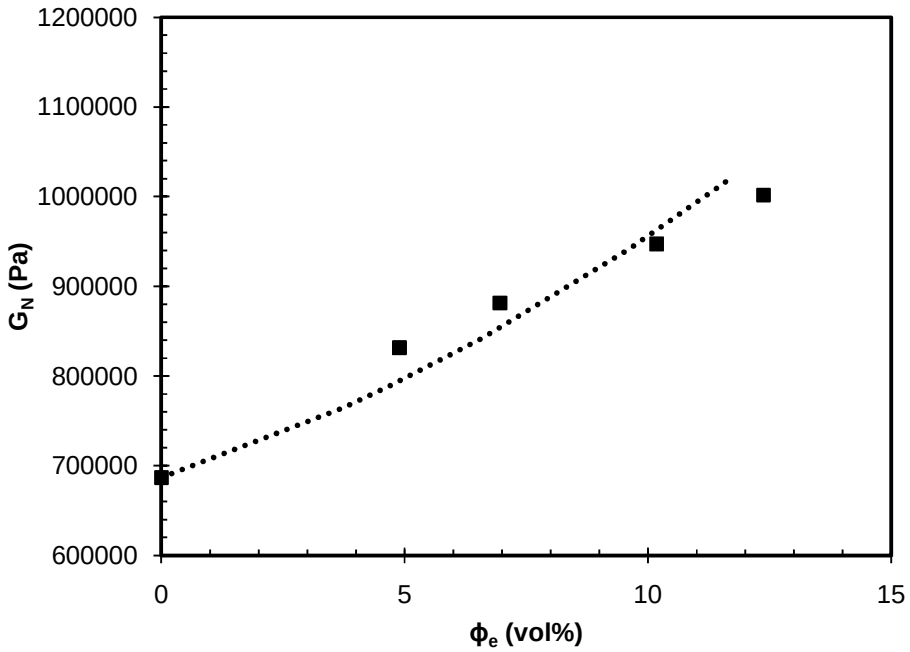

Figure 5.4 Fit of the experimental values of the plateau modulus (squares) of the EOC-g-VTEOS/oct-SiO_2 composite using the modified Guth-Smallwood equation (dashed line) at a fitted value of the shell thickness (Δ=2.5nm).

Values for the EOC-g-VTES composites are not presented here because of the uncertainties in the rheological characterization leading to the estimation of the plateau modulus, due to pronounced time dependent effects, as explained later in section 5.3.3. Although the values of the shell thickness are lower than the ones estimated through the bound rubber characterization (which were based on the idealized case of spherical silica particles), the trends are the same and verify that the EOC-g-VTEOS/SiO_2 composite has more bound rubber, because the unmodified SiO_2 has a higher number of free silanol groups that are able to engage in covalent bonding with the

matrix. Overall the values of the shell thickness are in the same order of magnitude and agree with literature reports [9,33]. It should be noted that the effective volume fraction estimated using this approach is about 2.5 - 3 times the real volume fraction, as shown in Figure 5.5.

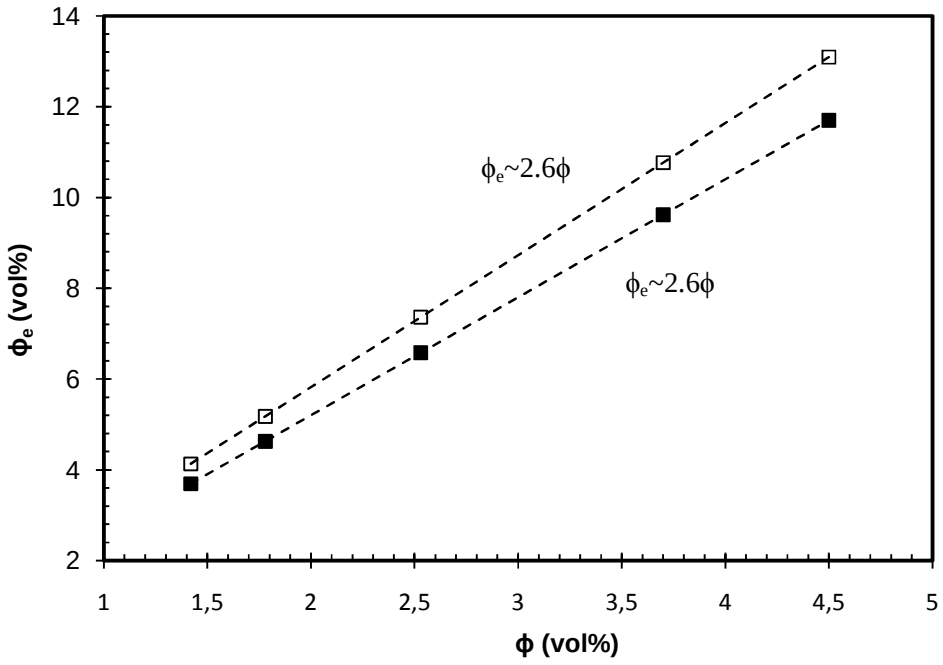

Figure 5.5 Effective filler content, in volume percent, ϕ_e vs. actual filler content, in volume percent, ϕ. (■) EOC-g-VTEOS/oct-SiO_2; (□) EOC-g-VTEOS/SiO_2.

This agrees with the values obtained by Zhang and Archer [33] and supports the hypothesis of the existence of a bound polymer layer surrounding the silica aggregates that causes an enhanced hydrodynamic effect. The effective volume fraction is higher for the EOC-g-VTEOS/SiO_2 composite, consistently with its larger shell thickness.

5.3.3 Shear Oscillatory Rheology

5.3.3.1 Frequency sweeps

Frequency sweeps demonstrate deviations from terminal flow behaviour at filler loadings above 5-7wt% (Figure 5.6), suggesting that the motion of the polymer chains becomes restricted above this filler loading.

The deviation can be better seen from the insets in Figure 5.6, which summarize the normalized moduli as a function of filler loading. It should be noted that the emergence of a low-frequency plateau is only seen at the highest filler loadings. For all other compositions the values of the loss tangent, tanδ, remain higher than one, indicating a viscoelastic-liquid response, which is consistent with the fact that these composites are below the percolation threshold, as evidenced by TEM (Figure 5.2).

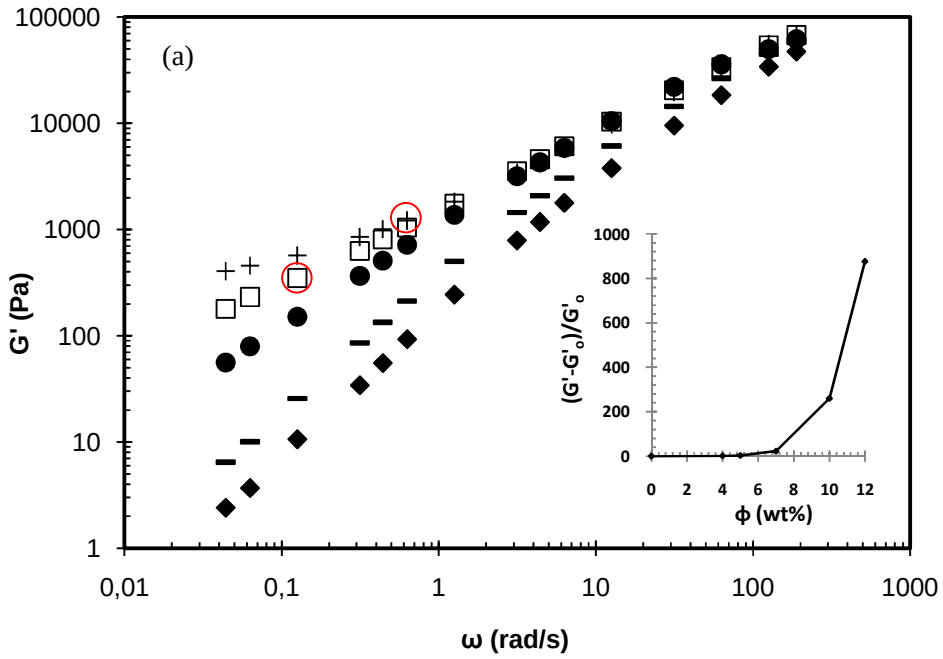

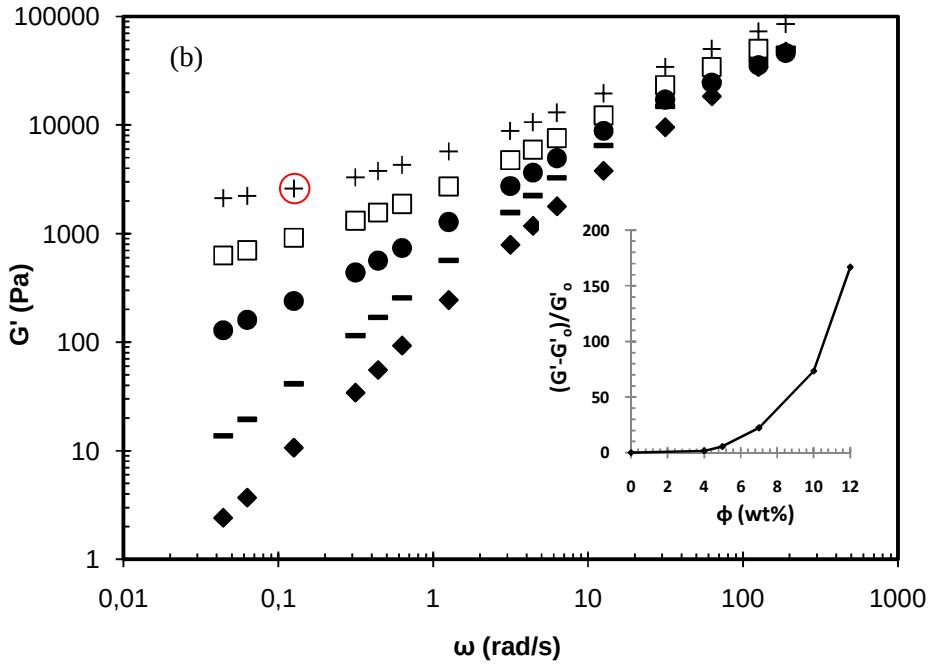

Figure 5.6 Frequency dependence of the storage modulus (G') for (a) EOC-g-VTEOS/oct-SiO_2 and (b) EOC-g-VTEOS/SiO_2 composites at 190°C. SiO_2 or oct-SiO_2 content: (◆) 0wt%; (-) 4wt%; (●) 7wt%; (□) 10wt%; (+) 12wt%. Cross-over points of storage and loss moduli are circled. Insets show the normalized moduli with respect to the matrix modulus, G'_o at ω=0.04 rad/s.

Figure 5.7 shows a representative frequency sweep for the neat polymer and the EOC-g-VTEOS/SiO_2 composite. In contrast to the simple dynamics and terminal flow behaviour demonstrated by the matrix, the composites exhibit a cross-over at low frequencies at the highest filler loadings, indicating a viscoelastic solid-like response. These complex frequency and volume fraction dependencies are attributed to the interaction between the filler structure and the viscoelastic response of the matrix [146]. Both the frequency and the modulus at which this cross-over appears increase with filler loading, as shown in Figure 5.6.

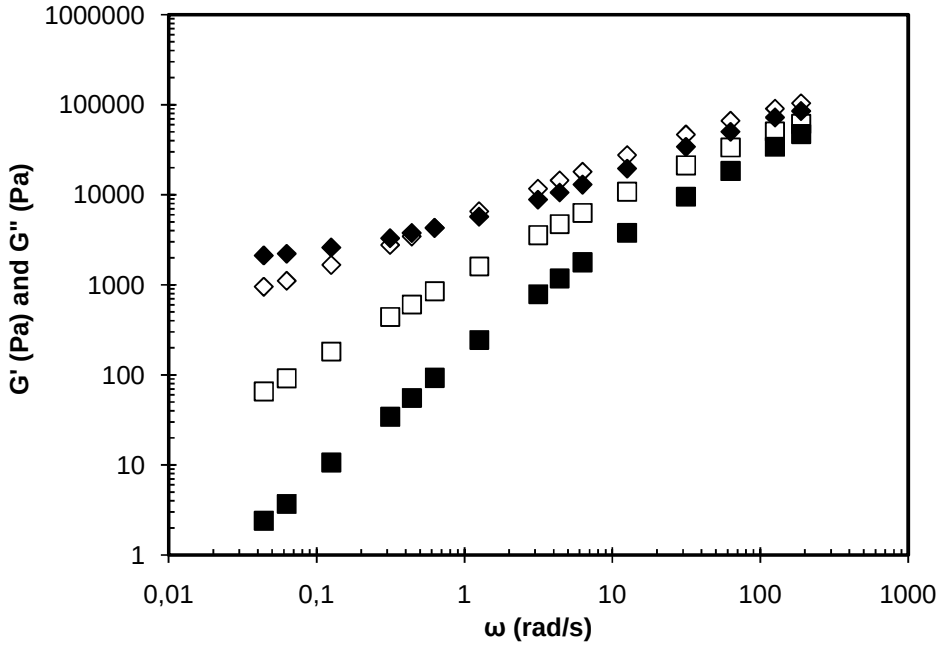

Figure 5.7 Frequency sweep at 190°C of EOC-g-VTEOS (squares) and EOC-g-VTEOS/12wt% SiO_2 (diamonds). G' (full symbols) and G" (empty symbols).

Figure 5.8 summarizes the G'_0 vs. volume fraction dependency at the lowest accessible experimental frequency, $G'_0=G'(\omega=0.04rad/s)$. A smooth scaling relationship of $G'_0 \sim \phi^m$ between G'_0 and filler loading is seen, with the exponent values for the EOC-g-VTEOS based composites shown in Table 5.3. For the EOC-g-VTEOS/oct-SiO_2 composites a scaling relation of $G'_0 \sim \phi^{3.5}$ is obtained. This is strikingly similar to the reports by Zhu et al. on polybutadiene nanosilica suspensions [147] and representative of reinforcement due to the formation of a fractal structure [133,134]. The dependency is sharper for the EOC-g-VTEOS/SiO_2 composite, presumably because of an enhanced hydrodynamic effect.

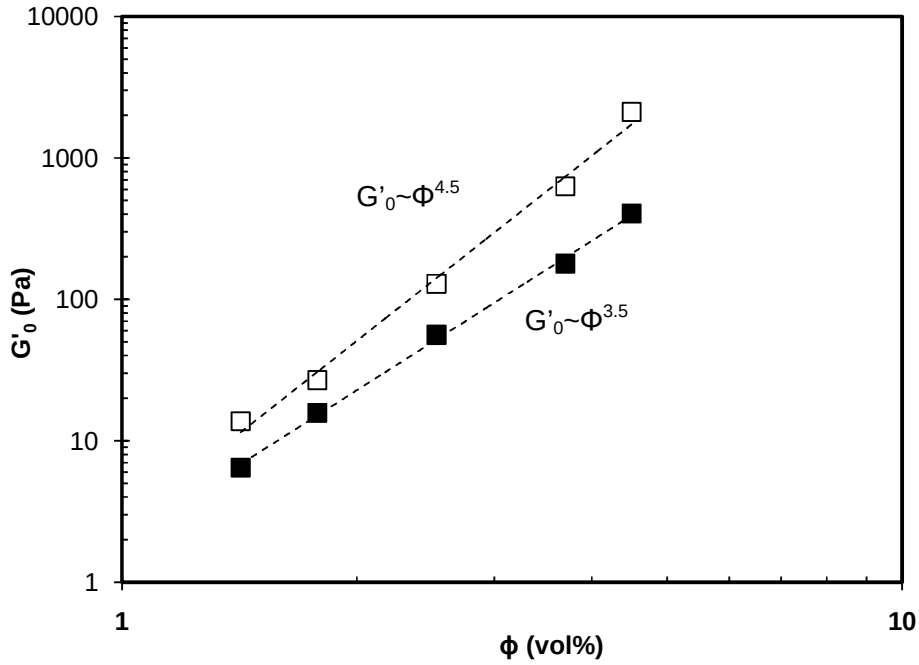

Figure 5.8 Elastic modulus at ω=0.04 rad/s as a function of the silica loading. (■) EOC-g-VTEOS/oct-SiO_2; (□) EOC-g-VTEOS/SiO_2. Lines indicate exponential model fit.

Several models have been proposed to describe the fractal structure arising from colloidal particle aggregation processes. Piau et al. considered non-fluctuating semidilute fractal objects, and showed that the elastic modulus scales with the volume fraction according to a power-law, $G'_0 \sim \phi^m$, where the exponent m contains the fractal dimension, d_f [127].

$$G'_0 \sim \phi^{\frac{5}{3-d_f}} \tag{5.5}$$

Values of the fractal dimension d_f can be experimentally obtained either by image analysis [132], light scattering experiments [127] or indirectly by rheology [148]. The values of the fractal

dimension obtained through Eq. (5.4) and reported in Table 5.3 are very close to literature reports.

Table 5.3 Values of exponent, m, and fractal dimension, d_f (Eq. (5.5) obtained by curve fitting the G'_0 vs. ϕ data. The reported values include the 95% confidence intervals.

	EOC-g-VTEOS/oct-SiO_2	EOC-g-VTEOS/SiO_2
m	3.5±0.1	4.4±0.2
d_f	1.6±0.04	1.9±0.05

For example Piau et al. reported an exponent of m=4.2±0.8 and a corresponding fractal dimension of d_f=1.8±0.2 for PDMS/SiO_2 gels. A lower value of d_f is obtained for EOC-g-VTEOS/oct-SiO_2 composites. This value is consistent with the predictions of the cluster-cluster aggregation (CCA) model, which is based on the concept that particles can fluctuate around their mean position to eventually lead to a space-filling configuration of fractal CCA-clusters [133]. The CCA model predicts m≈3.5 and d_f≈1.8, which is very similar to our results for the EOC-g-VTEOS/oct-SiO_2 composite.

The LVE results demonstrate that the magnitude of the modulus at low frequencies and the corresponding scaling factors and fractal dimensions vary depending on the type of matrix and nature of filler treatment. Further insight on the effect of P/F interactions on the rheological properties is provided through time-sweeps and strain-sweeps, as discussed below.

5.3.3.2 Time Sweeps

It is well known that suspensions of fumed silica experience microstructural rearrangements during shear, leading to flocculation and formation of particle aggregates [33,123]. Functionalized polyolefins that are commonly used as nanocomposite matrices are also prone to time-dependent effects, because of the propensity for functional group associations [149].

Time dependency was noted at filler loadings above 5 wt%, signifying that a certain amount of filler is required in order to observe a rearrangement and a corresponding increase in modulus, as pointed out previously by Romeo et al. [146]. A pronounced increase in storage modulus was seen for the EOC-g-VTES-based composites, as shown in Figure 5.9, suggesting that the silica particles have the propensity to associate and form aggregates when exposed to low strains during the time sweeps. This was the reason why these composites were excluded from the prior analysis of the frequency sweeps. The significantly higher starting elastic modulus values seen for the EOC-g-VTES/SiO_2 composite in Figure 5.9 are most likely related to the higher state of aggregation of the filler in this particular matrix.

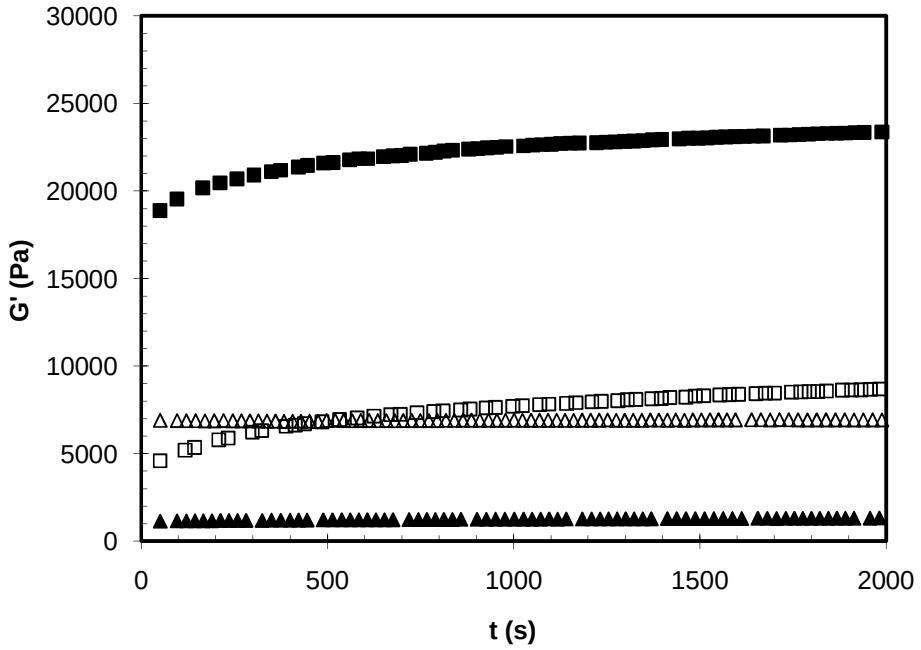

Figure 5.9 Storage modulus G' as a function of time, at 190°C under a 2% strain and 0.1Hz frequency. Silica content is 12wt%. (▲) EOC-g-VTEOS/oct-SiO_2; (△) EOC-g-VTEOS/SiO_2; (□) EOC-g-VTES/oct-SiO_2; (■) EOC-g-VTES/SiO_2.

The dramatic increase seen in these composites implies that the free silanol groups existing on the silica surface maintain their capability to associate through hydrogen bonding under the low strains imposed during the time sweep experiments, thereby leading to strong F/F interactions and thus aggregation. The situation changes when the VTEOS-based matrix is used, since the silanol groups are now able to form covalent bonds with the ethoxysilane functionality. This limits their capacity to associate with each other and form aggregates, leading to a steady rheological response, presumably attributed to a more stable morphology.

It is also noteworthy that these composites are very sensitive to pre-shearing, indicating that the flocculated clusters of silica can be broken down by relatively high levels of shearing. Furthermore the rate and extent of modulus recovery following preshearing depends on the strain level imposed during time sweeps, as shown in Figure 5.10.

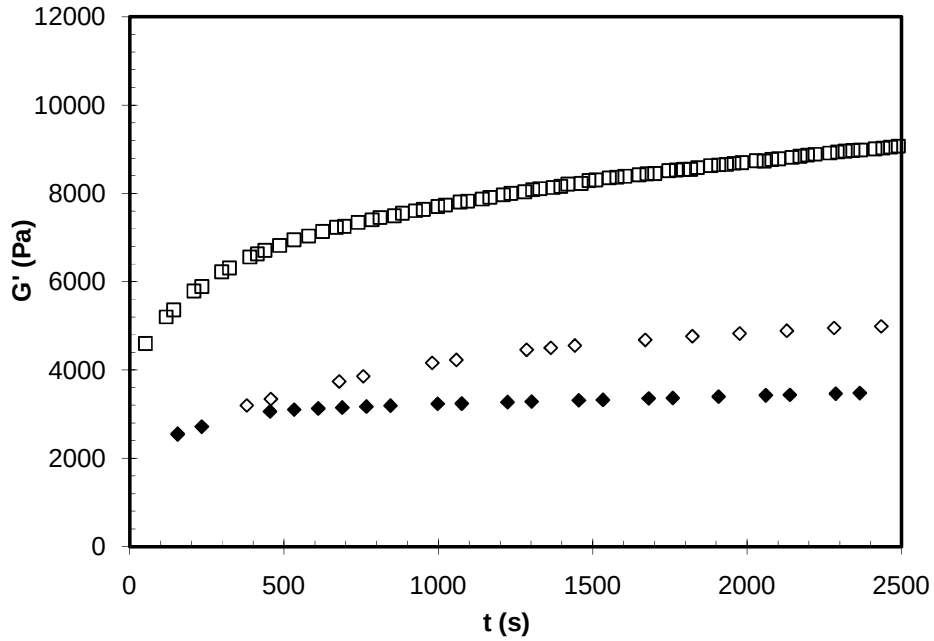

Figure 5.10 Storage modulus as a function of time for EOC-g-VTES/oct-SiO_2 12wt% at 190°C and 0.1Hz frequency: (□) no preshear; (◇) pre-sheared at 1000 Pa for 100 s, strain of 1% during time sweep; (◆) pre-sheared at 1000 Pa for 100 s, strain of 10% during time sweep.

Higher levels of strain during the time sweeps result in a break-down of the structure, which counteracts the continuous buildup, leading to lower values of the modulus and the appearance of a plateau.

5.3.3.3 Stress sweeps

A pronounced difference in strain dependence between the EOC-g-VTEOS and the EOC-g-VTES-based composites at filler loadings above 7wt% is revealed from the stress sweeps, shown in Figure 5.11.

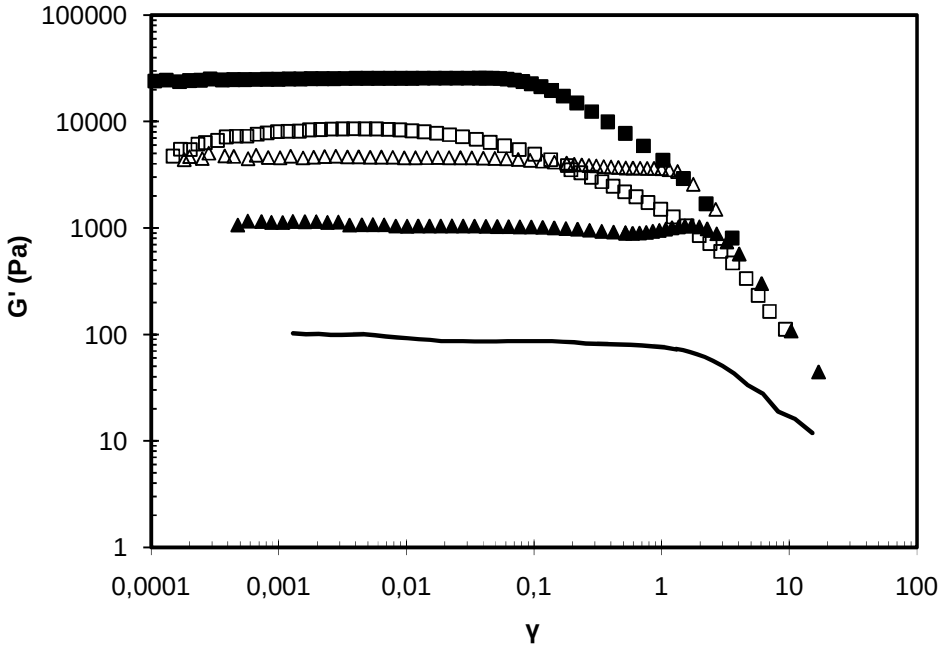

Figure 5.11Storage modulus vs. strain at 200°C, 0.1Hz at a silica loading of 12 wt%; (▲) EOC-g-VTEOS/oct-SiO_2; (△) EOC-g-VTEOS/SiO_2; (□) EOC-g-VTES/oct-SiO_2; (■) EOC-g-VTES/SiO_2. The solid line represents the unfilled EOC-g-VTEOS matrix.

The critical strain, γ_c, for the onset of non-linearity is significantly lower for the EOC-g-VTES compared to the EOC-g-VTEOS-based composites, with the latter being more strain resistant (Figure 5.11). Given that a "filler network" does not exist at the loadings used in the present work, the drop of γ_c is most likely attributed to the breakdown of the nanosilica aggregates during

the stress-sweep [8,128,130,148,150]. The EOC-g-VTES/oct-SiO_2 composite shows a very strong strain dependence; the elastic modulus curve increases at moderate strains, and subsequently decreases. The initial increase may be due to "strain-induced" aggregation. This is in agreement with the findings from the time sweep reported previously, where this particular composite seemed to be prone to aggregation.

The critical strain for the onset of non-linearity shifts to lower strain values upon increasing silica concentration. This is shown in Figure 5.12, which summarizes the critical strain, estimated as the strain reached when the modulus is equal to 95% of the plateau modulus as a function of the silica loading [151]. Given the absence of a well-defined linear region for EOC-g-VTES/oct-SiO_2, data are not shown for this particular composite. The data can be fitted using a power-law scaling relation [65,130].

$$\gamma_c \sim \phi^{-\upsilon} \tag{5.6}$$

where ν is a parameter, which according to the literature ranges in value from 0.7 to 4.0 and depends on the interparticle forces [65].

The EOC-g-VTES-based composites are significantly more sensitive to strain, resulting in an exponent of 1.6±0.2 for EOC-g-VTES/SiO_2. On the contrary the EOC-g-VTEOS-based composites are more resistant to strain, with lower exponents, 0.5±0.05 and 0.3±0.04 respectively for SiO_2 and oct-SiO_2 particles.

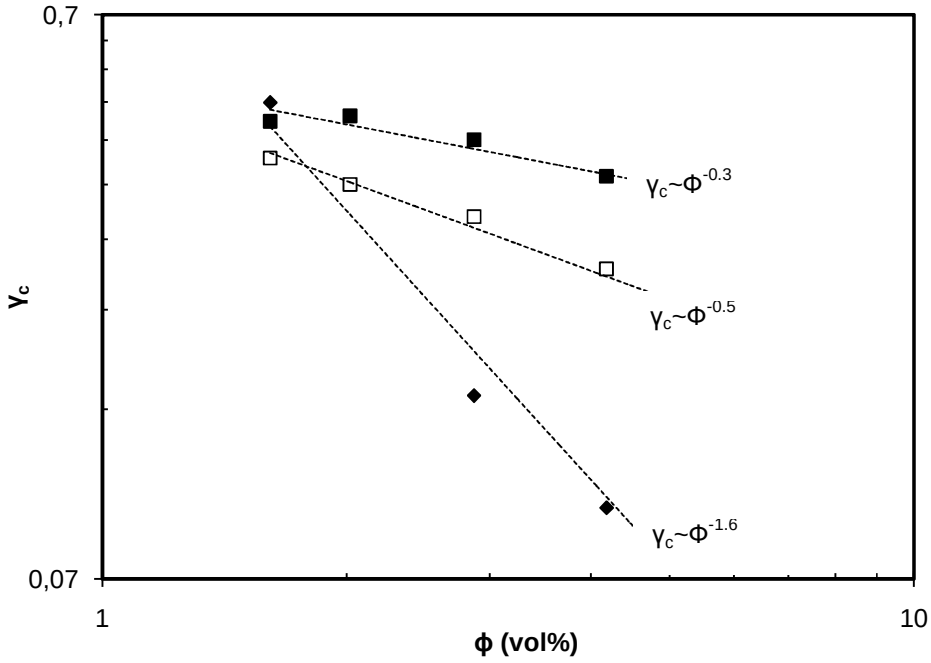

Figure 5.12 Critical strain vs. silica content: (■) EOC-g-VTEOS/oct-SiO_2; (□) EOC-g-VTEOS/SiO_2; (◆) EOC-g-VTES/SiO_2; Lines indicate exponential model fit.

The critical strain can be related to the cohesive energy density, E_c, needed to break the filler structure, according to Eq. (5.7) [152].

$$E_c = \frac{1}{2}\gamma_c^2 G'_{plateau} \qquad (5.7)$$

Application of this equation to our data shows that for EOC-g-VTES/SiO_2 the work required to break down the structure remains around 10 $J.m^{-3}$ irrespective of the filler loading, as opposed to EOC-g-VTEOS-based composites in which E_c increases with filler loading, reaching values

above 50 $J.m^{-3}$ at high loadings. This confirms that the structure of the EOC-g-VTEOS composites, where covalent bonds are present, is much more strain-resistant.

The presence of a small peak in the elastic modulus vs. strain curves of the EOC-g-VTEOS composites at very large strains (Figure 5.11), right beyond the strain where the transition to non-linear behaviour occurs in the pure polymer, is also noteworthy. To our knowledge this has never been reported before, except from a similar observation by Cassagnau [153] in silica-filled EVA/xylene mixtures. One possible explanation is stress-induced debonding of the polymer chains that are bound to the filler surface through covalent bonding.

5.3.4 Dynamic Mechanical Analysis

Figure 5.13 (a) and (b) present the storage and loss moduli as functions of temperature, obtained from the DMA measurements. For clarity, only the composites containing oct-SiO_2 are shown here.

Figure 5.13 (a) shows that although both the neat polymers and the composites have similar values of the storage moduli at temperatures below the glass transition, their behavior at temperatures around and above the glass transition differs, with the EOC-g-VTEOS-based composite showing a higher value of the elastic modulus and a more significant enhancement with respect to the neat polymer. Similarly, as Figure 5.13 (b) shows, the area under the loss modulus vs. temperature curve is higher for the EOC-g-VTEOS based composite, suggesting that more energy is dissipated when the glass transition temperature is reached, at about -50°C.

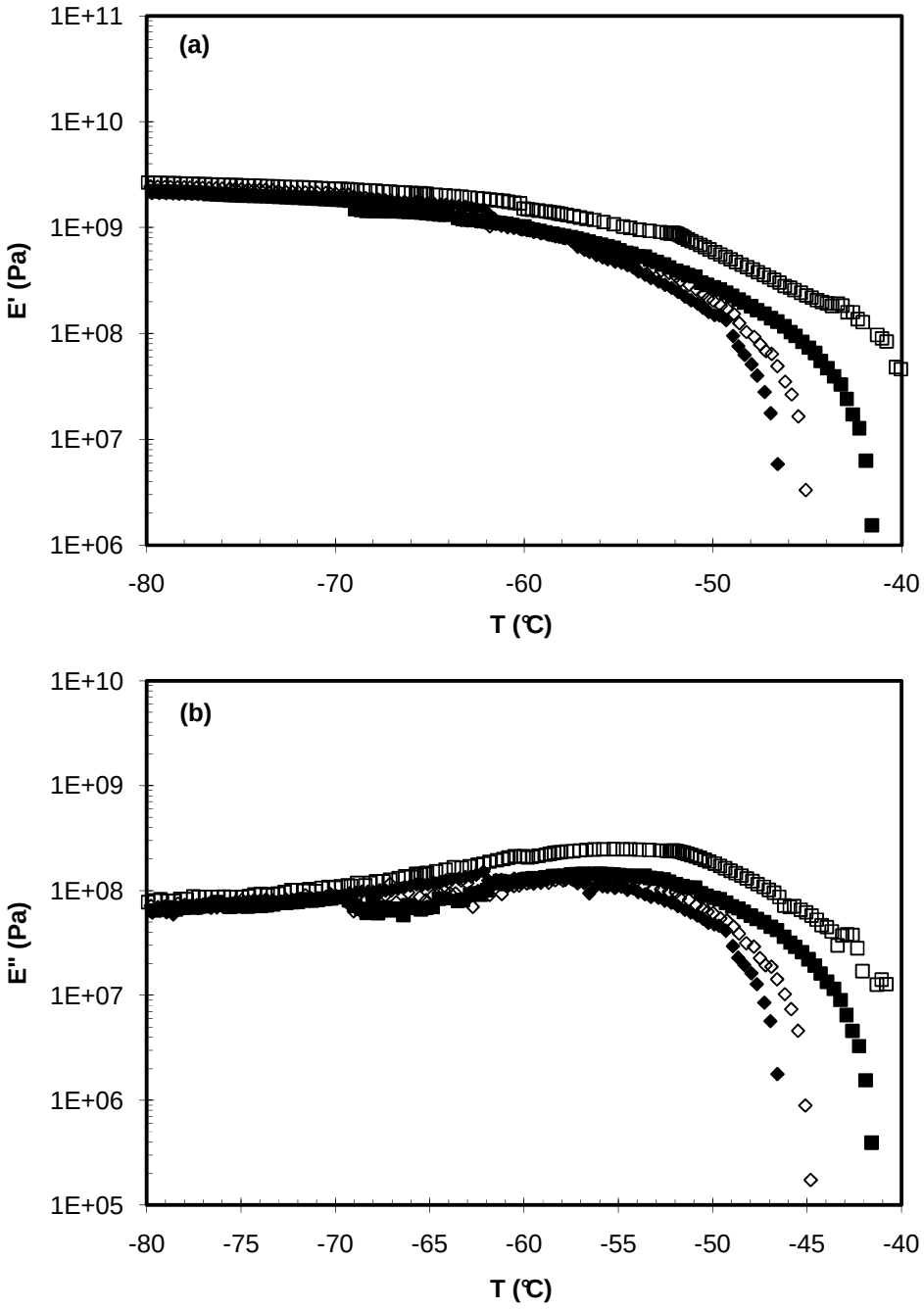

Figure 5.13 DMA curves at 1Hz for composites containing 7 wt% silica: (a) Storage modulus and (b) Loss modulus; (■) EOC-g-VTEOS; (□) EOC-g-VTEOS/oct-SiO_2; (◆) EOC-g-VTES; (◇) EOC-g-VTES/oct-SiO_2; Silica content is 7wt%.

On the contrary the curves corresponding to the EOC-g-VTES composite are very similar to the response of the neat polymer, suggesting a minimal effect of the filler. The type of filler (modified vs. unmodified) did not affect the results, implying that the most important factor is the matrix functionalization. It can be suggested therefore that the dynamic elastic and loss moduli are affected only when P/F interactions are present. Furthermore, these figures suggest a very slight increase in the glass transition temperature, T_g, for the EOC-g-VTEOS composites, presumably because the motion of macromolecules at the vicinity of the nanoparticles is hindered in the presence of chain entanglementsand P/F interactions, therefore leading to a higher T_g [56].

5.4 Discussion

The rheology of filled thermoplastics is influenced by both the presence of nanofillers as well as their state of dispersion. The latter further depends on the extent of F/F and P/F interactions. Given these complex interrelations, it is has been very challenging in the literature to differentiate between the effects of filler dispersion and P/F interactions. In this work, by using two different matrices and two types of silica particles, we were able to gain some insight on the dependence of the composite structure and the various rheological functions on the F/F and P/F interactions.

The different types of F/F and P/F interactions are reflected in the different states of dispersion (Figure 5.2 and Figure 5.3), as well as in the exponents of the $G' \sim \phi^m$ scaling relation (Table 5.3). Enhanced P/F interactions that are mainly attributed to covalent bonding between the surface silanol groups and the functional grafts present in the polymer matrix have an impact on the state of dispersion of the composites. As the results of image analysis showed, composites based on EOC-g-VTEOS present a lower state of aggregation compared to EOC-g-VTES-based

composites, regardless of the extent of F/F interactions (i.e. type of particle used). Overall, EOC-g-VTEOS/oct-SiO_2 displays the finest dispersion because it combines both a lower degree of F/F interactions and stronger P/F interactions.

The increases seen in the viscoelastic properties as a function of filler loading, are obviously attributed first of all to the hydrodynamic effect caused by the nanoparticles, and at higher loadings (above 5 wt% or 2 vol%) to the propensity of the silica particles to aggregate and form flocculated clusters, leading to a fractal structure with dimensions consistent to the predictions of the CCA model.

A volume fraction of ϕ_c=0.05 is generally acknowledged as the critical volume fraction beyond which a network consisting of overlapping clusters is formed, as predicted by Buscall et al.[129] and Huber and Vilgis [134]. Below ϕ_c the elastic modulus varies linearly with volume fraction, whereas above ϕ_c universal behaviour with scalings of $G' \sim \phi^m$ is reported. Interestingly, even though all our composites are below the critical volume fraction of ϕ=0.05, they obey the $G' \sim \phi^m$ scaling behaviour (see Figure 5.8 and Table 5.3), which at first glance is inconsistent. However, the effective volume fractions, which take into account the presence of bound polymer, are actually around three times the actual volume fractions, as implied by Figure 5.5, and may thus account for the observed rheological behaviour.

Measurements in the LVE region are inherently influenced by the degree of dispersion, therefore provide only indirect evidence of the existence of covalent bonding resulting in strong P/F interactions. In this work, the latter became more evident through the time-sweeps, stress-sweeps and DMA analysis. Covalently bridging the polymer chains and the nanoparticles in the EOC-g-VTEOS based composites resulted in "anchoring" of the filler to the polymer chains, thus preventing rearrangements and further aggregation of the particles during time-sweeps (Figure

5.9), in contrast with the EOC-g-VTES composites where covalent bonding was absent. The more stable structure of the EOC-g-VTEOS based composites was also evident from the stress-sweep experiments, where they appeared to be very strain resistant, with critical strain values that were an order of magnitude higher and a cohesive energy density 5 times higher than that of the VTES-based counterparts. The onset of non-linearity for these composites does not seem to be attributed to the breakdown of a filler network, as it has been widely suggested in the past [118,130,131,147,148,154], but rather depends on the type of interfacial interactions between polymer and filler. It should be noted that the EOC-g-VTEOS/oct-SiO_2 composites were the most strain resistant. Although silica particles have been modified, it should be noted that the coating is only partial, leaving a lot of silanol groups available for the reaction. These composites therefore benefit from both the absence of big aggregates, and the presence of covalent bonding. Finally, DMA measurements revealed that the energy dissipated during the glass transition was significantly higher in the EOC-g-VTEOS based composites, and the elastic modulus above the transition was higher.

5.5 Conclusions

Grafting reactive and non-reactive silanes onto an EOC matrix enabled the differentiation between two different types of composites, based on the presence or absence of P/F interactions due to covalent bonding. The amount of bound polymer was higher when VTEOS, which is able to form covalent bonds with the hydroxyl groups of silica, was grafted onto the EOC matrix. Both particle modification and grafting of VTEOS on the EOC matrix contributed to a finer dispersion of the nanoparticles, as revealed through TEM imaging.

The values of the moduli at low frequencies scaled with the volume fraction according to a power-law relation, which is consistent with the presence of a fractal structure. Given that the composites were below the percolation threshold, this observation is attributed to the higher effective volume of the filler particles, in the presence of bound polymer.

Time-sweep experiments showed that the composites were prone to aggregation, in the absence of chemical interactions between filler and hosting polymer. Stress sweeps revealed that VTEOS grafted composites were more capable of enduring high strains without significant network disruption, as their critical strains were much higher compared to VTES grafted composites. This behaviour was attributed to the presence of P/F interactions that create connections between the hosting polymer chains and the nanoparticles. Differences were also detected in the solid state DMA evaluations, which showed that a higher amount of energy is dissipated at the glass transition temperature when the VTEOS based composites were used.

Based on the results of the present Chapter, substantial differences in the rheological response between the composites can only be detected at loadings above 5 wt%. At these compositions, the response is also influenced by the formation of extensive flocculated clusters of aggregated silica. The following two chapters will address this issue by investigating composites containing lower nanosilica contents.

Chapter 6

LINEAR VISCOELASTIC PROPERTIES OF ETHYLENE-OCTENE COPOLYMER / NANOSILICA COMPOSITES INVESTIGATED OVER A BROAD RANGE OF FREQUENCIES

6.1 Introduction

Rheology serves as a valuable tool for the characterization of the molecular architecture (molecular weight, polydispersity, branching level) of polymer melts, and can aid in the prediction of their processing behaviour [155,156]. However, as seen in Chapter 5, the effects of the addition of nanoparticles on the rheological properties of nanocomposites are complex and multiple, and their causes are still subject to debate.

In Chapter 5, the viscoelastic properties of nanocomposites have been found to be deeply influenced by the state of dispersion of the fillers, which is related to the F/F and P/F interactions. Several authors reported specifically the effects of various degrees of P/F interactions when performing SAOS experiments both inside [33,41,45] and outside the LVE region [41,157]. However, as numerous parameters may impact the viscoelastic properties of nanocomposites, several conditions must be satisfied in order to reliably evaluate the viscoelastic properties. Firstly, the filler concentration must remain far below the percolation threshold to prevent particle aggregation and the formation of a filler network, which may affect the rheological properties and mask the effects of P/F interactions. Secondly, the time set for the experiments must remain within the limits of stability of the materials, filled polymers being prone to microstructural rearrangements.

Due to the extremely long relaxation times of polymer melts and the limitation of the time range accessible to SAOS experiments, creep followed by creep recovery experiments have been implemented as a means to extend the experimentally accessible time range. Kaschta and Schwartz combined creep and creep recovery data with oscillatory measurements to obtain dynamic mechanical spectra over a broad range of frequencies on PS, PC and PMMA melts [158,159]. This method has been successfully applied subsequently on various polymer-based materials: on pure polymer melts, such as, LLDPE [160], HDPE [161], PP [162], but also on polymer blends PP/PS [163], and on silica-filled polymers [164,165]. For materials which cannot reach steady-state, *incomplete* creep followed by creep recovery constitutes an alternative option. This method was described in details by He et al. [162] and used on pure HDPE melt [161] and PP/PS blends [163].

The previous chapter investigated polyolefin-based composites containing pristine and surface modified SiO_2 particles, as well as a silane-grafted matrix that was able to form covalent bonds with the silanol groups located at the surface of the nanoparticles. Significant differences in time sweeps, stress sweeps and SAOS experiments were reported, depending on the extent of modification of the matrix and the nanosilica surface. In the absence of any treatment, the viscoelastic properties of the composites increased as a function of experimental time, suggesting a tendency toward aggregation. However these effects were largely confounded with the development of flocculated silica clusters forming a network above a 7wt% loading as observed in Chapter 5. The present chapter focuses on lower silica loadings to minimize the F/F interactions leading to the formation of flocculated structures and thus to better identify the role of the P/F interactions. Various techniques of characterization have been used, including stress

and time sweeps, as well as creep and creep recovery experiments combined with frequency sweeps to extend the accessible time range.

6.2 Theory

The principle of a creep experiment followed by a creep recovery experiment is represented in Figure 6.1. A constant shear stress τ_0 is applied to the sample from t=0 to t=t_1. The stress is removed at t_1. The response of the material is measured in terms of strain as a function of the creep time t_c and the creep recovery time t_r.

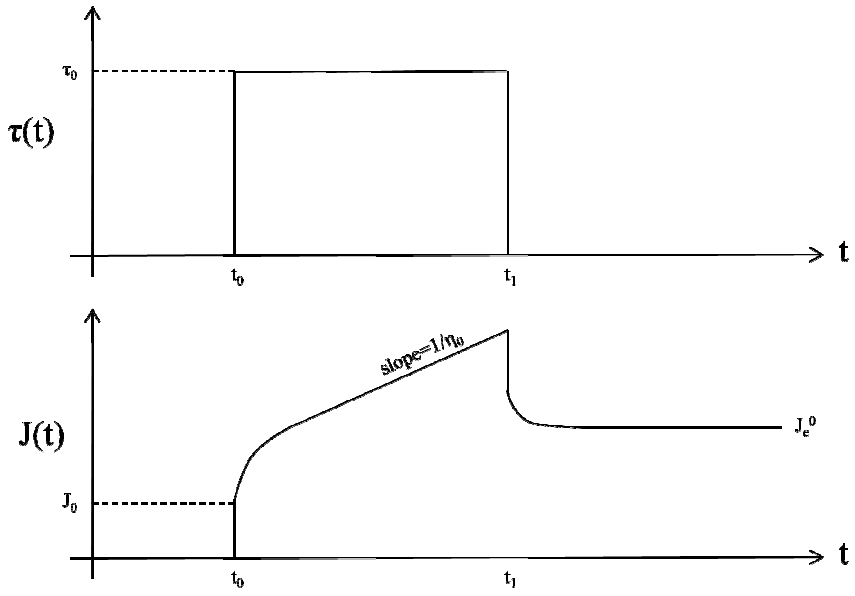

Figure 6.1 Creep and creep recovery experiments.

The strain measured during creep can be converted into a creep compliance according to:

$$J_c(t_c) = \frac{\gamma_c(t_c)}{\tau_0} \tag{6.1}$$

The strain measured during creep recovery can be converted into a recoverable compliance according to:

$$J_r(t_r, t_1) = \frac{\gamma_r(t_r, t_1)}{\tau_0} \tag{6.2}$$

with

$$\gamma_r(t_r, t_1) = \gamma_r(t_1) - \gamma(t_r, t_1) \tag{6.3}$$

According to the theory of linear elasticity [166], the creep compliance can be written as:

$$J_c(t_c) = J_0 + \psi(t_c) + \frac{t_c}{\eta_0} \tag{6.4}$$

where J_0 is the instantaneous compliance, $\psi(t)$ is called the creep function and represents the viscoelastic part of the creep compliance, and η_0 is the steady-shear viscosity.

For sufficiently large values of t_c:

$$J_c(t_c) = \frac{t_c}{\eta_0} \tag{6.5}$$

Additionally the recoverable compliance can be written as:

$$J_r(t_r, t_1) = J_0 + \psi(t_r, t_1) \tag{6.6}$$

and $\lim_{t_r \to \infty} J_r(t_r) = J_e^0$ (6.7)

where J_e^0 is the recoverable compliance.

The response of the material is a function of the strain history. According to the Boltzmann superposition principle, assuming that the deformation imposed is within the linear viscoelastic region, the strain can be expressed as:

$$\gamma(t) = \int_{-\infty}^{t} J(t - t')d\tau(t') \quad (6.8)$$

For $0<t<t_1$, the creep compliance can be directly calculated from the measured strain:

$$\gamma(t) = J(t)\tau_0 \quad (6.9)$$

However, for $t_1<t$, the total strain of the material is the sum of the strains obtained during the creep and creep recovery experiments. The creep recovery occurring at $t=t_1$ is equivalent to a second creep experiment with a constant stress of $-\tau_0$:

$$\gamma(t) = J(t)\tau_0 + J(t - t_1)(-\tau_0) \quad (6.10)$$

Hence :

$$J(t) = \frac{\gamma(t)}{\tau_0} + J(t - t_1) \quad (6.11)$$

Considering that J(t) is known for $0<t<t_1$, the creep compliance function can be extended to $2t_1$ by the equation above. The procedure can be repeated to extend the creep compliance curve as many times as necessary until J(t) reaches steady-state and becomes linear with time.

The creep function can be expressed as a function of the continuous retardation spectrum L(τ).

$$\psi(t) = \int_{-\infty}^{\infty} L(\tau')\left(1 - e^{-\frac{t}{\tau'}}\right) dln\tau' \quad (6.12)$$

An alternative expression using the discrete retardation spectrum (τ_k, J_k) composed of the retardation times and strengths can be used.

$$\psi(t) = \sum_{k=1}^{N} J_k(1 - e^{-\frac{t}{\tau_k}}) \quad (6.13)$$

The calculation of the continuous spectrum from experimental J(t) data by using Eq. (6.12) is an ill-posed mathematical problem [167]. Kaschta and Schwarzl developed an algorithm to calculate the discrete retardation spectrum based on Eq. (6.13) [158]. In this work, the nonlinear regularization algorithm (NLREG) developed by Honerkamp and Weese [168] was used.

Once the discrete retardation spectrum determined, the real part and the imaginary part of the complex compliance can be calculated according to:

$$J'(\omega) = J_0 + \sum_{k=1}^{N} J_k \frac{1}{1+\omega^2\tau_k^2} \quad (6.14)$$

$$J''(\omega) = \frac{1}{\omega\eta_0} + \sum_{k=1}^{N} J_k \frac{\omega\tau_k}{1+\omega^2\tau_k^2} \quad (6.15)$$

Following this, the storage and loss moduli can be calculated according to:

$$G'(\omega) = \frac{J'(\omega)}{J'(\omega)^2 + J"(\omega)^2} \quad (6.16)$$

$$G"(\omega) = \frac{J"(\omega)}{J'(\omega)^2 + J"(\omega)^2} \quad (6.17)$$

This methodology has been used to obtain estimates of the moduli at frequency values that are normally not accessible through regular frequency sweeps [159-161,165,169].

Once the moduli have been calculated, the discrete relaxation spectrum (λ_k, G_k) can be obtained by fitting the G'(ω) and G"(ω) data according to the following equations:

$$G'(\omega) = \sum_{k=1}^{N} G_k \frac{(\omega\lambda_k)^2}{1+(\omega\lambda_k)^2} \quad (6.18)$$

$$G"(\omega) = \sum_{k=1}^{N} G_k \frac{\omega\lambda_k}{1+(\omega\lambda_k)^2} \quad (6.19)$$

G_k represents a relaxation strength (Pa) and λ_k a relaxation time (s).

6.3 Experimental

6.3.1 Materials

The EOC, trade name Engage 8130, density 0.864 g.cm^{-3}, MFI 13 g/10 min at 190°C, copolymer content 42 wt%, was obtained from Dow Chemical. The melting point, crystallinity and crystallization temperature of the EOC, as measured by DSC are respectively 67.1°C, 3.7% and 40°C. A maleated EOC (EOC-g-MA) Exxelor MDEX 95-2, density 0.830 g.cm^{-3}, MFI 7.5 g/10

min at 190°C, MA content 0.35 wt% was supplied by ExxonMobil. The melting point, crystallinity and temperature of crystallization of the EOC-g-MA are respectively 73.4°C, 15%, and 60.5°C.

Hydrophilic fumed silica (SiO_2) Aerosil® 200 with an average primary particle size of 12 nm and SSA of 200±25 m^2/g was supplied by Evonik Industries.

Toluene (99.8%) was purchased from Sigma-Aldrich and used as received.

6.3.2 Preparation of nanocomposites

Silica nanoparticles were dried at 200°C for 20 hrs prior to compounding. EOC was introduced first into a Haake PolyLab rheometer equipped with a Rheomix 610p mixing chamber and roller rotors and compounded at 120°C and 60 rpm for 2 min, which was sufficient for the torque to reach a steady value, signifying that the polymer had melted. The SiO_2 particles were introduced subsequently and compounded with the polymer for an additional 6 min. SiO_2 loadings were 2 and 5wt%, which corresponds respectively to 0.8 and 2vol%. When the EOC-g-MA compatibilizer was used, EOC and EOC-g-MA were dry-blended first according to a 90/10 EOC/EOC-g-MA weight ratio before being introduced into the Haake. The same compounding procedure as described above for the uncompatibilized materials was followed.

6.3.3 Characterization of nanocomposites

6.3.3.1 Bound polymer determination

The same technique as detailed in section 5.2.6 was used. The average of three measurements is reported. This procedure was only performed on composites containing 5wt% SiO_2, as lower loadings did not produce a measurable quantity of insoluble material.

6.3.3.2 Morphology

The state of dispersion of the fillers was assessed by TEM imaging, using an FEI Tecnai 20 instrument. Samples were compression molded using a Carver press at 150°C and 10 MPa for 1 min. Ultra-thin sections were prepared using a Leica ultra cryomicrotome.

6.3.3.3 Rheological characterization

Rheological characterization was carried out using a Reologica ViscoTech oscillatory rheometer equipped with 20 mm parallel plate fixtures under nitrogen purge. Compression molded disks of 20 mm diameter and 1 mm thick prepared in a similar manner as described above were made. All the rheological tests were carried out at 100°C.

Oscillatory Shear

The limits of linear viscoelasticity were determined by stress sweep experiments with stresses ranging from 1 to 10^4 Pa at 0.7 rad/s (0.1 Hz). Time sweeps, lasting for 5000 s were conducted at a 5% strain and 0.7 rad/s (0.1 Hz). SAOS measurements included stress-controlled frequency sweeps from 0.06 to 160 rad/s in the LVE region, which was determined from the stress sweeps.

Creep experiments

Creep experiments involved imposing a constant stress during a certain amount of time followed by recovery. In order to collect and interpret reliable creep and creep recovery data, it is important that a couple of conditions are satisfied.

Firstly, the stress applied during the creep phase must be small enough to guarantee that the deformation remains within the LVE region and large enough to ensure a good quality of the data. Extensive trials at various stresses revealed that 30 Pa and 40 Pa for the samples containing 5wt% SiO_2 and 2wt% SiO_2 respectively were sufficient to produce signal of good quality, while remaining in the linear region.

Secondly, the time during which the constant stress is applied must be long enough to allow the samples to reach steady-state, while ensuring that the strain remains within the LVE region. For the compatibilized composites, a strain of 1 was reached at about 800 s, whereas for the non-compatibilized samples containing 2wt% SiO_2, this limit was reached at 400 s. On the other hand, the non-compatibilized samples containing 5wt% SiO_2 suffered for strong time-dependency. Therefore it was decided to conduct incomplete creep according to the procedures described in [161-163].

The time for the recovery experiments was set so that the recoverable compliance had reached a steady value – in all cases a total experimental time of 1400 s was sufficient for this.

Following extensive experimentation, to identify the stress values that would provide good torque resolution, while not exceeding the limits of linear viscoelasticity, the parameters summarized in Table 6.1 were chosen.

Table 6.1 Details of creep followed by creep recovery measurements

Matrix	Silica loading (wt%)	Stress (Pa)	Creep Time (s)	Recovery Time (s)	Total Time (s)
EOC	2	40	400	1000	1400
EOC	5	30	100	1300	1400
EOC/EOC-g-MA	2	40	800	600	1400
EOC/EOC-g-MA	5	30	800	600	1400

The NLREG software developed by the Freibourg Materials Research Center version 1650 (2006) was used to determine the retardation spectra and the dynamic oscillatory properties of the samples based on creep and creep recovery data [170].

6.4 Results

6.4.1 Effect of compatibilization

6.4.1.1 Morphology

The effectiveness of the introduction of a compatibilizer can be seen when comparing the TEM images shown in Figure 6.2 (a) and (b) representing respectively EOC+SiO2 and EOC/EOC-g-MA+SiO2 at 5wt%. A drastic reduction of the size of the aggregates is observed when the compatibilized matrix is used. Introduction of the compatibilizer results in an improvement of the interfacial interactions between polymer and filler, through hydrogen bonding between the silanol groups located at the surface of the silica particles and the polymer matrix [171,172]. BdP evaluations can be used as an indication of P/F interactions [9]. These measurements confirm that

the amount of polymer bound on the surface of the particles in the compatibilized samples is substantially higher than that present in the non-compatibilized samples (1.1 as opposed to 0.29 grams of BdP per gram of SiO_2 respectively).

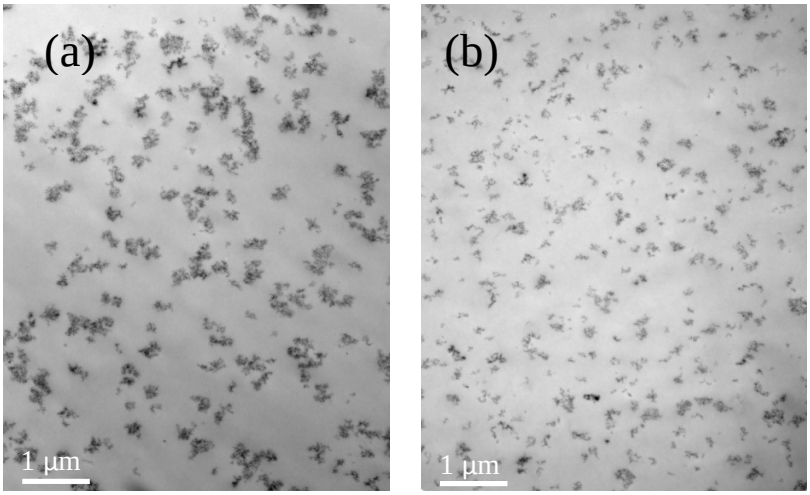

Figure 6.2 TEM images of non-compatibilized (a) and compatibilized (b) composites filled with 5wt% of SiO_2 particles.

The improved P/F interactions result in a greater capability for stress transfer from the polymer matrix to the particles during compounding, thus resulting in a finer state of dispersion. It should be noted that at the loadings under considerations the filler aggregates are not interconnected, thus avoiding the complications that arise in rheological evaluations stemming from the presence of a filler network composed of flocculated silica, as it was reported in Chapter 5.

6.4.1.2 Strain dependence

Figure 6.3 compares the strain dependence of the storage modulus, G' of the compatibilized and non-compatibilized composites filled with 5wt% of SiO_2 particles and the respective matrices. The EOC/EOC-g-MA matrix has higher values of the storage modulus, as well as complex viscosity, due to the higher viscosity of the EOC-g-MA.

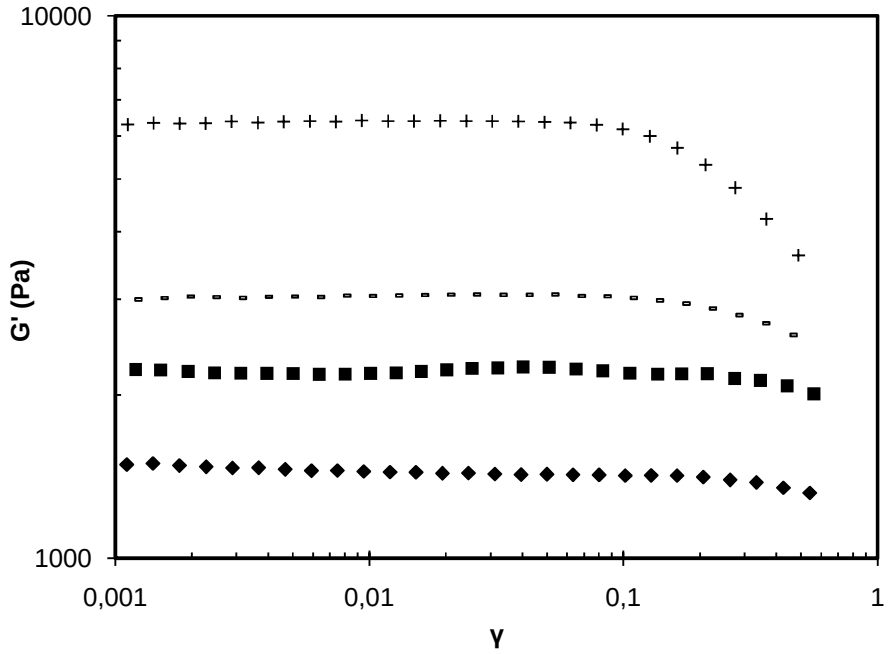

Figure 6.3 Strain-sweeps at 0.1 Hz, 100°C. The corresponding stresses ranged from 1 to 10^4 Pa. Symbols are: (◆) EOC, (■) EOC/EOC-g-MA, (+) EOC+SiO_2 5wt% (-) EOC/EOC-g-MA+SiO_2 5wt%.

The non-compatibilized composites are significantly more strain sensitive, displaying a critical strain of about 0.08 as opposed to 0.2 for the compatibilized samples. The "Payne" effect in filled rubbers is typically associated with a breakdown of the secondary network of particles [65]. In Chapter 5 it was suggested that in the absence of a network of filler particles this phenomenon is

driven by the strength of the P/F interactions. When interfacial interactions between filler and polymer are weak, debonding of the adsorbed chains takes place when a critical value of strain is reached. In the presence of strong interfacial interactions, the polymer chains are “anchored” to the surface of the filler, thus resisting debonding until higher values of strain are reached.

6.4.1.3 Time sweeps

The LVE properties of the EOC and EOC/EOC-g-MA matrices exhibit a steady behavior over 5000s, as shown in Figure 6.4.

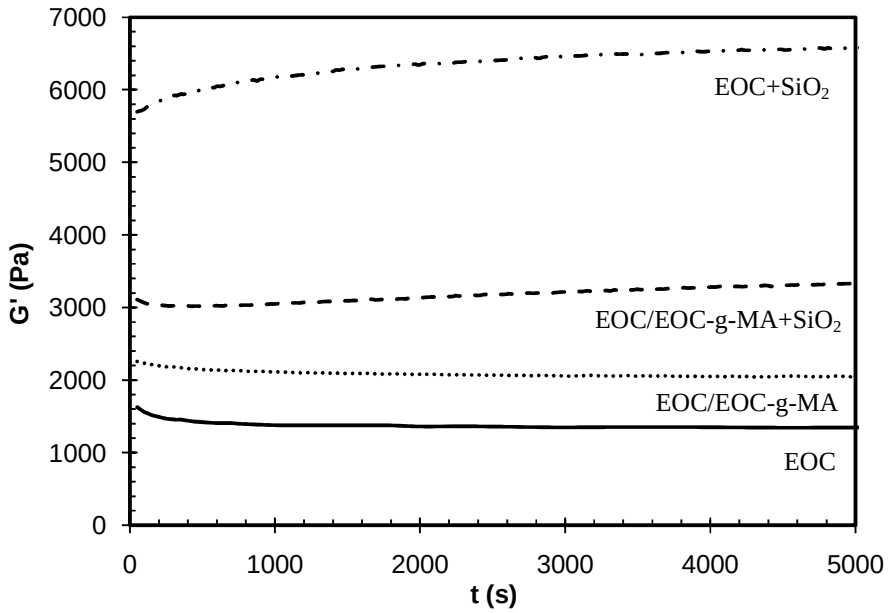

Figure 6.4 Time sweeps showing the evolution of the storage modulus as a function of time at 100°C under a 5% strain and 0.1Hz (0.7rad/s). SiO_2 loading is 5wt%.

The filled compatibilized samples show a very subtle increase whereas the filled non-compatibilized samples experience a significant increase of G' by about 15%. The increase in modulus is caused by the SiO_2 particle agglomeration during the time sweep, which can be clearly seen in TEM images of samples taken before and after the completion of the time sweep (Figure 6.5 (a) and (b) respectively).

On the contrary, the morphology of the compatibilized composites is stable (Figure 6.5 (c) and (d)). These findings confirm what was suggested in chapter 5 i.e. that improved P/F interactions promote stability by anchoring the particles to the matrix, thus preventing the particles from agglomerating during the time sweep.

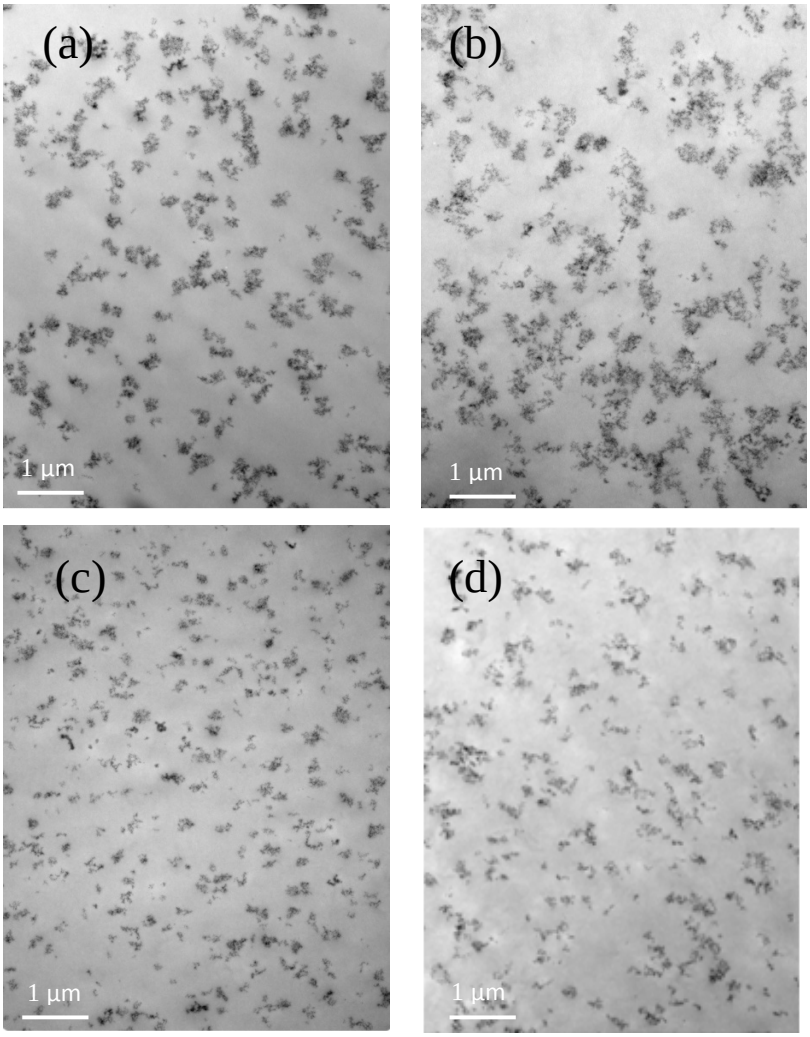

Figure 6.5 TEM images at 5wt% before and after a 5000s time sweep experiment, at 5wt% strain and 0.1 Hz. (a) EOC+SiO_2, before (b) EOC+ SiO_2 after, (c) EOC/EOC-g-MA+SiO_2 before, (d) EOC/EOC-g-MA+SiO_2 after.

A slight decrease is noted in the response of the matrices and the compatibilized composites during the first 200 s of the time sweep. Additionally, most of the modulus increase in the

EOC/EOC-g-MA composite takes place in the first 300 s. As a result, it was decided to wait 300 s before recording any rheological data in the subsequent evaluations.

6.4.2 Frequency sweeps and creep/recovery experiments

6.4.2.1 Compatibilized samples

Given the complications in rheological characterization arising from the strong time dependency of the non-compatibilized composites, we begin our investigations with the compatibilized samples. Frequency sweeps of the compatibilized composites at various SiO_2 loadings reveal minor differences between the matrix and composites (Figure 6.6).

The complex viscosity of the composites is slightly higher, which is characteristic of the hydrodynamic effect of the nanoparticles. The slope of the elastic modulus vs. frequency curve remains the same, even at a 5wt% loading.

It should be noted that based on the data shown in Figure 6.6, all samples display a slight deviation from terminal flow, as there is a slight deviation from the characteristic slope of 2 of the G'(ω) and the complex viscosity curve has not reached a plateau. This implies that at the rather low temperature used in this work (100°C), the time frame of the experiment does not allow the polymers and composites to fully relax [173].

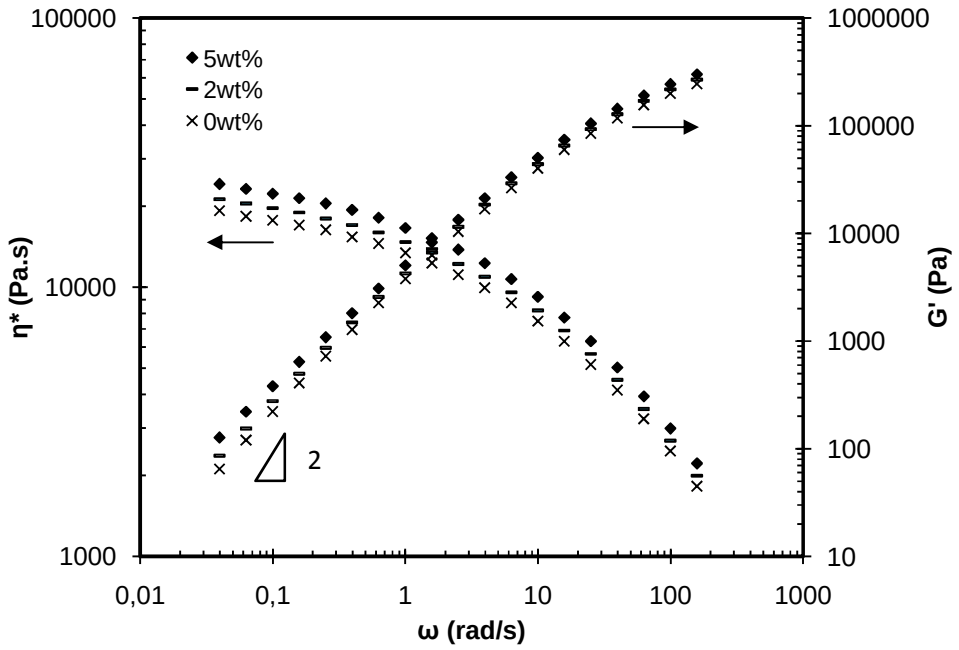

Figure 6.6 Dynamic material functions as a function of angular frequency for compatibilized composites filled with 0, 2 and 5wt% of SiO_2 particles.

SAOS measurements therefore are not sensitive enough and access to much lower frequencies (i.e. much longer times) would be required to differentiate between samples. However, accessing the terminal flow zone means being able to experimentally achieve frequencies lower than 0.001 rad/s, taking more than 6000s. This is not practically feasible, due to thermal degradation considerations. One way to achieve lower frequencies is via the TTS principle. However the use of TTS with filled materials is sometimes questionable [174].

Another way to get an insight into the long time behaviour is by conducting creep followed by creep recovery experiments, and combining the data obtained with the SAOS data to broaden the frequency range, as explained in section 6.2.

Figure 6.7 shows the J_c and J_r data from creep/recovery experiments.

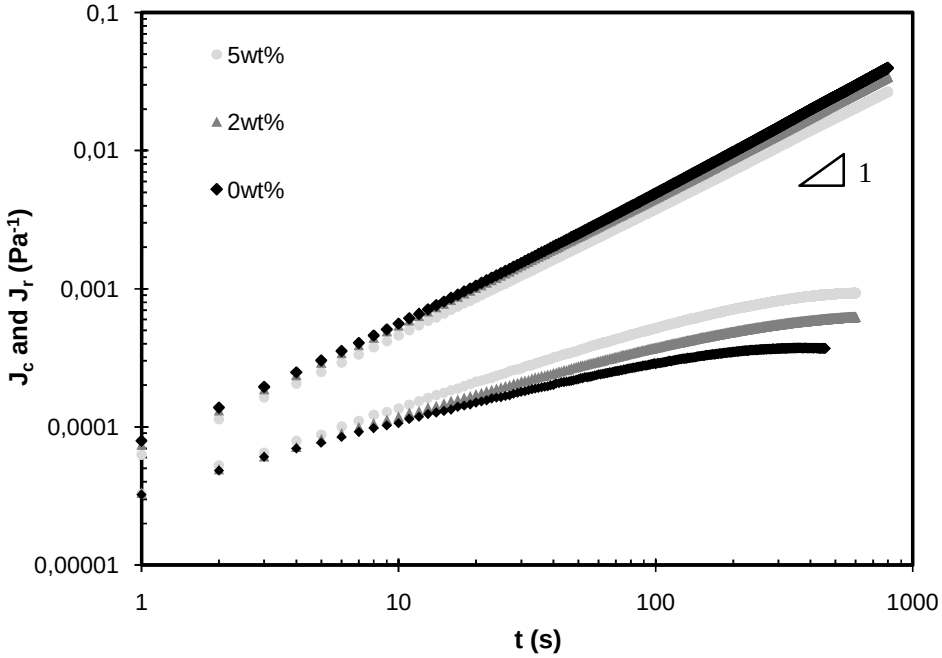

Figure 6.7 J_c (above) and J_r (below) data from creep/recovery experiments for compatibilized materials filled with 0, 2 and 5wt% of SiO_2 particles.

The data of the creep compliance confirm that the EOC/EOC-g-MA matrix reaches steady-state quite rapidly, as a slope of 1 is attained. There is no discernible difference between the matrix and the composite containing 2wt% SiO_2, whereas the composite containing 5wt% exhibits slightly lower values of the creep compliance, consistent with the results of Figure 6.6. A slight deviation from the slope of 1 is observed, which is typical of filled polymers at these loadings [165]. The recovery data show a trend of increasing J_r as the SiO_2 content increases.

It is interesting to note that the values of t/J(t) versus 1/t obtained from the creep experiments show perfect superposition with the SAOS data, when plotted together in a plot of the complex viscosity versus ω, as shown in Figure 6.8.

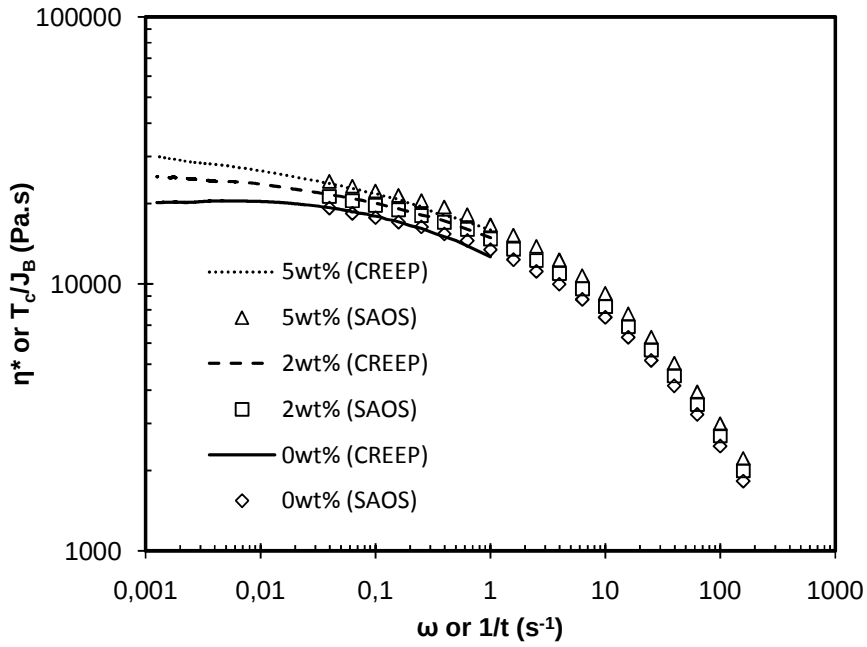

Figure 6.8 Superposition of data from SAOS experiments and creep/recovery experiments for compatibilized materials reinforced with 0, 2 and 5wt% of SiO_2 particles.

This suggests that creep and SAOS experiments can be used to complement each other, with SAOS being able to access the higher frequencies (short time scale), whereas creep being more suitable to characterize the viscoelastic properties at longer times (corresponding to lower freqency range). At smaller frequencies, the pure EOC/EOC-g-MA matrix clearly attains a plateau, suggesting that the terminal regime has been reached. However, the t/J values of the composites increase slightly, indicating that they have not reached true steady-state.

Given that extending the experimental creep time would lead into the non-linear region, the Boltzmann superposition principle was applied to the strain data to further extend the time scale accessible through the creep experiments, according to the procedure described in section 6.2.

Figure 6.9 presents the retardation spectra obtained using the combined creep and creep recovery data as inputs to the NLREG software and compares them to the spectra obtained from the SAOS data. The retardation spectra obtained from the two different sets of data agree well with each other and overlap in the time frame between 1 and 10 s.

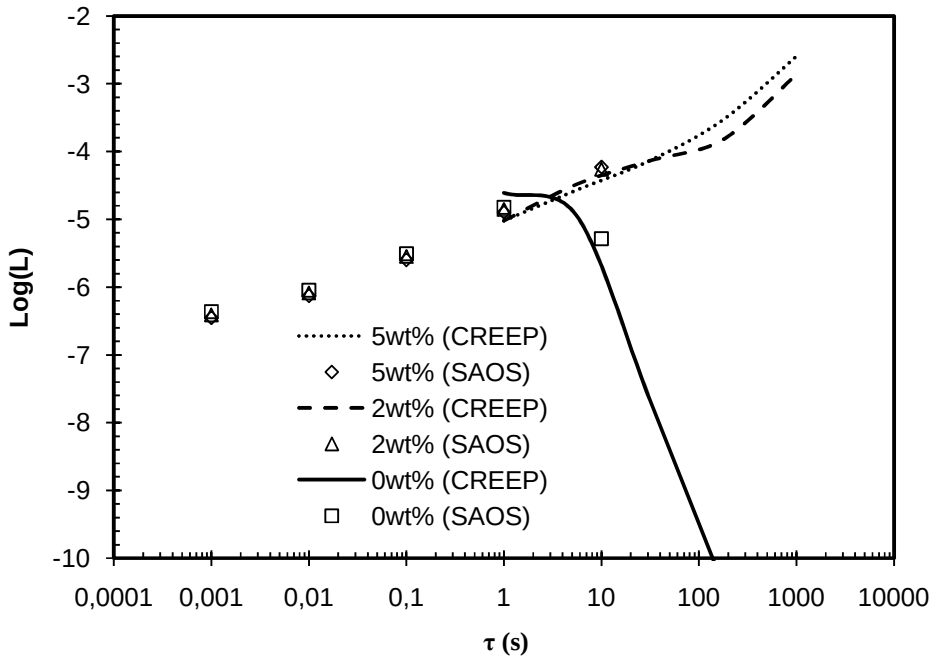

Figure 6.9 Retardation spectra of compatibilized materials reinforced with 0, 2, 5wt% of SiO_2 particles obtained from creep/recovery and oscillatory data processed with NLREG.

At retardation times above 10 s, the retardation strengths of the unfilled material drop, while the strengths of the filled composites continue to increase. Similar trends were obtained in the literature [163,165,175]. The increase in the retardation times, indicating increased rigidity of the composites has been explained in terms of lower mobility of the polymer chains and the presence of the nanoparticles [175]. Since there are no interactions between the particle aggregates, because of the large inter-aggregate distance, the effect seen here is most probably related to particle/molecule interactions [165].

Figure 6.10 displays the storage modulus as a function of frequency obtained from the retardation spectra using Eq. (6.16). Good superposition of the oscillatory and creep data is confirmed regardless of the silica loading. The curve of the storage modulus as a function of the angular frequency of the pure material exhibits a slope of 2 at the very low frequencies, indicating that by using the described approach the terminal flow zone has been reached. The difference in the storage modulus values of the matrix and the composites becomes clear at the lowest frequencies, with a secondary relaxation process taking place, revealing the effect of the nanoparticles on the motion of the macromolecules at long time scales.

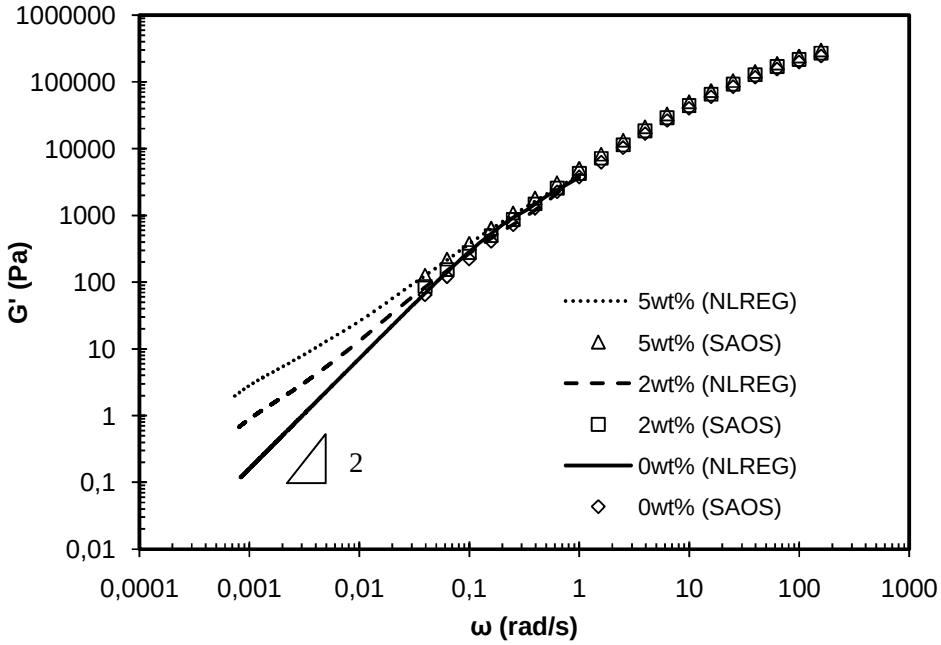

Figure 6.10 Storage modulus as a function of angular frequency for compatibilized materials filled with 0, 2, 5wt% of SiO_2 particles. Superposition of experimental SAOS data and NLREG results from creep and creep recovery data.

Given that P/F interactions seem to play an important role in the systems under consideration that contain low filler loadings, it is instructive to examine the EOC matrix, without the compatibilizer. The absence of hydrogen bonding capacity between polymer and filler would result into weaker P/F interactions, where the only possible mode would be physical adsorption of the filler onto the polymer surface. This analysis is presented in the following section.

6.4.2.2 Non-compatibilized samples

Figure 6.11shows the SAOS results for the non-compatibilized materials, filled with 0, 2 and 5wt% of SiO_2 silica particles.

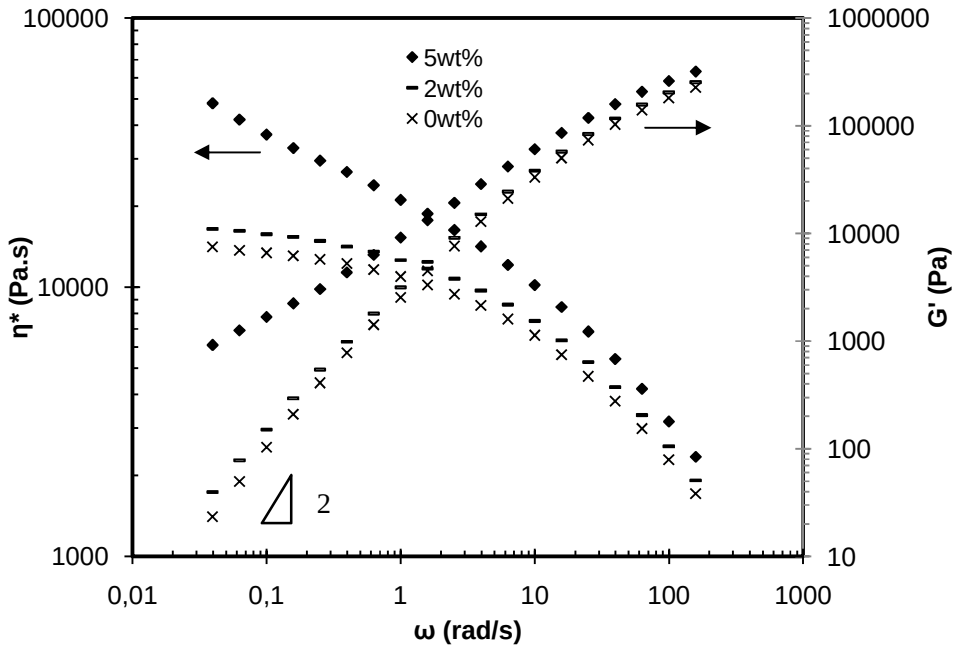

Figure 6.11 Dynamic functions as a function of angular frequency of non-compatibilized composites filled 0, 2 and 5wt% of SiO_2 particles.

Similarly to what was observed for the compatibilized composites, the addition of 2wt% SiO_2 led to a minor effect on both storage modulus and complex viscosity. However, at 5 wt%, the deviation is much more significant, and it not only affects the whole frequency range, but it is even more pronounced at low frequencies, where a yield stress and a secondary plateau begin to emerge.

Given the slight difference in the viscosities of the matrices (the compatibilized matrix has a zero shear viscosity of $2.04 \cdot 10^4$ vs. $1.77 \cdot 10^4$ Pa.s for the non-compatibilized matrix), it is more instructive to compare the ratio of the complex viscosity of the composites and the viscosity of the respective matrices, as shown in Figure 6.12.

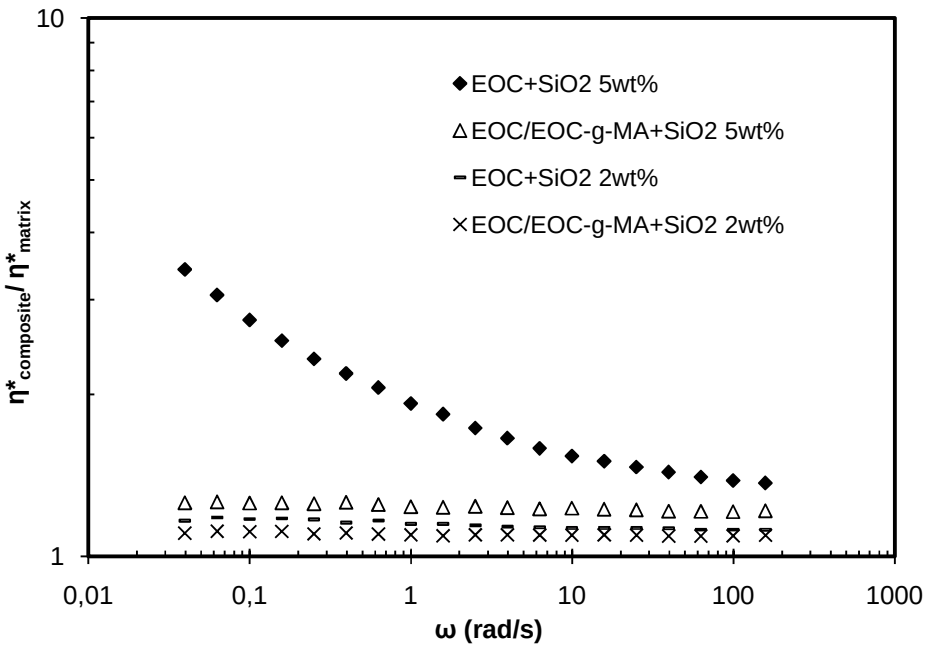

Figure 6.12 Normalized complex viscosities with respect to the matrix for compatibilized and non-compatibilized samples filled with 2 and 5wt% of SiO_2 particles.

Given that the type of particles remains the same, this difference must be attributed to the different type of P/F interactions that are established in this system, which in turn influence the dispersion of the SiO_2, as discussed in section 6.4.1.1.

Figure 6.13 shows the creep compliance data for non-compatibilized composites filled with 0, 2 and 5wt% of SiO_2 particles. The composites containing 5wt% SiO_2 do not reach steady-state. This can be explained by the pronounced time-dependent behaviour of the samples reported earlier in Figure 6.4, which is due to their tendency for agglomeration.

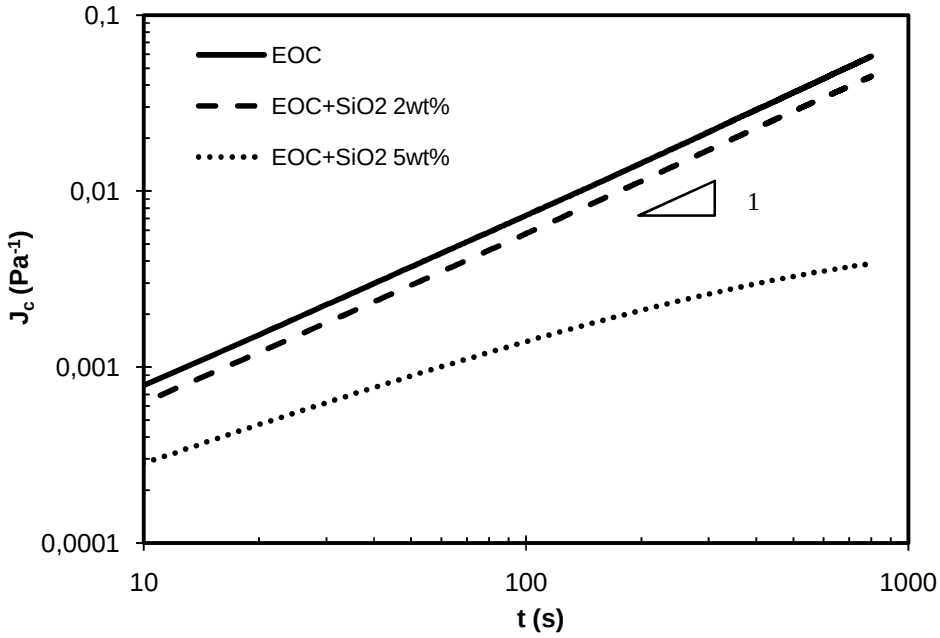

Figure 6.13 Creep compliance data of different materials at 100°C and 30Pa.

Given the inability to reach long creep times, incomplete creep experiments were conducted up to 100 s, and the Boltzmann superposition principle were used in order to extend the frequency range available by combining SAOS and creep/recovery data. The dynamic oscillatory functions as a function of the angular frequency inferred from NLREG calculations are shown in Figure 6.14.

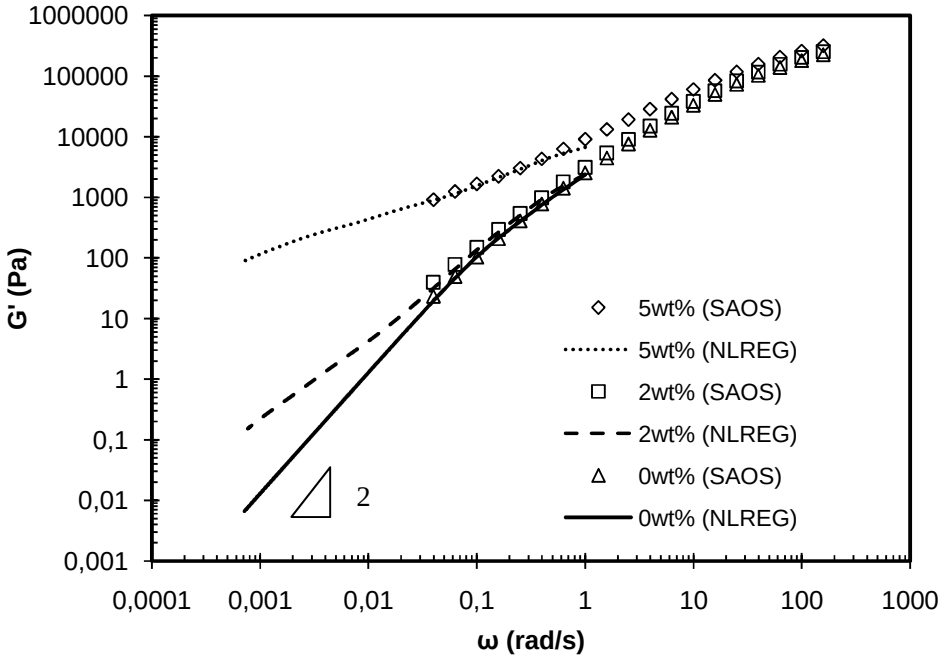

Figure 6.14 Storage modulus as a function of angular frequency for non-compatibilized composites filled with 0, 2, 5wt% of SiO_2 particles. Superposition of experimental SAOS data and NLREG results from creep and creep recovery data.

The NLREG data overlap very well with the SAOS data in the 0.04 – 1 rad/s frequency range. A deviation from the response of the pure matrix can now be readily seen for the 2wt% silica-containing sample as shown in Figure 6.14. Figure 6.15 presents the weighted relaxation spectra of both compatibilized and non-compatibilized samples.

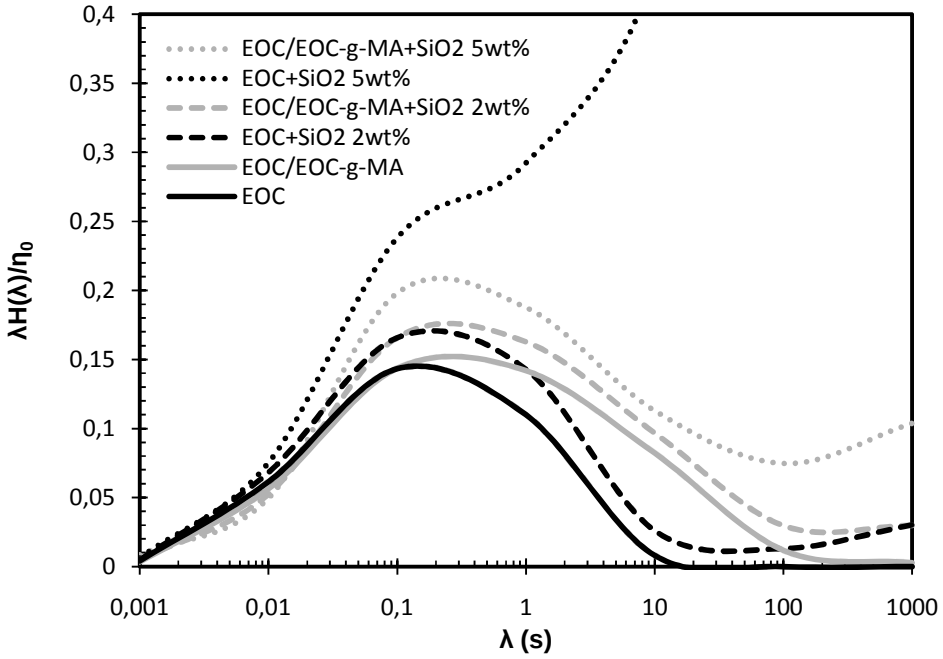

Figure 6.15 Weighted relaxation spectra for compatibilized and non-compatibilized samples at 0, 2 and 5wt% SiO_2 loadings with respect to the zero-shear viscosity of their respective matrix; obtained for the combination of SAOS and creep experiments.

The normalized values are used to account for the difference of viscosity between the matrices. The effects of SiO_2 concentration and compatibilizer can be seen: regardless of the matrix, as the SiO_2 concentration increases, the normalized relaxation strengths do too, indicating the presence of a secondary relaxation process. Additionally, the more silica in the composite, the earlier the onset of the additional relaxation.

For a given SiO_2 concentration, non-compatibilized samples show a much greater value in their relaxation strengths than their compatibilized counterparts, indicating a reduced chain mobility due to the poorer dispersion of the particles. This is especially pronounced for the non-compatibilized sample containing 5wt% SiO_2.

6.5 Discussion

In this study, composites containing low amounts of nanosilica were investigated. The rheological responses recorded depended on the nature of the P/F interactions. The presence of P/F interactions was confirmed by higher amounts of BdP present in the compatibilized samples. As a result, particle dispersion was found to be much finer for compatibilized composites, as TEM images revealed. This finding is attributed to the lowering of the interfacial tension at the particle/polymer interface, due to the presence of the P/F interactions, which facilitates the wetting of the particles by the polymer matrix.

The existence of physical contacts, resulting in an anchoring of the polymer chains on the filler surface may explain the ability of the compatibilized samples to resist to high strains (Figure 6.3). The important effect of aggregation is striking from the time sweep experiments, which clearly show that modulus increases as a function of time as the particles have an increased propensity to aggregate (Figure 6.4). This tendency is obviously an outcome of the absence of interactions between polymer and filler in the non-compatibilized samples.

In the non-compatibilized composites, particles are free to interact and therefore to aggregate, a process that is facilitated upon application of shear, since the probability of the particles to collide increases. Compatibilized samples have a layer of bound polymer surrounding the particles. This layer breaks up the F/F interactions by reducing the ability of the silanol groups located at the surface of the nanosilica to associate via hydrogen bonding. In SAOS experiments, the non-compatibilized samples exhibit larger increases in the viscoelastic properties compared to their compatibilized counterparts. At the low SiO_2 loadings used in this work, differences are hard to detect, therefore an extension of the time scale through a combination of SAOS and creep/creep recovery experiments is necessary. This technique proved to be valuable in differentiating

between the responses, especially in cases where the strong time dependency precludes reliable measurements using conventional SAOS experiments. The compatibilized samples appeared in a less aggregated state, therefore leading to a smaller increase of G', due to a reduced hyrodynamic effect, as opposed to their non-compatibilized counterparts.

These results are consistent with the findings of Chapter 5 where composites with weak physical interactions between the matrix and the surface of the particles were more prone to the formation of flocculated clusters, leading to network formation at lower filler loadings and to higher values of the viscoelastic material functions. In the present work, where the formation of a network is avoided, it is clear that the observed enhancements in the LVE properties have their origins in the formation of larger nanosilica aggregates.

6.6 Conclusions

EOC composites containing low amounts of SiO_2 were investigated in the presence and absence of a maleated EOC-g-MA compatibilizer. Compatibilized composites were characterized by a higher amount of polymer bound to the nanoparticles, and a finer state of dispersion compared to their non-compatibilized counterparts, due to the improved P/F interactions. Enhanced P/F interactions also stabilized the morphology, resulting in stable rheological responses. The compatibilized samples had greater critical strain for the onset of non-linearity compared to their non-compatibilized counterparts.

Compatibilized samples did not show deviations from terminal flow and displayed miminal increases in the dynamic oscillatory properties as a function of SiO_2 loading over the entire range of frequencies. This chapter introduced a technique that enables the extension of the SAOS data to lower frequencies (longer time scales) by superposing them with the retardation spectra

obtained from creep/creep recovery experiments. By using this technique it was possible to differentiate clearly the enhancement in the low frequency moduli as a function of filler loading. Non-compatibilized samples showed siginifcant deviations from the matrix response at a 5 wt% SiO_2 content. This was attributed to the presence of aggregated particles. Given the inability to conduct creep experiments at times sufficient to reach steady-state due to the pronounced time dependency, incomplete creep experiments were conducted in conjunction with creep recovery. Applications of these techniques showed that in spite of the time dependency and strain sensitivity, rheology in the linear region provides a useful tool to differentiate the morphology of these composites and thus to provide information about the extent of P/F and F/F interactions.

Chapter 7

INFLUENCE OF SPECIFIC SURFACE AREA AND COMPATIBILIZATION ON THE MORPHOLOGY AND VISCOELASTIC PROPERTIES OF ETHYLENE-OCTENE COPOLYMER/NANOSILICA COMPOSITES

7.1 Introduction

In Chapter 6, the effects of the presence of compatibilization and nanosilica content on the morphology and viscoelastic properties of EOC/SiO_2 nanocomposites were investigated over a broad range of frequencies. The altered P/F interactions induced by compatibilization led to distinctly different responses under shear deformation.

The degree of P/F and F/F interactions can be also altered by changing the SSA of the nanoparticles. The SSA, measured by the BET technique [32], is a well-known characteristic of solid particles. Szekeres et al. [176] confirmed that the SSA measured with the BET technique reflects well the surface chemistry of the particles, in particular the total surface silanol group concentration, which provides accurate indications on the surface area available for interaction with the hosting polymer chains. As a result, by increasing the SSA it should be possible to obtain higher degrees of P/F interactions due to physical adsorption, as well as more F/F interactions due to the increased potential for hydrogen bonding.

Several authors examined the effects of the SSA of silica particles on the amount of bound polymer [177,178], the glass transition temperature [179], the rate of degradation [177], the

morphology [178,180,181], the mechanical [177,178,181], thermal [179] and viscoelastic [179,180] properties of the composites based on rubber [177,181,182], polyurethane [179] and thermoplastic [180] matrices.

Parent et al. [177] and Wang et al. [178] reported contradictory results about the correlation between the SSA of the particles and the amount of bound polymer, highlighting the competition between the two phenomena mentioned above: an increasing number of silanol groups offers greater possibilities for chain adsorption, leading to higher amounts of BdP while at the same time enhancing the propensity for filler association through hydrogen bonding, thus promoting agglomeration.

Camenzind et al. [181] observed in PDMS/SiO_2 systems that particles with higher SSAs formed bigger aggregates, because of the larger surface area available for F/F interactions. On the contrary, Dorigato et al. [180] found in LLDPE/SiO_2 systems no significant differences in the state of dispersion between a precipitated silica having a SSA of 160 m^2/g and a fumed silica with a SSA of 380 m^2/g.

Regarding the dynamic oscillatory behaviour of the nanocomposites, Jauregui-Beloqui et al. [179] reported on polyurethane/SiO_2 composites during frequency sweep experiments an increase of both the storage and loss moduli at low frequencies up to an SSA of 200 m^2/g after which no increase took place. They explained this phenomenon by the enhancement of the fumed silica-polyurethane interactions. On the contrary, Dorigato et al. [180] did not detect any differences in the dynamic oscillatory behavior of LLDPE/SiO_2 nanocomposites filled with particles having SSAs of 200 and 380 m^2/g at both low and high frequencies.

The strong discrepancies in the studies mentioned above highlight the difficulty to generalize conclusions about the effects of the SSA of the particles, as the results may vary depending on the

type of silica (fumed/precipitated), its surface chemistry (presence/absence of functional groups), the nature of the matrix (polar/non-polar), and the silica concentration (below/above the percolation threshold).

In this study we investigate the morphology and viscoelastic properties of nanocomposites containing fumed silicas having a wide range of SSAs, from 150 to 380 m^2/g embedded in a non-polar thermoplastic matrix at concentrations much lower than the percolation threshold.

7.2 Experimental

7.2.1 Materials

The EOC, trade name Engage 8130, density 0.864 $g.cm^{-3}$, MFI 13 g/10 min at 190°C, copolymer content 42 wt%, was obtained from Dow Chemical. The melting point, crystallinity and temperature of crystallisation of the EOC, as measured by DSC are respectively 67.1°C, 3.7% and 40°C. The maleated EOC (EOC-g-MA) trade name Exxelor MDEX 95-2, density 0.830 $g.cm^{-3}$, MFI 7.5 g/10 min at 190°C, MA content 0.35 wt% was obtained from ExxonMobil. The melting point, crystallinity and temperature of crystallisation of the EOC-g-MA are respectively 73.4°C, 15%, and 60.5°C. The characteristics of the four different types of hydrophilic silica particles supplied by Evonik Industries are detailed in Table 7.1. Toluene (99.8%) and dicumyl peroxide (DCP, 98%) were purchased from Sigma-Aldrich and used as received.

Table 7.1 Physical characteristics of the silica nanoparticles.

Particles	Code	SSA (BET) (m^2/g)
Aerosil® 150	R150	150±15
Aerosil® 200	R200	200±25
Aerosil® 300	R300	300±30
Aerosil® 380	R380	380±30

7.2.2 Preparation of nanocomposites

Silica nanoparticles were dried at 200°C for 20 hrs prior to compounding. EOC was introduced first into a Haake PolyLab rheometer equipped with a Rheomix 610p mixing chamber and roller rotors at 120°C, 60 rpm. After 2 minutes when the torque had reached a constant value and the polymer had molten, the silica particles were introduced to reach a final compounding time of 8 minutes. Silica loadings were 2 and 5wt% which corresponds respectively to 0.8 and 2 vol%. When the EOC-g-MA compatibilizer was used, EOC and EOC-g-MA were dry-blended first according to a 90/10 EOC/EOC-g-MA weight ratio before being introduced into the Haake. The same compounding procedure as described above for the uncompatibilized materials was followed.

7.2.3 Characterization of nanocomposites

The techniques of characterization for the determination of the amount of bound polymer, the morphology, and the rheological properties were the same as the ones used in Chapter 6.

7.2.3.1 Mechanical testing

Cross-linked samples were prepared for mechanical testing. The components were dry-blended first and then mixed in the Haake with 0.5wt% DCP at 120°C, 60RPM, 8min, and then chopped into small pieces. The pieces were then compression-moulded under a Carver hot press at 180°C and 10 MPa for 5 min to make a 1.5mm-thick sheet. Dog-bone shaped specimens were cut out from the sheet with a type V die according to ASTM D638.

Tensile properties were measured using an Instron 3369 universal tester, at a crosshead speed of 500 mm/min. 7 specimens were tested per material, the highest and lowest values were removed and the average value was reported. The Young's modulus and the stress reached at a 500% strain are reported.

7.3 Results

7.3.1 Effect of SSA on the amount of bound polymer

The results of the bound polymer measurements on the 5wt% silica containing composites are presented in Figure 7.1. BdP measurements can provide a measure of the amount of polymer that is physically attached to the SiO_2 particles, and thus provide an indication of the degree of P/F interactions [9].

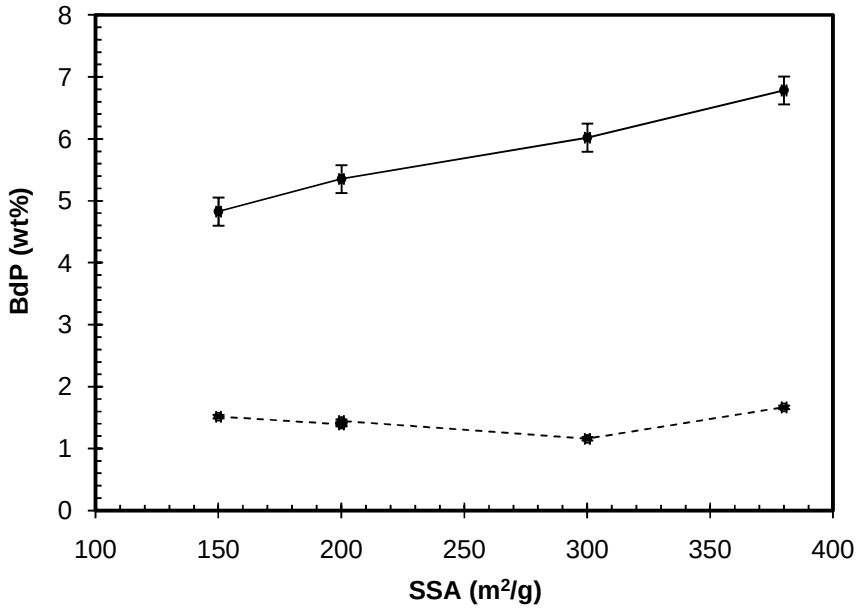

Figure 7.1 Amount of bound polymer as a function of the SSA for the 5wt% silica containing composites. Full line is with compatibilizer, dashed line is without compatibilizer.

First of all, in the presence of the EOC-g-MA compatibilizer the amount of BdP is significantly higher, suggesting stronger P/F interactions, which stem from hydrogen bonding between the silanol groups present at the surface of the particles and the succinic anhydride groups. The effect of hydrogen bonding becomes more pronounced as the SSA of the particles increases. Particles with a higher SSA offer a greater amount of hydroxyl groups that can potentially interact with the succinic anhydride groups of the EOC-g-MA, resulting in more polymer chains adsorbed on the particles surface and therefore in higher BdP amounts [177,178,182].

However, no influence of the SSA was noticed in the non-compatibilized samples, the amount of BdP remaining constant and representing only the amount of polymer that is physically adsorbed on the surface of the particles.

7.3.2 Effect of SSA on morphology

The effects of the SSA on the state of dispersion can be seen when comparing Figure 7.2 (a) and (b), representing respectively EOC+R150 and EOC+R380 at 5wt%.

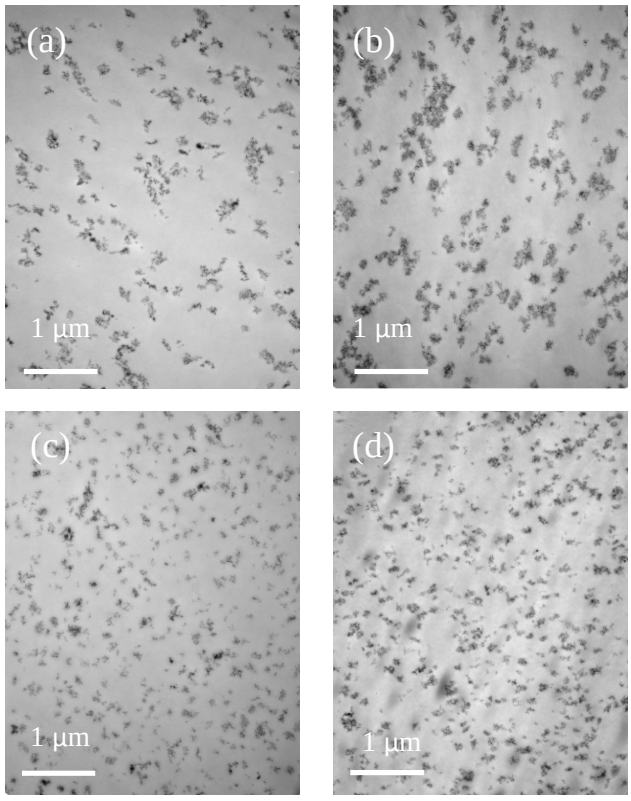

Figure 7.2 TEM images at 5wt%. (a) EOC+R150 (b) EOC+R380 (c) EOC/EOC-g-MA+R150 (d) EOC/EOC-g-MA+R380.

The R380 particles form bigger aggregates than their R150 counterparts. This can be explained by the fact that R380 particles, due to their higher SSA, possess a greater surface available per unit of weight and can potentially associate more readily due to increased F/F interactions. As a

result, particles with a high SSA are more prone to aggregation, as it can be seen on the TEM image of Figure 7.2 (b).

For a given SSA, the compatibilized composites (Figure 7.2 (c) and (d)) show a significant improvement in the state of dispersion of the nanoparticles. Indeed, the aggregates are much smaller, more spherical and with a shorter interparticle distance between them compared to their non-compatibilized counterparts (Figure 7.2 (a) and (b)). Obviously this improvement is attributed to the presence of stronger interactions between the succinic anhydride groups and the silanol groups through hydrogen bonding. The effect of the SSA on the morphology of the compatibilized composites is not as pronounced as in the non-compatibilized materials: only a slight increase of the size of the aggregates is observed in the composites filled with R380 compared to R150, but still showing a significant improvement compared to the non-compatibilized samples.

7.3.3 Effect of SSA on rheology

7.3.3.1 Stress Sweeps

Figure 7.3 presents the strain dependence of both compatibilized and non-compatibilized samples filled with R150 and R380 particles.

As reported previously in Chapter 6 the compatibilized samples exhibit a higher resistance to strain, but there is no obvious trend relating the SSA to the critical strain. The modulus appears slightly enhanced for the particles with higher SSA. The major effect once again here is that the non-compatibilized samples have significantly higher modulus values.

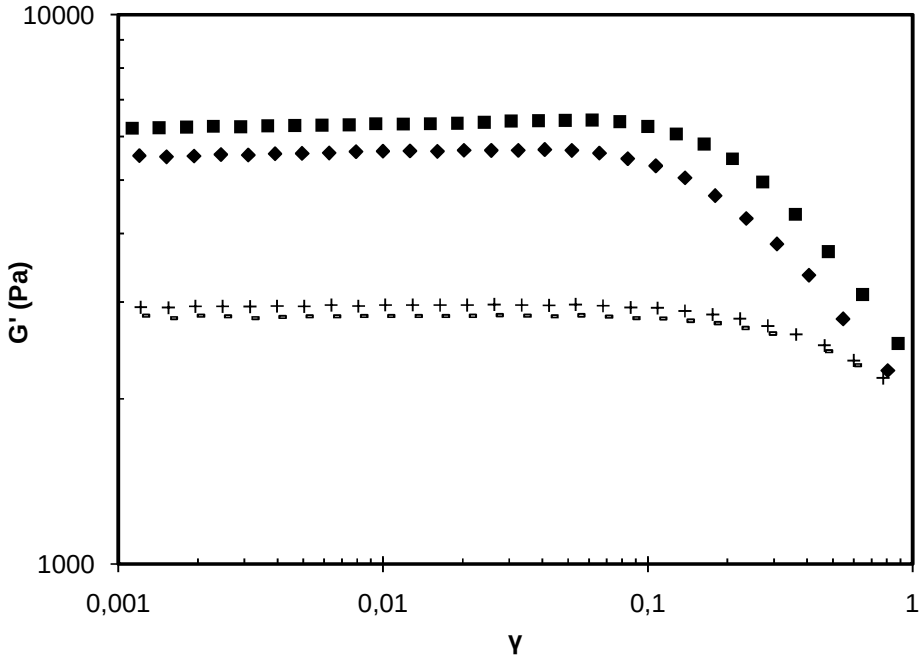

Figure 7.3 Strain-sweeps at 0.1 Hz, 100°C. The corresponding stresses ranged from 1 to 10^4 Pa. Silica loading is 5wt%. Symbols are: (◆) EOC+R150, (■) EOC+R380, (-) EOC/EOC-g-MA+R150, (+) EOC/EOC-g-MA+R380.

7.3.3.2 Time Sweeps

In the previous chapter we reported that the viscoelastic functions of the non-compatibilized samples displayed strong time dependency. This was associated to their increased propensity for aggregation, as shown in Figure 6.4. Additionally, the SSA of the particles affects the rate of growth of the viscoelastic functions: it can be seen on Figure 7.4 that in non-compatibilized materials, the storage modulus of the R380 particles shows a higher rate of growth compared to the R200 particles, suggesting that they are more prone to aggregation. This is due to their higher ability to engage F/F interactions as the surface area that is available for the formation of hydrogen bonds increases.

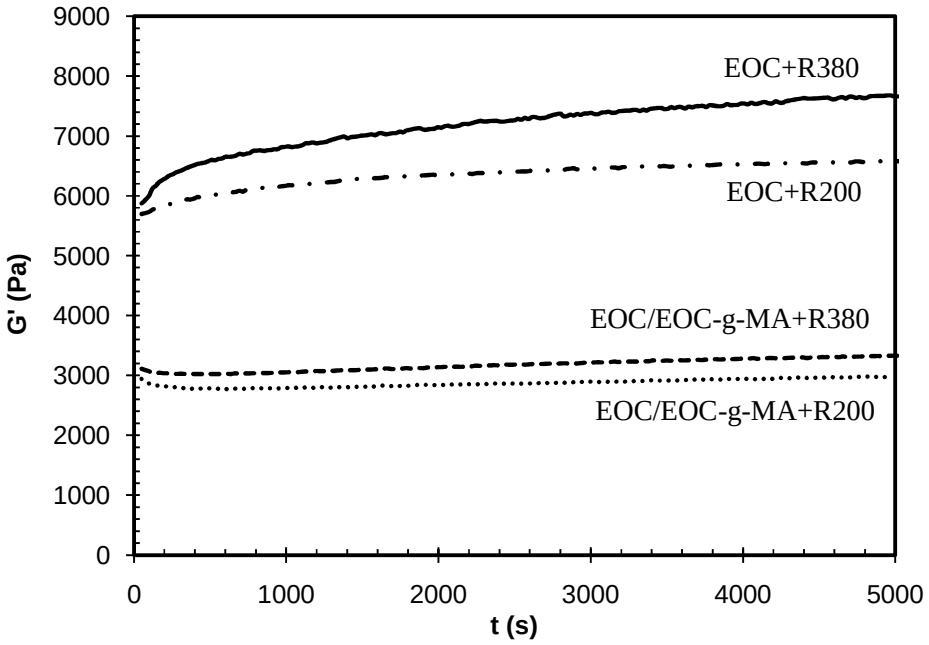

Figure 7.4 Time dependence of the viscosity η*(t) at 100°C under a 5% strain and 0.1Hz (0.7 rad/s). Silica concentration is 5wt%.

However, in compatibilized materials, no difference is seen between R200 and R380 particles. The stability of the samples in the presence of a compatibilizer is supported by the high amounts of BdP, which results in a formation of a layer of polymer surrounding the particles, thus preventing them from aggregating, irrespective of their SSA.

7.3.4 Frequency sweeps and creep/recovery experiments

7.3.4.1 Non-compatibilized samples

Figure 7.5 shows the SAOS measurements of the non-compatibilized samples containing 2wt% SiO_2. Irrespective of their SSA, there is no statistically significant difference among the samples, at this concentration.

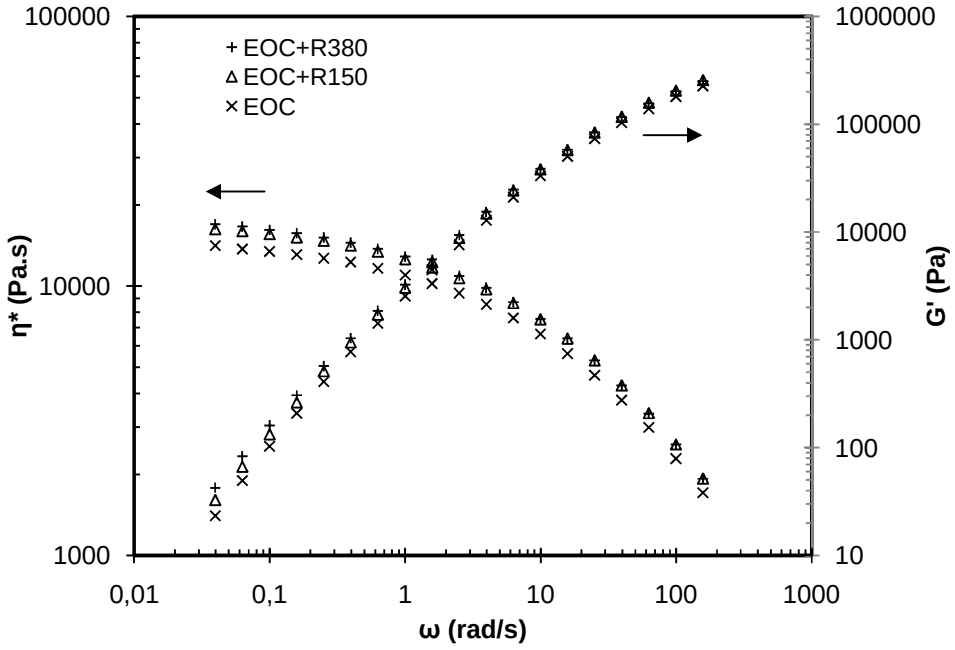

Figure 7.5 Dynamic material functions as a function of angular frequency for non-compatibilized composites filled with 2wt% of R150 and R380 particles.

As shown in Chapter 5, creep recovery experiments can provide a very sensitive means of differentiating between samples. The data of the creep and creep recovery compliances are shown in Figure 7.6. As it can be seen on the creep compliance curves, a slope of 1 is achieved for all

the samples, which is indicative of steady-state. The recovery curves however show remarkable differences between the samples. During recovery the pure EOC matrix reaches an equilibrium recoverable compliance J_e^0 much faster than the filled composites (200s for EOC vs. 500s for the filled materials). As a result, it can be concluded that nanoparticles tend to delay the creep recovery process. Moreover, the composites display significantly higher values of J_e^0 than the unfilled matrix and increasing the SSA of the particles leads to higher values of J_e^0.

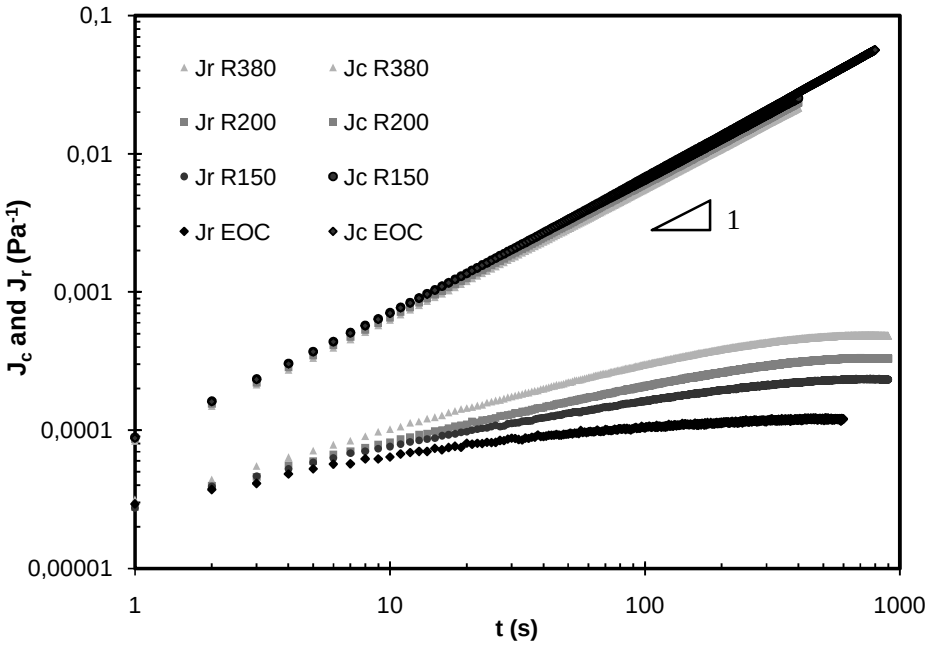

Figure 7.6 Raw J_c and J_r data from creep/recovery experiments for non-compatibilized materials filled with 2wt% of silica particles. R300 was removed for clarity.

Even though the frequency sweeps of Figure 7.5 showed very little difference between the types of particles used, it is possible to reveal a trend by extending the time scale of the measurement

according to the method described in section 6.2. The strain data recorded during creep and creep recovery were transformed into a creep compliance curve by using the Boltzmann superposition principle. The creep compliance data obtained were then processed with NLREG to calculate the G'(ω) dependence for the non-compatibilized composites at a 5wt% silica loading, as presented in Figure 7.7.

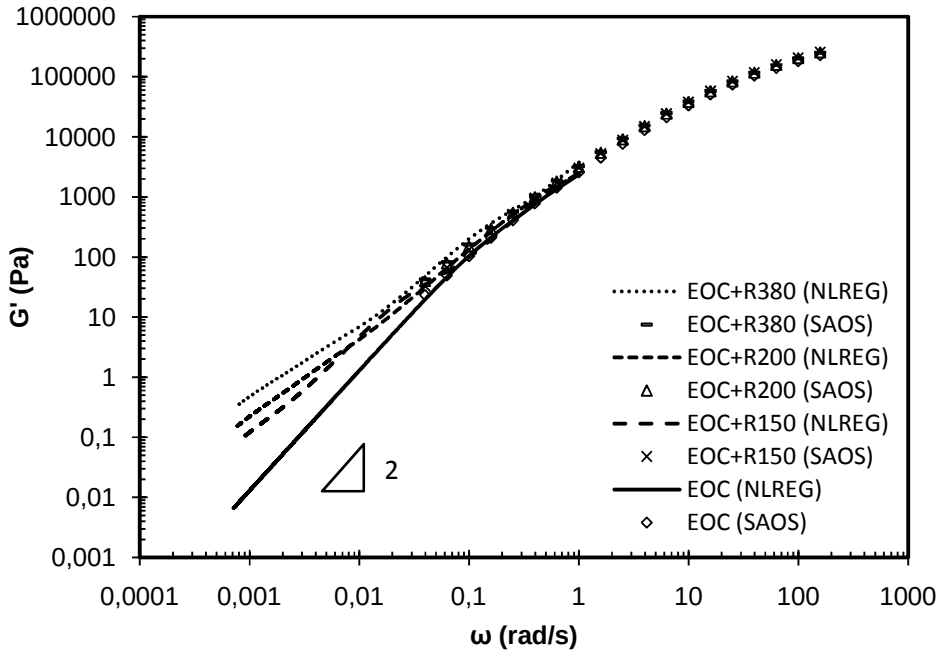

Figure 7.7 Storage modulus as a function of angular frequency for non-compatibilized materials filled with 2wt% of R150, R200 and R380 particles. Superposition of experimental SAOS data and NLREG results from creep and creep recovery data.

By using this approach, it becomes obvious that particles having a higher SSA induce a larger increase in the G' values in the low frequency range.

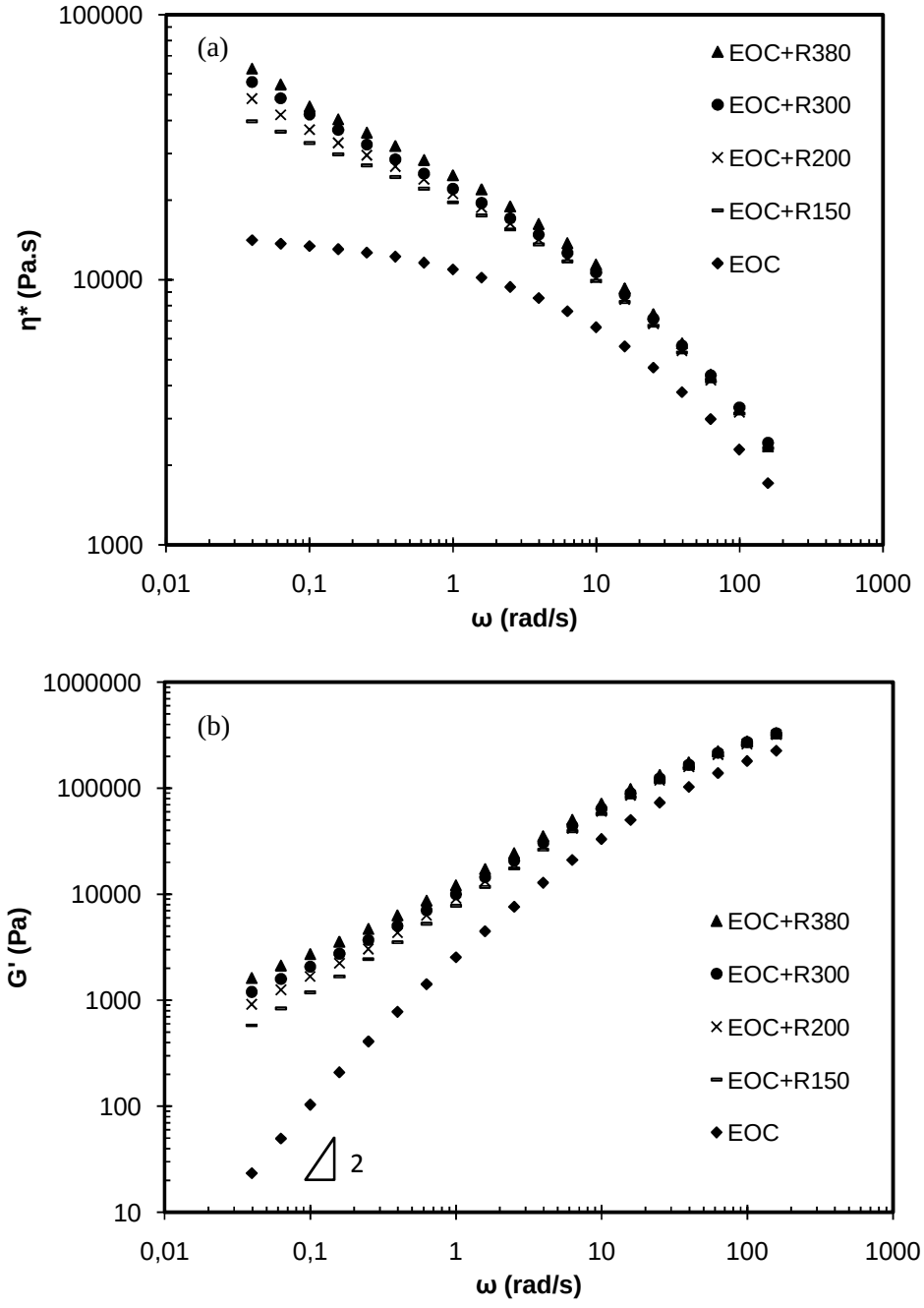

Figure 7.8 Dynamic material functions as a function of angular frequency for non-compatibilized composites at a 5wt% loading. (a) Complex viscosity, (b) Storage modulus.

The effect of the nanoparticles in the SAOS experiments throughout the frequency range becomes more evident as the filler content increases, as demonstrated in Figure 7.8, which presents the results of the SAOS measurements in terms of storage modulus and complex viscosity as a function of the angular frequency at a 5wt% silica concentration.

As expected, all the composites exhibit a strong deviation from the unfilled material, which is even more pronounced at low frequencies. As shown in Figure 7.8 (a) and Figure 7.8 (b) there is no Newtonian plateau regardless and the slope of the storage modulus at low frequencies remains higher than 2, which is characteristic of the terminal flow zone. Additionally, a small difference can be observed amongst the samples according to their SSA. There is a slight trend, suggesting that composites filled with particles with higher SSAs experience more pronounced increases in the storage modulus and complex viscosity at low frequencies, similarly to what was observed at the 2wt% composition. These differences can be seen better when the SAOS results are combined with the creep/recovery data, as shown in Figure 7.9.

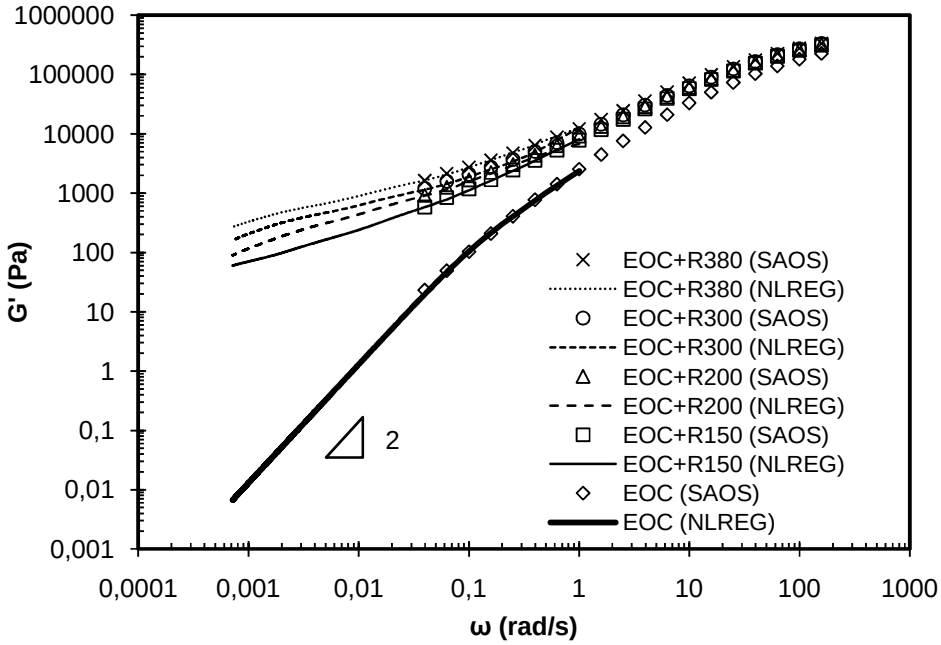

Figure 7.9 Storage modulus as a function of angular frequency for non-compatibilized materials filled with 5wt% of silica particles. Superposition of experimental SAOS data and NLREG results from *incomplete* creep and recovery data.

It should be noted that due to the higher silica concentration (5wt%) and the time dependence observed in the non-compatibilized samples (see Figure 7.4), only *incomplete* creep experiments could be conducted for a total of 100 s, followed by creep recovery, as explained in detail in Chapter 6. Similarly to what was observed at 2wt%, particles having a higher SSA induce a larger increase in the G' values. The trend described above can be explained by the TEM images of Figure 7.2, as it was observed that in non-compatibilized composites higher SSAs generally led to increased nanoparticle aggregation.

7.3.4.2 Compatibilized samples

Figure 7.10 depicts the dynamic oscillatory behavior of the compatibilized composites filled with particles having different SSAs.

Similarly to the results of Figure 7.5, the deviation from the properties of the unfilled matrix is very small for the compatibilized composites. Additionally, no trend with respect to the SSA can be seen.

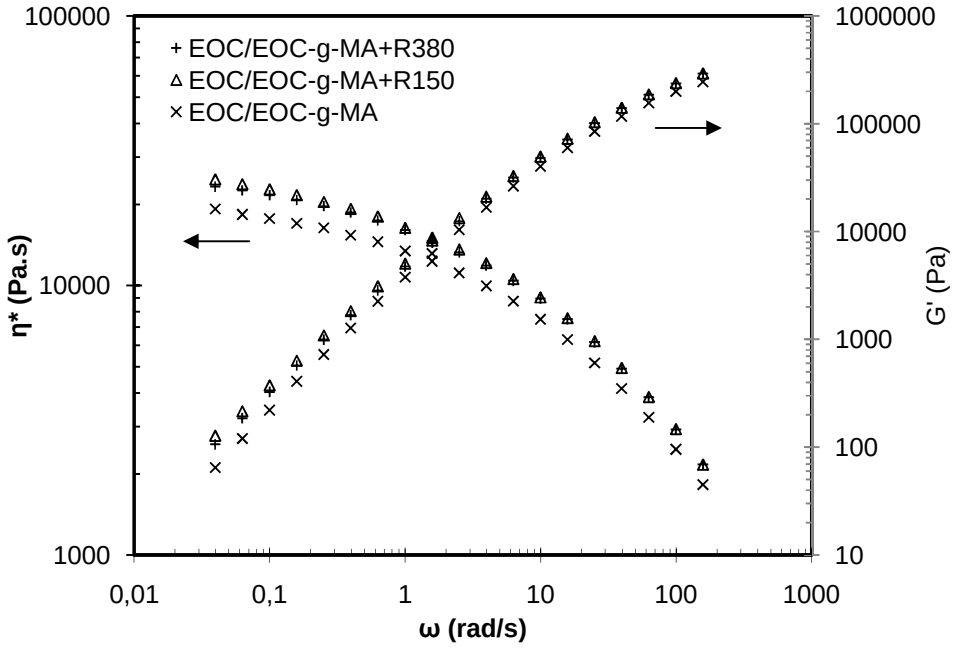

Figure 7.10 Dynamic material functions as a function of angular frequency for compatibilized composites filled with 5wt% of R150 and R380 particles.

This is true even when the SAOS experiments are combined with the creep/recovery experiments in order to extend the time scale, as shown in Figure 7.11. The creep recovery compliances did not show any trend, contrary to what was seen for the non-compatibilized composites in Figure 7.6.

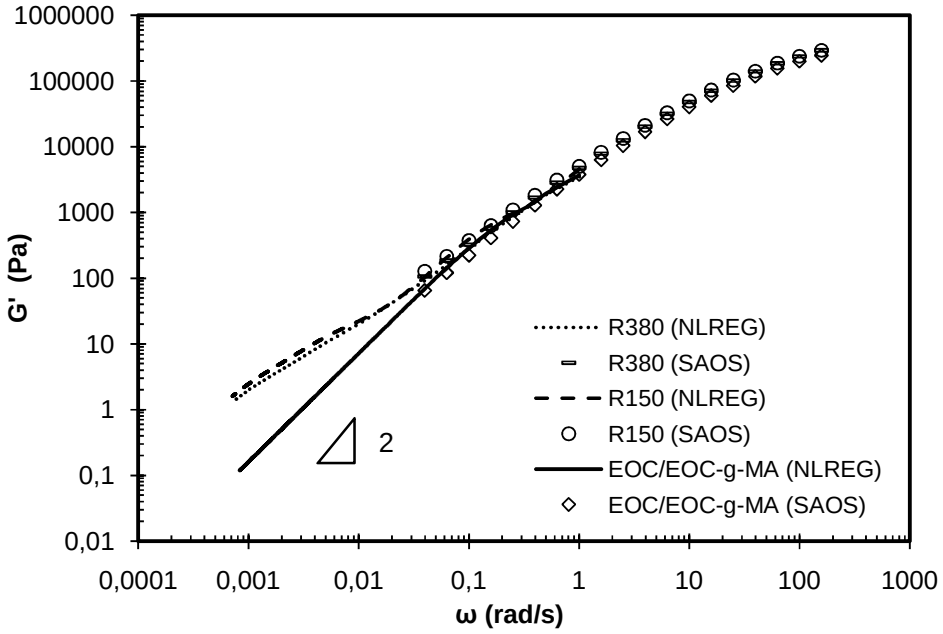

Figure 7.11 Storage modulus as a function of angular frequency for compatibilized materials filled with 5wt% of various particles. Superposition of experimental SAOS data and NLREG results from creep and creep recovery data.

As the TEM images revealed (see Figure 7.2), the dispersion of the nanoparticles inside the compatibilized matrix was similar regardless of the SSA. The similarity in microstructure supports the identical rheological behaviour.

7.3.5 Non-linear creep

In all previous results, the samples containing 2wt% SiO_2 generally reached steady-state very soon, after less than 100 s of creep time. A set of experiments were conducted at long times, lasting up to 5000 s to investigate the effect of shear on the morphology of the samples. These experiments involved very high deformations (up to 20 strain units), well above the limit of linear viscoelasticity. Results are shown in Figure 7.12.

Two distinct types of behavior can be seen, depending on the type of the matrix. Whereas the compatibilized samples achieve a constant value of t/J, the non-compatibilized samples experience a sharp upturn in t/J at around 1000 s. Furthermore, the upturn happens earlier when the R380 particles are used.

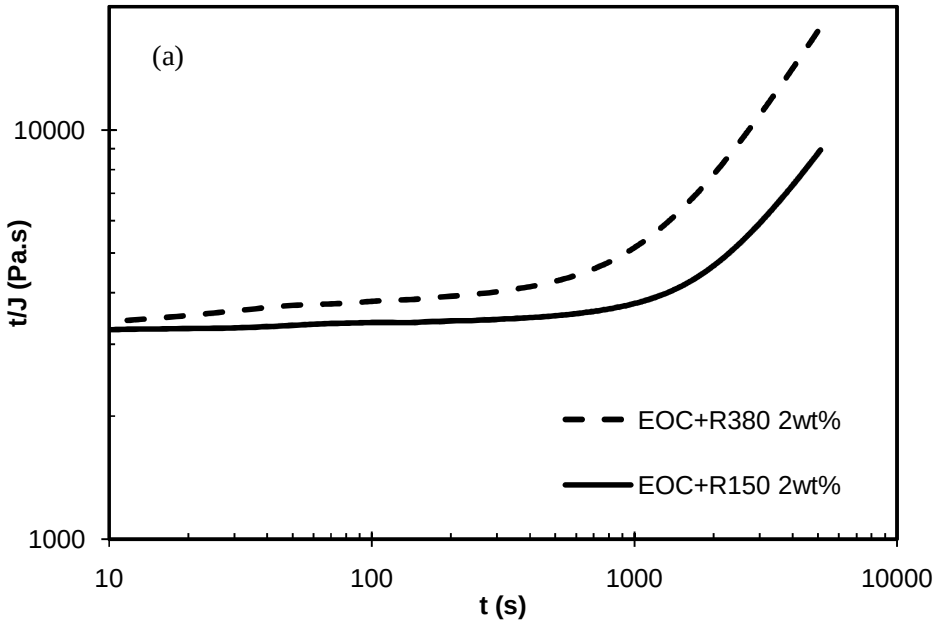

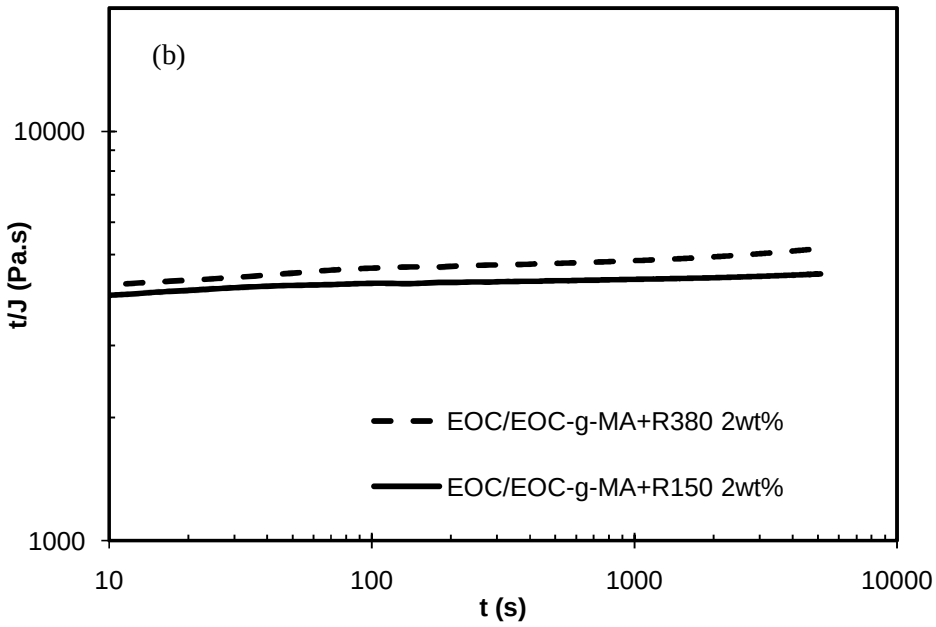

Figure 7.12 Non-linear creep at 150°C, 20Pa for 5000s for non-compatibilized (a) and compatibilized (b) materials filled with R150 and R380 at 2wt%.

The morphology of the samples before and after the creep experiments is shown in Figure 7.13.

.

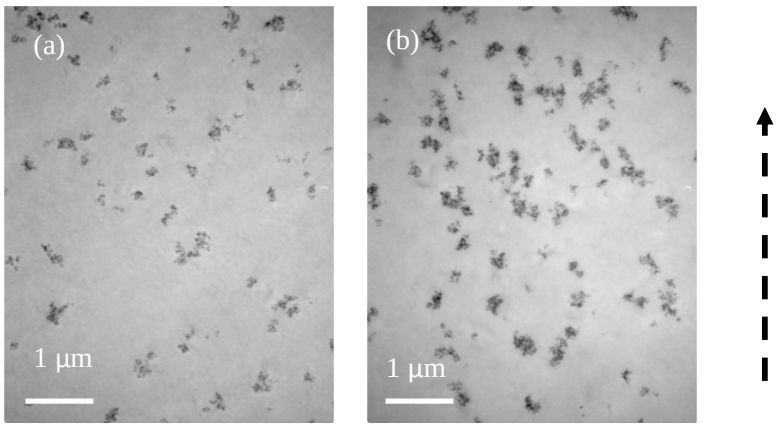

Figure 7.13 TEM images before (a) and after (b) creep of the EOC+R380 2wt% sample. The arrow indicates the direction of the flow.

It is striking when comparing Figure 7.13 (a) and (b) that the size of the aggregates has increased following completion of the creep experiment, and that they appear aligned along the direction of the flow. Obviously under the influence of shear the particles are free to associate with each other through hydrogen bonding between the silanol groups. This tendency becomes stronger as the SSA of the particles increases. On the other hand, compatibilized materials have a layer of bound polymer surrounding them, which would prevent them from further associating with each other, resulting in a more stable response. This behaviour is consistent with the time sweeps that were shown in Figure 7.4, where the non-compatibilized samples displayed a strong time-dependency, indicative of a change in the state of aggregation. The very strong increase in t/J as a function of time indicates that steady-shear has a more substantial influence rather than the oscillatory shear, and is capable of inducing particle orientation to a substantial degree.

7.3.6 Mechanical properties

The tensile properties of the cross-linked composites are shown in Figure 7.14. First of all, a significant reinforcement effect is observed upon addition of SiO_2 particles. Specifically when R200 is added, the properties of the pure EOC are increased by 14% for the stress and by 24% for the Young's modulus. When the EOC/EOC-g-MA matrix, the properties are increased by 26% for the stress and by 25% for the Young's modulus. The effect of SSA on the mechanical properties of the compatibilized samples was minor and not statistically significant.

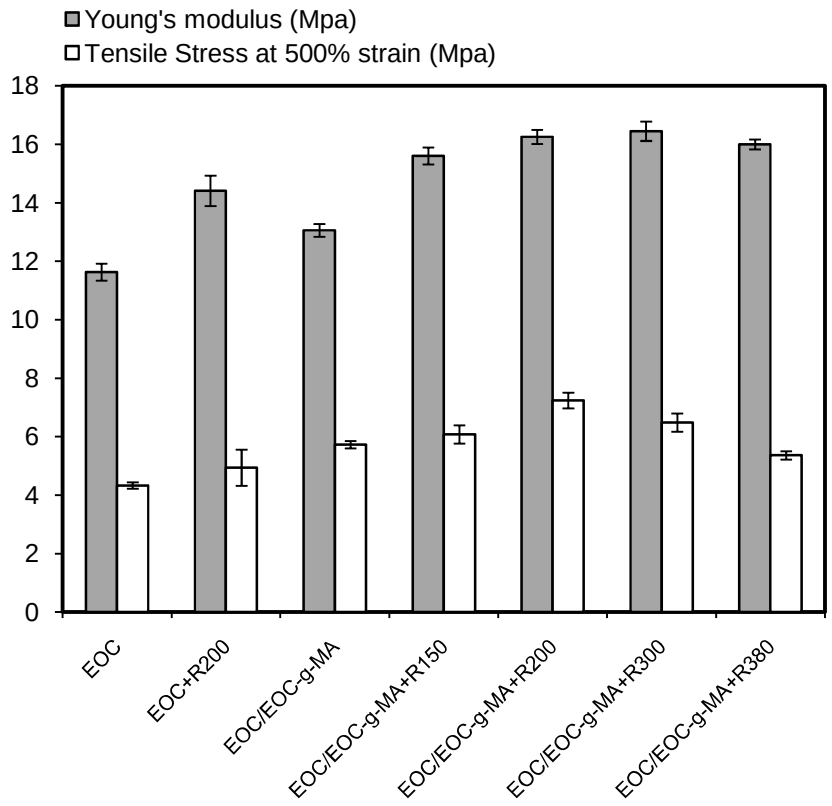

Figure 7.14 Results of mechanical testing for cross-linked compatibilized and non-compatibilized samples. Silica loading is 5wt%.

7.4 Discussion

The observed viscoelastic properties are largely dependent on the dispersion, which in turn depends on the interactions between polymer chains and nanoparticles. The latter occur either by physical adsorption in the absence of compatibilizer or by hydrogen bonding in the presence of compatibilizer. Rheology is thus a very sensitive indicator of the morphology of the nanocomposites.

Nanosilica particles dispersed in the non-compatibilized matrix have a tendency to associate, resulting in the formation of some aggregates during compounding. This tendency increases at higher SSAs. There is a small amount of BdP originating from the chains trapped inside the aggregates during compounding, but in both cases, the amount of bound polymer is not sufficient to completely coat the polymers, rather it represents the small number of chains adsorbed on the surface of the particles. The silanol groups are still free and able to associate during application of shear, which becomes evident during time sweeps and extended creep experiments. A conceptual illustration of SiO_2 particles having low and high SSAs dispersed within the non-compatibilized matrix is shown in Figure 7.15 (a) and (b).

The larger aggregates led to an amplified hydrodynamic effect, and therefore to an enhancement of the dynamic functions at low frequencies. Furthermore, by offering a greater surface available for adsorption, the particles with high SSAs offered more anchoring points for the adsorbed polymer chains. This resulted in increased elasticity, which in turn caused an increased recoverable compliance in creep experiments.

In the compatibilized materials, the amount of bound polymer measured was four times higher than in the non-compatibilized samples (see Figure 7.1), leading to the formation of a “shell” surrounding the particles, consisting of polymer chains adsorbed on their surface. A simplified illustration of the polymer shell, which considers each particle in isolation, without taking into account the formation of particle clusters, is represented in Figure 7.15 (c) and (d) by the dashed circles around the silica particles.

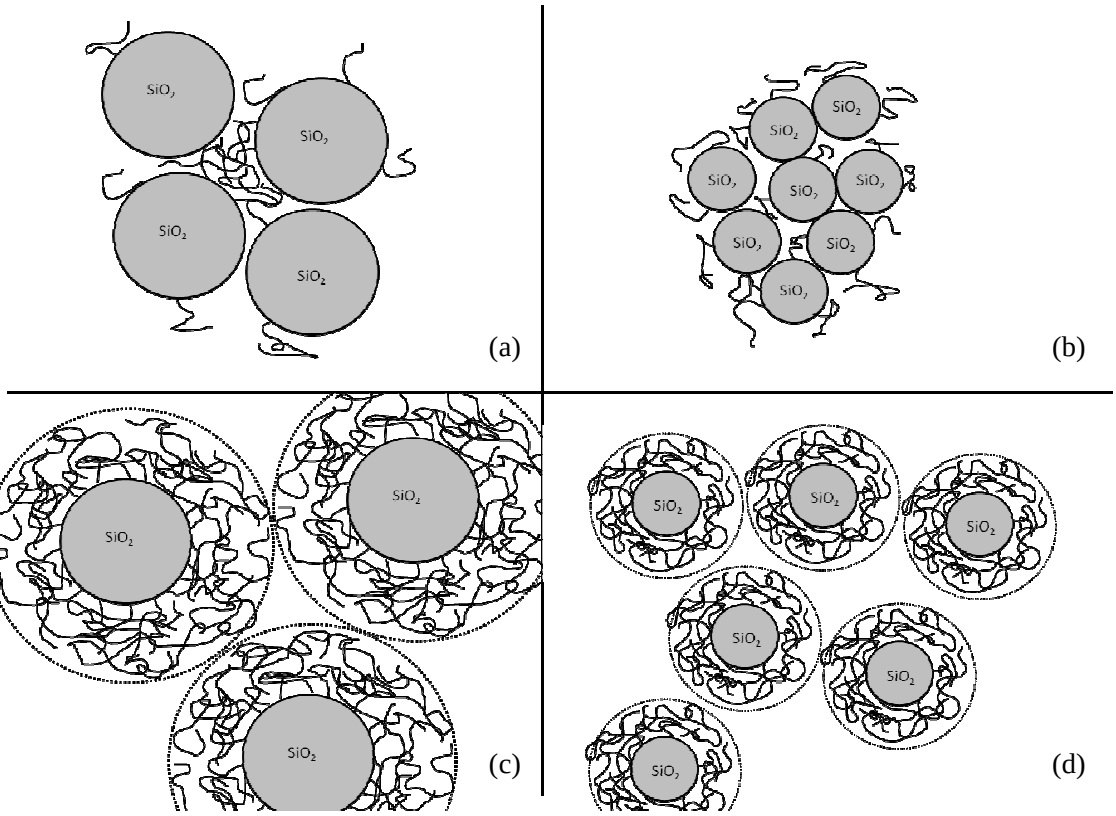

Figure 7.15 Schematic representation of the non-compatibilized materials reinforced with particles having (a) low SSAs, (b) high SSAs, and compatibilized materials reinforced with particles having (c) low SSAs, (d) high SSAs.

Based on the amounts of BdP measured and assuming an idealized case of spherical particles of density 2.2 $g.cm^{-3}$ and diameter according to the values presented in Table 7.1 surrounded by a bound polymer shell of density 0.864 $g.cm^{-3}$, it is possible to estimate the thickness of this shell. The values obtained are displayed in Table 7.2.

Table 7.2 Estimated thickness of polymer shell based on the amount of bound polymer for compatibilized composites filled with 5wt% of silica.

SSA (m^2/g)	150	200	300	380
Nominal Particle diameter (nm)	14	12	7	7
Shell thickness (nm)	8.9	7.6	4.3	4.5

As shown in Figure 7.1 higher SSAs led to higher amounts of BdP. It is interesting to note from the values of Table 7.2 that higher amounts of BdP do not necessarily correspond to a thicker shell. Indeed, the ratio particle diameter/shell thickness is constant and equal to about 1.5 for all the particles. These proportions are respected in Figure 7.15 (c) and (d). The thick polymer shell bound around the particles facilitates their breakup and prevents their re-agglomeration during shear experiments. It also masks the surface of the particles, so that these responses are not affected by the value of the SSA, thus explaining the observed insensitivity of the LVE characterizations to the SSA.

7.5 Conclusions

The effect of SSA and presence of a compatibilizer on the morphology and rheological properties of melt-compounded EOC/SiO_2 nanocomposites was investigated. In non-compatibilized samples, the state of dispersion of the particles depends on the SSA as higher SSAs led to a poorer dispersion. This was explained by the stronger F/F interactions in particles having higher SSA, leading to a reduced ability to break-up the aggregates during compounding. The bigger

aggregates observed for particles with high SSAs were at the origin of an enhanced hydrodynamic effect that was characterized by a significant increase of the storage modulus at low frequencies and increased recoverable compliance.

Bound polymer measurements revealed that in the presence of compatibilizer, higher SSAs led to greater amounts of BdP. The BdP formed a “shell” surrounding the particles that significantly lowered the interfacial tension between the particles and the polymer chains, leading to improved dispersion. However, the shell masked any difference in the particle surface, resulting in identical rheological and mechanical properties.

Chapter 8

CONCLUSIONS, SIGNIFICANT CONTRIBUTIONS AND RECOMMENDATIONS FOR FUTURE WORK

8.1 Conclusions

The mechanical performances of TPO blends were optimized by using different strategies such as the functionalization of the PP matrix or the addition of a compatibilizer, and the use of hydrophobic silica nanoparticles. Microscopy revealed that in the compatibilized and functionalized composites the silica nanoparticles localized exclusively in the PP phase and were finely dispersed resulting in a segregated microstructure. Coalescence of the EOC domains and coarsening of the microstructure were significantly reduced via a barrier effect induced by the presence of nanoparticles. When the combination of compatibilized or functionalized matrix and silica particles was used, the composites exhibited enhanced strength and stiffness in both flexural and tensile tests, whereas impact strength was maintained. This was attributed to the selective localization of the fillers, reinforcing the PP phase without compromising the ability of the EOC domains to act as impact modifiers, and to the presence of P/F interactions. Increasing silica concentration significantly changed the rheological behaviour at low frequencies to reach a "pseudo-solid" behaviour characterized by a reduced dependency of the complex viscosity and the elastic modulus on the frequency. The responses were influenced by the type of interactions between the nanofillers and the polymer matrix.

The influence of P/F and F/F interactions was further examined by preparing and characterizing binary EOC/SiO_2 nanocomposites. Grafting reactive and non-reactive silanes onto an EOC matrix enabled the differentiation between two different types of composites, based on the presence or absence of covalent bonding. Similarly, presence of EOC-g-MA as a compatibilizer combined with particles having various SSAs allowed the observation of the effects of various degrees of physical P/F interactions on the morphology and rheological properties of the nanocomposites. When chemical or physical P/F interactions were introduced, higher amounts of BdP were measured compared to systems in which no or weak interactions occured. The BdP formed a "shell" surrounding the particles that presumably lowered the interfacial tension between the particles and the polymer chains, explaining the improved dispersion observed. The values of the moduli at low frequencies scaled with the volume fraction of nanosilica according to a power-law relation, which is consistent with the presence of a fractal structure. Given that the composites were below the percolation threshold, this observation is attributed to the higher effective volume of the filler particles due to the presence of bound polymer. Time-sweep experiments showed that the composites were prone to aggregation in the absence of P/F interactions. Stress sweeps revealed that VTEOS-grafted and compatibilized composites were more capable of enduring high strains without any significant change in their viscoelastic properties. This behaviour was attributed to the presence of P/F interactions that create linkages between the hosting polymer chains and the nanoparticles.

When low silica concentrations were used, compatibilized and non-compatibilized composites could not be differentiated by SAOS experiments. The retardation spectra and the dynamic functions issued from creep/recovery data showed differences at long times (or low frequencies) according to the silica concentration and degree of P/F interactions that could not be detected by

conventional SAOS experiments. The results confirmed that P/F interactions via the state of dispersion of the particles are a key-factor determining the dynamic response of the composites: composites with finely-dispersed nanoparticles exhibited a more modest deviation compared to the unfilled matrix at very long times, as opposed to composites with bigger aggregates observed for particles with high SSAs. This phenomenon was explained by the size of the aggregates which is at the origin of an enhanced hydrodynamic effect characterized by a significant increase of the storage modulus at low frequencies and an increased recoverable compliance.

8.2 Significant Contributions

This work presents several approaches to obtain polyolefin nanocomposites with enhanced properties and offers some important contributions in the understanding of the complex structure/property relationships in polymer nanocomposites.

Chapters 3 and 4 present an approach to obtain a synergistic effect in polymer blends reinforced with silica nanoparticles, by taking advantage of both the addition of the rigid nanoparticles and the soft elastomer. A novel functionalization strategy that enables the formation of covalent bonds between the polyolefin and the nanofiller, thus ensuring good interfacial adhesion resulting in excellent mechanical properties has been implemented. This is of primary importance since the mechanical properties of polyolefins used in the industry could be significantly enhanced by using the strategies developed in this work without any major changes in the processing steps.

Chapters 5, 6 and 7 provide a detailed understanding of how the P/F interactions affect the microstructure and consequently the physical properties of the composites by using model

systems. It is expected that this knowledge will enable the synthesis of nanocomposites with predictable structures and properties using polyolefins of commercial interest. More specifically, knowledge on how to disperse efficiently nanoparticles into the inherently non-polar matrices can have important technological implications, not only to achieve good mechanical properties, but also in specialty applications, such as use of nanoparticles as nucleating agents for foaming or to promote crystallization.

The implementation of a rheological technique based on a combination of SAOS, creep and creep recovery experiments enabled a precise assessment of the microstructure of the composites. Given the ambiguities inherent in the rheological evaluation of these composites because of their pronounced tendency for agglomeration, availability of this method will provide a valuable tool in their characterization.

The recognition that depending on the extent of P/F and F/F interactions the nanoparticles have different tendencies for association, leading to potentially different structures, can be exploited by using processing techniques that promote a specific spatial arrangement, e.g. strings of particles aligned in a preferential direction. Such technologies would result in composites with optimum properties in a preferred direction.

8.3 Recommendations for Future Work

I. The prediction of the morphology of ternary nanocomposites is done via the thermodynamic and kinetic considerations reviewed in this work. However, it clearly appears that reliable experimental techniques to measure the required thermodynamic parameters, such as the surface

tensions of the polymers, the surface free energy of the nanoparticles and the interfacial tensions between the components at the appropriate temperature are currently missing. Future work is therefore needed to improve the current techniques available. This would serve two purposes: 1. to make the predictions regarding the morphology of the composites (quality of particle dispersion and filler localization) more accurate and 2. to quantitatively estimate the degree of interactions between the components. These are the two most important parameters influencing the ultimate performance of the composites.

II. In the ternary nanocomposites prepared and characterized in this work, only the interactions between PP and SiO_2 were studied. It would be very interesting to prepare similar ternary nanocomposites with a segregated morphology -as it showed the best combination of mechanical performances- and monitor the influence of various degrees of interactions between the thermoplastic matrix and the elastomeric phase. For example, one could imagine a system in which the matrix is a thermoplastic polar polymer (e.g. PEO) toughened with a thermoplastic non-polar elastomer such as EOC and reinforced with silica nanoparticles. In such system, there would be no need to functionalize the matrix or add a compatibilizer to obtain a segregated morphology. It would then be very interesting to gradually modify the elastomer by radical functionalization or by the addition of increasing amounts of compatibilizer to obtain various degrees of interactions with the matrix, and monitor the effects on the mechanical properties.

III. In this work, chemical and physical P/F interactions were investigated in EOC/SiO_2 binary nanocomposites. These are not the only types of interactions that can occur between the hosting polymer chains and the silica nanoparticles. It would be interesting to study the influence of other

types of P/F interactions, such as acid-base interactions and chain entanglements. The latter can be examined via the preparation of analogous EOC/SiO_2 nanocomposites using surface-modified SiO_2 nanoparticles on which macromolecules were grafted. Similar materials were prepared using PS as a matrix, but polyolefins have not been investigated yet.

IV. The investigation of the thermal properties of the composites, as well as the nucleating ability of the nanoparticles would also be of considerable interest.

V. As all the specimens in this work prepared by melt-mixing were shaped by using a compression moulding technique, it would be useful to study the effects of other post-processing methods on the morphology and properties of the nanocomposites. Especially, injection moulding is a very popular technique used in the plastics industry and could have significant impacts on the morphology and final properties of the materials, due to the high shear rates involved.

References

1. Wypych G Handbook of fillers. : ChemTec, 1999.

2. Usuki A, Kojima Y, Kawasumi M, et al. J Mater Res 1993;8(5):1179-1184.

3. Kojima Y, Usuki A, Kawasumi M, et al. J Mater Res 1993;8(5):1185-1189.

4. Thostenson ET, Li CY, Chou TW Composites Sci Technol 2005;65(3-4):491-516. doi:10.1016/j.compscitech.2004.11.003.

5. Tjong SC Mater Sci Eng R-Rep 2006;53(3-4):73-197. doi:10.1016/j.mser.2006.06.001.

6. Hussain F, Hojjati M, Okamoto M, Gorga RE J Composite Mater 2006;40(17):1511-1575. doi:10.1177/0021998306067321.

7. Alexandre M, Dubois P Mater Sci Eng R-Rep 2000;28(1-2):1-63.

8. Wang MJ Rubber Chem Technol 1998;71(3):520-589.

9. Leblanc JL Prog Polym Sci 2002;27(4):627-687.

10. Zou H, Wu S, Shen J Chem Rev 2008;108(9):3893-3957. doi:10.1021/cr068035q.

11. Soloukhin VA, Posthumus W, Brokken-Zijp JCM, Loos J, de With G Polymer 2002;43(23):6169-6181.

12. Su YH, Liu YL, Sun YM, Lai JY, Guiver MD, Gao Y J Power Sources 2006;155(2):111-117. doi:10.1016/j.jpowsour.2005.03.233.

13. Jain S, Goossens JGP, van Duin M Macromol Symp 2006;233:225-234. doi:10.1002/masy.200650129.

14. Bikiaris DN, Vassiliou A, Pavlidou E, Karayannidis GP European Polymer Journal 2005;41(9):1965-1978. doi:10.1016/j.eurpolymj.2005.03.008.

15. Rong MZ, Zhang MQ, Ruan WH Mater Sci Technol 2006;22(7):787-796. doi:10.1179/174328406X101247.

16. Rong MZ, Zhang MQ, Pan SL, Lehmann B, Friedrich K Polym Int 2004;53(2):176-183. doi:10.1002/pi.1307.

17. Liang JZ, Li RKY J Appl Polym Sci 2000;77(2):409-417.

18. Utracki LA Polymer alloys and blends: Thermodynamics and Rheology. Munich: Hanser Gardner, 1989.

19. Wu SH Polymer 1985;26(12):1855-1863.

20. Kontopoulou M, Wang W, Gopakumar TG, Cheung C Polymer 2003;44(24):7495-7504. doi:10.1016/j.polymer.2003.08.043.

21. Lee H, Fasulo PD, Rodgers WR, Paul DR Polymer 2005;46(25):11673-11689. doi:DOI: 10.1016/j.polymer.2005.09.068.

22. Gelfer MY, Song HH, Liu L, et al. J Polym Sci B Polym Phys 2003;41(1):44-54.

23. Li Y, Shimizu H Polymer 2004;45(22):7381-7388. doi:DOI: 10.1016/j.polymer.2004.09.018.

24. Mehrabzadeh M, Kamal MR Polym Eng Sci 2004;44(6):1152-1161.

25. Lee KY, Goettler LA Polym Eng Sci 2004;44(6):1103-1111.

26. Austin JR, Kontopoulou M Polym Eng Sci 2006;46(11):1491-1501.

27. Ma X, Liang G, Liu H, Fei J, Huang Y J Appl Polym Sci 2005;97(5):1915-1921.

28. Xiaoyan M, Guozheng L, Haijun L, Hailin L, Yun H J Appl Polym Sci 2005;97(5):1907-1914.

29. Khatua BB, Lee DJ, Kim HY, Kim JK Macromolecules 2004;37(7):2454-2459.

30. Mehta S, Mirabella FM, Rufener K, Bafna A J Appl Polym Sci 2004;92(2):928-936.

31. Bergna HE, Roberts WO Colloidal silica : fundamentals and applications;2006;131.

32. Brunauer S, Emmett PH, Teller E J Am Chem Soc 1938;60:309-319.

33. Zhang Q, Archer LA Langmuir 2002;18(26):10435-10442. doi:10.1021/la026338j.

34. Wu SH Polymer interface and adhesion;1982.

35. Zhang W, Leonov AI J Appl Polym Sci 2001;81(10):2517-2530. doi:10.1002/app.1693.

36. Chibowski E, Perea-Carpio R Adv Colloid Interface Sci 2002;98(2):245-264. doi:10.1016/S0001-8686(01)00097-5.

37. Ahn SH, Kim SH, Lee SG J Appl Polym Sci 2004;94(2):812-818. doi:10.1002/app.21007.

38. Ding X, Wang Z, Han D, et al. Nanotechnology 2006;17(19):4796-4801. doi:10.1088/0957-4484/17/19/002.

39. Reculusa S, Poncet-Legrand C, Ravaine S, Mingotaud C, Duguet E, Bourgeat-Lami E Chem Mat 2002;14(5):2354-2359. doi:10.1021/cm0116525.

40. Bikiaris DN, Papageorgiou GZ, Pavlidou E, Vouroutzis N, Palatzoglou P, Karayannidis GP J Appl Polym Sci 2006;100(4):2684-2696. doi:10.1002/app.22849.

41. Aranguren MI, Mora E, Degroot JV, Macosko CW J Rheol 1992;36(6):1165-1182.

42. Papageorgiou GZ, Achilias DS, Bikiaris DN, Karayannidis GP Thermochim Acta 2005;427(1-2):117-128. doi:10.1016/j.tca.2004.09.001.

43. Gun'ko VM, Voronin EF, Pakhlov EM, et al. Colloid Surf A-Physicochem Eng Asp 2000;166(1-3):187-201.

44. Wu W, Wagner MH, Xu Z Colloid Polym Sci 2003;281(6):550-555.

45. Bartholome C, Beyou E, Bourgeat-Lami E, et al. Polymer 2005;46(23):9965-9973. doi:10.1016/j.polymer.2005.07.057.

46. Goel V, Chatterjee T, Bombalski L, Yurekli K, Matyjaszewski K, Krishnamoorti R J Polym Sci Pt B-Polym Phys 2006;44(14):2014-2023. doi:10.1002/polb.20827.

47. Edmondson S, Osborne VL, Huck WTS Chem Soc Rev 2004;33(1):14-22. doi:10.1039/b210143m.

48. Rong MZ, Zhang MQ, Zheng YX, Zeng HM, Friedrich K Polymer 2001;42(7):3301-3304.

49. Rong MZ, Zhang MQ, Zheng YX, Zeng HM, Walter R, Friedrich K Polymer 2001;42(1):167-183.

50. Shieh YT, Liu CM J Appl Polym Sci 1999;74(14):3404-3411.

51. Demjen Z, Pukanszky B, Nagy J Polymer 1999;40(7):1763-1773.

52. Yang S, Song G, Zhao Y, Yang C, She X Polym Eng Sci 2007;47(7):1004-1008. doi:10.1002/pen.20753.

53. Jiao C, Wang Z, Gui Z, Hu Y European Polymer Journal 2005;41(6):1204-1211. doi:10.1016/j.eurpolymj.2004.12.008.

54. Parent JS, Tripp M, Dupont J Polym Eng Sci 2003;43(1):234-242. doi:10.1002/pen.10020.

55. Beltran M, Mijangos C Polym Eng Sci 2000;40(7):1534-1541.

56. Wu C, Liao H J Appl Polym Sci 2003;88(4):966-972. doi:10.1002/app.11725.

57. Yurekli K, Krishnamoorti R, Tse MF, Mcelrath KO, Tsou AH, Wang HC J Polym Sci Pt B-Polym Phys 2001;39(2):256-275.

58. Zhou X, Dai G, Guo W, Qunfang J Appl Polym Sci 2000;76(8):1359-1365. doi:10.1002/(SICI)1097-4628(20000523)76:8<1359::AID-APP17>3.0.CO;2-A.

59. Bikiaris D, Matzinos P, Larena A, Flaris V, Panayiotou C J Appl Polym Sci 2001;81(3):701-709. doi:10.1002/app.1487.

60. Qiu WL, Mai KC, Zeng HM J Appl Polym Sci 1999;71(10):1537-1542.

61. Rong MZ, Ji QL, Zhang MQ, Friedrich K Eur Polym J 2002;38(8):1573-1582.

62. Turcsanyi B, Pukanszky B, Tudos F J Mater Sci Lett 1988;7(2):160-162.

63. Pukanszky B, Tudos F, Kolarik J, Lednicky F Polym Compos 1990;11(2):98-104.

64. Ma CG, Mai YL, Rong MZ, Ruan WH, Zhang MQ Composites Sci Technol 2007;67(14):2997-3005.

65. Cassagnau P Polymer 2008;49(9):2183-2196. doi:DOI: 10.1016/j.polymer.2007.12.035.

66. Payne AR Reinforcement of elastomers. In: Anonymous Reinforcement of elastomers. New York: Interscience, 1965. pp. 69-123.

67. Smallwood HM J Appl Phys 1944;15(11):758-766.

68. Elias L, Fenouillot F, Majesté J-, Martin G, Cassagnau P J Polym Sci B Polym Phys 2008;46(18):1976-1983.

69. Elias L, Fenouillot F, Majeste JC, Cassagnau P Polymer 2007;48(20):6029-6040. doi:DOI: 10.1016/j.polymer.2007.07.061.

70. Fenouillot F, Cassagnau P, Majesté J- Polymer 2009;50(6):1333-1350. doi:DOI: 10.1016/j.polymer.2008.12.029.

71. Liu Y, Kontopoulou M Polymer 2006;47(22):7731-7739. doi:DOI: 10.1016/j.polymer.2006.09.014.

72. Liu Y, Kontopoulou M Journal of Vinyl and Additive Technology 2007;13(3):147-150. doi:10.1002/vnl.20118.

73. Yang H, Zhang Q, Guo M, Wang C, Du R, Fu Q Polymer 2006;47(6):2106-2115. doi:DOI: 10.1016/j.polymer.2006.01.076.

74. Yang H, Zhang X, Qu C, et al. Polymer 2007;48(3):860-869. doi:DOI: 10.1016/j.polymer.2006.12.022.

75. Yang H, Li B, Wang K, et al. European Polymer Journal 2008;44(1):113-123. doi:10.1016/j.eurpolymj.2007.10.028.

76. Sumita M, Sakata K, Asai S, Miyasaka K, Nakagawa H Polymer Bulletin 1991;25(2):265-271.

77. Ma CG, Zhang MQ, Rong MZ J Appl Polym Sci 2007;103(3):1578-1584. doi:10.1002/app.25431.

78. Clarke J, Clarke B, Freakley PK, Sutherland I Plast Rubber Compos 2001;30(1):39-44.

79. Zhou P, Yu W, Zhou C, Liu F, Hou L, Wang J J Appl Polym Sci 2007;103(1):487-492. doi:10.1002/app.25020.

80. Dasari A, Yu Z, Mai Y Polymer 2005;46(16):5986-5991. doi:DOI: 10.1016/j.polymer.2005.05.145.

81. Ray SS, Pouliot S, Bousmina M, Utracki LA Polymer 2004;45(25):8403-8413. doi:10.1016/j.polymer.2004.10.009.

82. Ray SS, Bousmina M Macromolecular Rapid Communications 2005;26(20):1639-1646. doi:10.1002/marc.200500447.

83. Zhang Q, Yang H, Fu Q Polymer 2004;45(6):1913-1922. doi:DOI: 10.1016/j.polymer.2004.01.037.

84. Wang Y, Zhang Q, Fu Q Macromolecular Rapid Communications 2003;24(3):231-235. doi:10.1002/marc.200390026.

85. Voulgaris D, Petridis D Polymer 2002;43(8):2213-2218. doi:DOI: 10.1016/S0032-3861(02)00039-3.

86. Dorazio L, Mancarella C, Martuscelli E, Sticotti G, Massari P Polymer 1993;34(17):3671-3681.

87. Choudhary V, Varma HS, Varma IK Polymer 1991;32(14):2534-2540.

88. Da Silva ALN, Rocha MCG, Coutinho FMB, Bretas R, Scuracchio C J Appl Polym Sci 2000;75(5):692-704.

89. McNally T, McShane P, Nally GM, Murphy WR, Cook M, Miller A Polymer 2002;43(13):3785-3793.

90. Premphet K, Paecharoenchai W J Appl Polym Sci 2002;85(11):2412-2418. doi:10.1002/app.10886.

91. Paul S, Kale DD J Appl Polym Sci 2000;76(9):1480-1484.

92. Paul S, Kale DD J Appl Polym Sci 2002;84(3):665-671. doi:10.1002/app.10376.

93. Yang JH, Zhang Y, Zhang YX Polymer 2003;44(17):5047-5052. doi:10.1016/S0032-3861(03)00438-5.

94. DaSilva ALN, Tavares MIB, Politano DP, Coutinho FMB, Rocha MCG J Appl Polym Sci 1997;66(10):2005-2014.

95. Da Silva ALN, Rocha MCG, Coutinho FMB, Bretas RES, Scuracchio C J Appl Polym Sci 2001;79(9):1634-1639.

96. Da Silva ALN, Rocha MCG, Coutinho FMB, Bretas RES, Farah M Polym Test 2002;21(6):647-652.

97. Kim BK, Kim MS, Kim KJ J Appl Polym Sci 1993;48(7):1271-1278.

98. Hornsby PR, Premphet K J Appl Polym Sci 1998;70(3):587-597.

99. Liang JZ, Li RKY, Tjong SC Polym Compos 1999;20(3):413-422.

100. Molnar S, Pukanszky B, Hammer CO, Maurer FHJ Polymer 2000;41(4):1529-1539.

101. Chiang WY, Yang WD, Pukanszky B Polym Eng Sci 1992;32(10):641-648.

102. Schaefer KU, Theisen A, Hess M, Kosfeld R Polym Eng Sci 1993;33(16):1009-1021.

103. Tjong SC, Meng YZ J Polym Sci Pt B-Polym Phys 2003;41(19):2332-2341. doi:10.1002/polb.10587.

104. Premphet K, Horanont P Polymer 2000;41(26):9283-9290.

105. Premphet-Sirisinha K, Preechachon I J Appl Polym Sci 2003;89(13):3557-3562. doi:10.1002/app.12544.

106. Lee SH, Kontopoulou M, Park CB Polymer 2010;51(5):1147-1155. doi:DOI: 10.1016/j.polymer.2010.01.018.

107. Pavlidou E, Bikiaris D, Vassiliou A, Chiotelli M, Karayannidis G Second Conference on Microelectronics, Microsystems and Nanotechnology 2005;10:190-193. doi:10.1088/1742/6596/10/1/047.

108. Lacroix C, Bousmina M, Carreau PJ, Favis BD, Michel A Polymer 1996;37(14):2939-2947.

109. Mekhilef N, Favis BD, Carreau PJ J Polym Sci Pt B-Polym Phys 1997;35(2):293-308.

110. Vinckier I, Laun HM Rheol Acta 1999;38(4):274-286.

111. Martin P, Carreau PJ, Favis BD, Jerome R J Rheol 2000;44(3):569-583.

112. Maani A, Heuzey M, Carreau P Coalescence in thermoplastic olefin (TPO) blends under shear flow; Rheologica Acta 2010:1-15. doi:10.1007/s00397-010-0501-6.

113. Wu SH J Appl Polym Sci 1988;35(2):549-561.

114. Hasegawa N, Okamoto H, Kawasumi M, Kato M, Tsukigase A, Usuki A Macromol Mater Eng 2000;280(7-8):76-79.

115. Shim JH, Joo JH, Jung SH, Yoon J J Polym Sci B Polym Phys 2007;45(5):607-615. doi:10.1002/polb.21048.

116. Jancar J, Dibenedetto AT J Mater Sci 1994;29(17):4651-4658.

117. Wu CL, Zhang MQ, Rong MZ, Friedrich K Composites Sci Technol 2002;62(10-11):1327-1340.

118. Ramier J, Gauthier C, Chazeau L, Stelandre L, Guy L J Polym Sci Pt B-Polym Phys 2007;45(3):286-298. doi:10.1002/polb.21033.

119. Parent JS, Parodi R, Wu W Polym Eng Sci 2006;46(12):1754-1761. doi:10.1002/pen.20642.

120. Danusso F, Gianotti G European Polymer Journal 1968;4(1):165-171.

121. Mekhilef N, Carreau PJ, Favis BD, Martin P, Ouhlal A J Polym Sci Pt B-Polym Phys 2000;38(10):1359-1368.

122. Owens DK, Wendt RC J Appl Polym Sci 1969;13(8):1741-1747. doi:10.1002/app.1969.070130815.

123. Raghavan SR, Khan SA J Rheol 1995;39(6):1311-1325.

124. Khan SA, Zoeller NJ J Rheol 1993;37(6):1225-1235.

125. Kraus G Reinforcement of elastomers. New York: Interscience Publishers, 1965.

126. de Gennes PG Scaling Concepts in Polymer Physics. Ithaca, New York: Cornell University Press, 1979.

127. Piau JM, Dorget M, Palierne JF J Rheol 1999;43(2):305-314.

128. Galindo-Rosales FJ, Rubio-Hernandez FJ, Velazquez-Navarro JF Rheol Acta 2009;48(6):699-708. doi:10.1007/s00397-009-0367-7.

129. Buscall R, Mills PDA, Goodwin JW, Lawson DW Journal of the Chemical Society, Faraday Transactions 1: Physical Chemistry in Condensed Phases 1988;84(12):4249-4260. doi:10.1039/F19888404249.

130. Yziquel F, Carreau PJ, Tanguy PA Rheol Acta 1999;38(1):14-25.

131. Rueb CJ, Zukoski CF J Rheol 1997;41(2):197-218.

132. Chakraborti RK, Atkinson JF, Van Benschoten JE Environ Sci Technol 2000;34(18):3969-3976. doi:10.1021/es990818o.

133. Heinrich G, Kluppel M Recent Advances in the Theory of Filler Networking in Elastomers. In: Anonymous Filled Elastomers Drug Delivery Systems. Berlin: Heidelberg, 2002. pp. 1-44.

134. Huber G, A.Vilgis T Macromolecules 2002;35(24):9204-9210. doi:10.1021/ma0208887.

135. Shang SW, Williams JW, Soderholm KJM J Mater Sci 1995;30(17):4323-4334.

136. Bansal A, Yang H, Li C, Benicewicz BC, Kumar SK, Schadler LS J Polym Sci B Polym Phys 2006;44(20):2944-2950. doi:10.1002/polb.20926.

137. Taniguchi Y, Shirai K, Saitoh H, Yamauchi T, Tsubokawa N Polymer 2005;46(8):2541-2547. doi:DOI: 10.1016/j.polymer.2005.02.016.

138. Sengupta SS, Parent JS Polym Eng Sci 2006;46(4):480-485. doi:10.1002/pen.20500.

139. Sato Y, Hashiguchi H, Inohara K, Takishima S, Masuoka H Fluid Phase Equilib 2007;257(2):124-130. doi:10.1016/j.fluid.2007.01.013.

140. Yatsuyanagi F, Suzuki N, Ito M, Kaidou H Polymer 2001;42(23):9523-9529. doi:DOI: 10.1016/S0032-3861(01)00472-4.

141. Liu C, He J, Ruymbeke Ev, Keunings R, Bailly C Polymer 2006;47(13):4461-4479. doi:DOI: 10.1016/j.polymer.2006.04.054.

142. Baumgaertel M, Winter HH Rheol Acta 1989;28(6):511-519.

143. Sasaki H, Shibata S, Hatanaka T Bull Natl Grassl Res Inst 1994;49:17-24.

144. Elias L, Fenouillot F, Majesté JC, Alcouffe P, Cassagnau P Polymer 2008;49(20):4378-4385. doi:DOI: 10.1016/j.polymer.2008.07.018.

145. White JL, Crowder JW J Appl Polym Sci 1974;18(4):1013-1038.

146. Romeo G, Filippone G, Fernández-Nieves A, Russo P, Acierno D Rheol Acta 2008;47(9):989-997. doi:10.1007/s00397-008-0291-2.

147. Zhu Z, Thompson T, Wang S, Meerwall EDv, Halasa A Macromolecules 2005;38(21):8816-8824. doi:10.1021/ma050922s.

148. Paquien JN, Galy J, Gerard JF, Pouchelon A Colloid Surf A-Physicochem Eng Asp 2005;260(1-3):165-172.

149. Lee JA, Kontopoulou M, Parent JS Polymer 2004;45(19):6595-6600. doi:DOI: 10.1016/j.polymer.2004.07.017.

150. Cassagnau P, Mélis F Polymer 2003;44(21):6607-6615. doi:DOI: 10.1016/S0032-3861(03)00689-X.

151. Abbasi S, Carreau P, Derdouri A, Moan M Rheol Acta 2009;48(9):943-959. doi:10.1007/s00397-009-0375-7.

152. Bossard F, Moan M, Aubry T J Rheol 2007;51(6):1253-1270. doi:10.1122/1.2790023.

153. Cassagnau P Polymer 2003;44(8):2455-2462. doi:DOI: 10.1016/S0032-3861(03)00094-6.

154. Clement F, Bokobza L, Monnerie L Rubber Chem Technol 2005;78(2):211-231.

155. Fetters LJ, Lohse DJ, Richter D, Witten TA, Zirkel A Macromolecules 1994;27(17):4639-4647.

156. Gahleitner M Progress in Polymer Science 2001;26(6):895-944. doi:10.1016/S0079-6700(01)00011-9.

157. Sternstein SS, Zhu AJ Macromolecules 2002;35(19):7262-7273. doi:10.1021/ma020482u.

158. Kaschta J, Schwarzl FR Rheol Acta 1994;33(6):517-529.

159. Kaschta J, Schwarzl FR Rheol Acta 1994;33(6):530-541.

160. Gabriel C, Kaschta J, Munstedt H Rheol Acta 1998;37(1):7-20.

161. Kraft M, Meissner J, Kaschta J Macromolecules 1999;32(3):751-757.

162. He CX, Wood-Adams P, Dealy JM J Rheol 2004;48(4):711-724.

163. Shaayegan V, Wood-Adams P, Demarquette NR, Souza AMC The Polymer Processing society 26th annual meeting, Banff, Canada 2010.

164. Triebel C, Katsikis N, Stara H, Muenstedt H J Rheol 2010;54(2):407-420. doi:10.1122/1.3314291.

165. Muenstedt H, Koeppl T, Triebel C Polymer 2010;51(1):185-191. doi:10.1016/j.polymer.2009.11.049.

166. Ferry JD, 1912- Viscoelastic properties of polymers /. New York: Wiley, 1980.

167. Honerkamp J Rheol Acta 1989;28(5):363-371.

168. Honerkamp J, Weese J Rheol Acta 1993;32(1):65-73.

169. Eckstein A, Suhm J, Friedrich C, et al. Macromolecules 1998;31(4):1335-1340.

170. Freiburg Materials Research Center NLREG (non-linear-regularization);2006;1650.

171. Sahakaro K, Beraheng S J Appl Polym Sci 2008;109(6):3839-3848. doi:10.1002/app.28483.

172. Pollanen M, Pelz U, Suvanto M, Pakkanen TT J Appl Polym Sci 2010;116(2):1218-1225. doi:10.1002/app.31673.

173. Sternstein SS, Amanuel S, Shofner ML Rubber Chem Technol 2010;83(2):181-198.

174. Wang MJ, Lu SX, Mahmud K J Polym Sci Pt B-Polym Phys 2000;38(9):1240-1249.

175. Pistor V, Lizot A, Fiorio R, Zattera AJ Polymer 2010;51(22):5165-5171. doi:10.1016/j.polymer.2010.08.045.

176. Szekeres M, Toth J, Dekany I Langmuir 2002;18(7):2678-2685. doi:10.1021/la011370j.

177. Parent JS, Mrkoci MI, Hennigar SL plas rub compos 2003;32(3):114-121. doi:10.1179/146580103225001354.

178. Wang M-, Morris MD, Kutsovsky Y KGK-Kautsch Gummi Kunstst 2008;61(3):107-117.

179. Jauregui-Beloqui B, Fernandez-Garcia JC, Orgiles-Barcelo AC, Mahiques-Bujanda MM, Martin-Martinez JM J Adhes Sci Technol 1999;13(6):695-711.

180. Dorigato A, Pegoretti A, Penati A Express Polym Lett 2010;4(2):115-129. doi:10.3144/expresspolymlett.2010.16.

181. Camenzind A, Schweizer T, Sztucki M, Pratsinis SE Polymer 2010;51(8):1796-1804. doi:10.1016/j.polymer.2010.02.030.

182. Cochrane H, Lin CS Rubber Chem Technol 1993;66(1):48-60.